University of California
Santa Barbara

First principles studies of thermal, structural, and chemical phase spaces in quantum materials

A dissertation submitted in partial satisfaction
of the requirements for the degree

Doctor of Philosophy
in
Materials

by

Alex Hallett

Committee in charge:

Professor John Harter, Chair
Professor Ram Seshadri
Professor Susanne Stemmer
Professor Bolin Liao

June 2024

The Dissertation of Alex Hallett is approved.

Professor Ram Seshadri

Professor Susanne Stemmer

Professor Bolin Liao

Professor John Harter, Committee Chair

June 2024

First principles studies of thermal, structural, and chemical phase spaces in quantum materials

by

Alex Hallett

For my best friend.

So many of the best moments of my life were possible because of you.

You are such an important part of the person I have become.

You will always be with me wherever I go.

I love you so much.

Lee Hansche

March 8, 1978 - May 21, 2024

"The value engine is moving from the certainties of answers to the uncertainties of questions. Facts, order, and answers will always be needed and useful. But the most precious aspects, the most dynamic, most valuable, and most productive facets of our lives and new technology will lie in the frontiers, in the edges where uncertainty, chaos, fluidity, and questions dwell."

– from *The Inevitable*, by Kevin Kelley

Acknowledgements

First and foremost, I would like to thank my advisor John Harter for his guidance and support throughout my PhD. He was always extremely patient and took the time to answer my many questions. It is rare to meet someone with such a high level of expertise in so many areas - from designing and building experimental equipment to programming to quantum theory - the extent of his knowledge in so many topics is truly inspiring.

I would also like to thank Professors Susanne Stemmer, Ram Seshadri, and Bolin Liao for serving on my thesis committee. Their insightful questions and advice were extremely valuable in keeping my projects on course. A special thanks to Professor Stemmer for our conversations about the strontium titanate project.

Throughout my time at UCSB, I have benefited from a wonderful community of colleagues and friends. Thank you to all the members of the Harter group: Ryan, Ruben, Jack, Art, and Nick, it has been wonderful working alongside you. I have many fond memories of our many talks and laughs, as well as trips hiking and climbing. You were the best coworkers one could hope for!

As the only computationalist in an experimental group, I greatly appreciated the support I received from other computationalists: Sam who helped me get started with DFT calculations, Farnaz, Siavash, Yubi, Aury, and Justin for providing helpful advice and commiseration about the specific challenges of computational work.

My work would not have been possible without the computing resources at CNSI and the staff who manage them, so a big thanks goes to Fuzzy and Paul for all they do. Additionally, I am grateful to the experimentalists who synthesized and characterized the materials I studied: Ryan Russell, Guomin Zho, Noah Ratcliff, Salva-Salmani Rezaie, Kaveh Ahadi, Nicholas Combs, and Hanbyeol Jeong. You all laid the groundwork for my computational contributions.

One of the most fulfilling parts of graduate school was the scientific outreach I participated in. I would like to thank Wendy Ibsen for her work bringing science to the community. Thank you to Catalina for being a wonderful intern in the Summer of 2022, and to all the Quantum Foundry interns I had the pleasure of guiding through the summer of 2023. I was also honored to have the opportunity to teach a group of highly motivated high school students who signed up to learn about quantum mechanics on Saturdays! Education and outreach will undoubtedly be a cornerstone of my career going forward.

My personal support system was also much needed during my PhD. I extend my gratitude to Rey and Alyssa for embarking on so many wonderful adventures with me and being a part of my journey. My family, including Lee and Torie, have provided me with a quality of love and support that is invaluable. Wherever I go and whatever I do, the knowledge that there are people out there who truly know and love me keeps me grounded and fulfilled.

Finally, I would like to acknowledge the significance of the solitary moments I spent in deserts and rivers, on mountains and beaches, at the bases of waterfalls and the mouths of caves. I will always remember driving towards my next solo adventure with the windows down and the music up, feeling profoundly free.

Curriculum Vitæ

Alex Hallett

Education

2024	Ph.D., Materials, University of California, Santa Barbara
2019	B.S., Chemical Engineering, University of Arkansas, Fayetteville, Arkansas

Publications

"Effects of doping on lattice dynamics and polar order in strontium titanate," Alex Hallett and John W. Harter, *in preparation*.

"Coexistence of antiferrodistortive and polar order in a superconducting $SrTiO_3$ film," Guomin Zhu, Alex Hallett, Nicholas G. Combs, Hanbyeol Jeong, Arda Genc, John W. Harter, and Susanne Stemmer, *Physical Review Materials*, 8, 001800 (2024): L051801.

"Combinatorial exploration of quantum spin liquids in the herbertsmithite material family," Alex Hallett, Catalina Avarvarei, and John Harter, *Physical Review Materials*, 7, (2023): 064403.

"Modeling polar order in compressively strained strontium titanate," Alex Hallett, and John W. Harter, *Physical Review B*, 106, (2022): 214107.

"Coherent phonon spectroscopy and interlayer modulation of charge density wave order in the kagome metal CsV_3Sb_5," Noah Ratcliff, Lily Hallett, Brenden R. Ortiz, Stephen D. Wilson, and John W. Harter, *Physical Review Materials*, 5, (2021): L111801.

"Superconducting MoN thin films prepared by DC reactive magnetron sputtering for nanowire single-photon detectors," Lily Hallett, Ilya Charaev, Akshay Agarwal, Andrew Dane, Marco Colangelo, Di Zhu, and Karl K. Berggren, *Superconducting Science and Technology*, 34, (2021): 035012.

Abstract

First principles studies of thermal, structural, and chemical phase spaces in quantum materials

by

Alex Hallett

In quantum materials, phenomena occurring at the subatomic level can manifest as properties on a macroscopic scale. The exploration of quantum effects in materials with nontrivial band topology and strongly correlated electrons holds great promise for technological advancement in fields such as quantum computing. This thesis examines properties of three such quantum materials using computational methods.

The primary material system investigated is strontium titanate, an incipient ferroelectric that gives rise to an unconventional superconducting state at exceptionally low doping levels. The polar phase can be stabilized through strain or chemical substitution. Remarkably, superconductivity is enhanced within the polar phase, suggesting that the polar instability plays a pivotal role in the superconducting pairing mechanism. We develop a simplified free energy model combined with statistical mechanics methods to assess the character of the polar transition, which we find to be neither order-disorder nor displacive.

We explore the effects of doping on the structural phase transitions and find that, in agreement with experiment, the polar distortion and formation of polar nanodomains are suppressed in the presence of free carriers, while antiferrodistortive order remains essentially unchanged. The single-domain nature and insensitivity to doping suggest that the antiferrodistortive order does not play an important role in Cooper pairing. By calculating electronic properties in the polar phase, we analyze parameters that are

relevant to superconductivity such as the density of states at the Fermi level, the Rashba splitting of the energy bands, and the Migdal ratio.

We explore the chemical phase space of the naturally occurring minerals herbertsmithite [$ZnCu_3(OH)_6Cl_2$] and Zn-substituted barlowite [$ZnCu_3(OH)_6BrF$], which both feature perfect kagome layers of spin-1/2 copper ions and display experimental signatures consistent with a quantum spin liquid state at low temperatures. To identify other possible candidates within this material family, we perform a systematic first-principles combinatorial exploration of structurally related compounds [$ACu_3(OH)_6B_2$ and $ACu_3(OH)_6BC$] by substituting nonmagnetic divalent cations (A) and halide anions (B, C). We select several promising candidate materials that we believe deserve further attention.

Finally, we examine CsV_3Sb_5, a member of the AV_3Sb_5 (A = K,Rb,Cs) family of kagome metals, whose low-energy physics is dominated by an unusual charge density wave phase. We elucidate the nature of the charge density wave order parameter using first-principles density functional theory calculations which support the findings of experimental coherent phonon spectroscopy measurements. Through our study of the structural phase space of CsV_3Sb_5, we find that the charge density wave can be described as tri-hexagonal ordering with interlayer modulation along the c-axis.

First-principles techniques are often limited by their inability to incorporate the effects of temperature and disorder. Here, we augment first-principles density functional calculations using statistical mechanics methods such as the Metropolis Monte Carlo algorithm and Langevin dynamics to incorporate temperature effects on large, disordered supercells to simulate the thermal phase space of strontium titanate. The chemical phase of the herbertsmithite material family is systematically explored through high-throughput first-principles pseudo-convex hull calculations and an assessment of defect formation energy. We use frozen phonon calculations to investigate the structural phase space of

CsV_3Sb_5 and find that the charge density wave order expands beyond the previously studied 2×2×1 construction. Our techniques can be applied more broadly to other material systems to expand the capabilities of computational methods to accurately capture thermal effects and structural disorder in quantum materials.

Contents

Chapter 1

Introduction

1.1 Outline

Chapter 1 will provide an overview of the physical phenomena relevant to the materials systems studied in this thesis, including ferroelectricity and superconductivity, charge density wave order, and quantum spin-liquid behavior. In Chapter 2, I will describe the first principles, phenomenological, and statistical mechanical methods I use in my research. I discuss the results of my work characterizing the polar phase transition in strontium titanate in Chapter 3 after giving a review of previous experimental and computational studies of the polar phase transition. Chapter 4 will examine the electronic properties and assess parameters relevant to superconductivity in compressively strained $SrTiO_3$. In Chapter 5, I will describe a combinatorial exploration of herbertsmithite-related spin-liquid compounds to identify new quantum spin liquid candidates. I will report the characterization of the charge density wave order of CsV_3Sb_5 in Chapter 6. Chapter 7 will conclude with an exploration of future directions for research for each material system, and suggest other potential applications for the methods used in this work.

1.2 Ferroelectricity

Ferroelectrics are insulating materials possessing at least two stable or metastable states with spontaneous, finite electric polarization in the absence of any external electric field. The system must be able to switch between the two polarization states under the application of an applied electric field. The coupling of the polarization to the field is given by $-E \cdot P$. Polarization can be approximated by the magnitude of ionic displacements from the high symmetry structure and the Born effective charges.

The ability of ferroelectrics to exhibit spontaneous, switchable, electric polarization makes them extremely useful in a variety of technologies. Applications for ferroelectrics include data storage, computing, and sensing. Their implementation in capacitors makes ferroelectric materials vital components of energy storage and harvesting systems. An excellent overview of ferroelectricity and its applications can be found in [1].

Ferroelectric crystal structures must have a polar (noncentrosymmetric) space group. However, many materials which have a polar space group are not ferroelectric, either because the ions comprising the structure are not charged in a such a way as to induce finite polarization, or because the polarization is not switchable under the application of an electric field. In ferroelectric materials, the spontaneous polarization is the result of a particular arrangement of charged ions in the crystal lattice.

1.2.1 Perovskite Oxides

Ferroelectricity was first discovered in Rochelle salt, a hydrogen-bonded material [2]. The discovery of the perovskite oxide $BaTiO_3$ in 1949 [3] with its simple crystal structure provided an excellent platform to study the physics of ferroelectrics, and perovskite oxides remain the most highly studied family of ferroelectric oxide materials. The ideal perovskite structure, shown in Fig.1.1(a), has the space group $Pm\bar{3}m$ with a simple cu-

bic lattice and a 5-atom basis. Two of the possible polarization states are depicted in Fig.1.1(b,c), where the positively charged B cation is displaced from the center of an octahedron of six nearest-neighbor oxygen anions, with an A cation positioned at the corners of the unit cell. Depending on the structure, the direction of the polarization vector may be along various axes, and domains of different polarization orientations are possible in many materials.

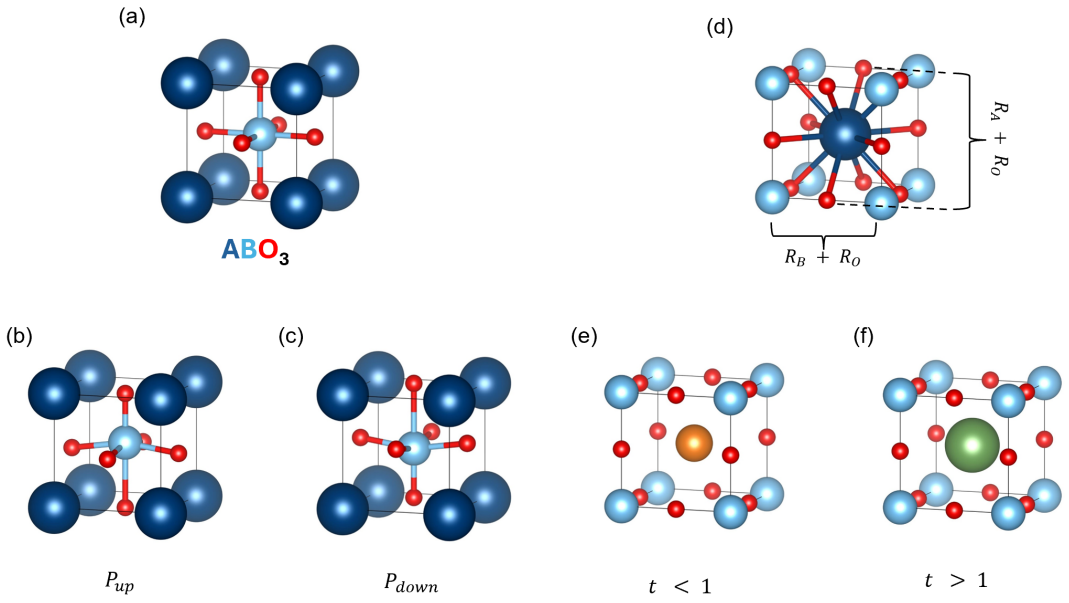

Figure 1.1: **Ferroelectric Perovskite Oxide** (a) Prototypical cubic perovskite structure (b) Polarization up state where cations and anions move in opposition to one another (c) Polarization down state (d) Different view of the perovskite structure, centered around the A atom (e) A smaller tolerance factor ($t < 1$), corresponds to loosely packed ions, and polar distortions are favored. (f) A larger tolerance factor ($t > 1$), corresponds to tightly packed ions, and octahedral rotations are favored. Figure adapted from [4].

In Fig.1.1(d), an alternative view of the crystal structure is presented where the A cation is positioned in the center of the unit cell, surrounded by twelve equidistant oxygen atoms. The relative size of the oxygen octahedra containing the B atoms and the A atoms occupying the holes between the octahedra determines whether a material takes on the prototypical perovksite structure. Following this logic, Goldschmidt [5]

provided a condition describing the ideal relation between ionic radii. The bond lengths $(r_A + r_o), (r_B + r_o)$ are depicted schematically in Fig.1.1(d), and the following relation between them is defined as the tolerance factor:

$$t = \frac{r_A + r_o}{\sqrt{2}(r_B + r_o)} \tag{1.1}$$

The perovskite oxide structure forms when $t \approx 1$. When $t > 1$ [Fig.1.1(e)], ions are loosely packed and the B atom is too small for the oxygen octahedron. The structure develops a small polar distortion, such as in $BaTiO_3$. When $t < 1$ [Fig.1.1(f)], the A atom is small in comparison to the space between the octahedra and the rotations or titling of the oxygen octahedra is favored. Owing to the ease of chemical substitution and the variety of polar and rotational distortions, the perovskite oxide family hosts a variety of diverse structural and physical properties.

1.2.2 Quantum Paraelectricity

In addition to finite, switchable polarization, a ferroelectric phase transition is characterized by a dielectric constant that diverges at low temperatures and a phonon mode that softens to zero at the ferroelectric transition temperature, T_c. It is possible for a material that is expected to be ferroelectric to avoid transitioning to an ordered phase due to quantum fluctuations between the two polarization states. Such a material is called a quantum paraelectric. The characteristic behavior of the soft mode frequency and the dielectric constant for ferroelectric and quantum paraelectric materials are compared in Fig.1.2. The softening of the phonon mode is aborted at the transition temperature of the quantum paraelectric phase [Fig.1.2(a)], and likewise the dielectric function saturates at the quantum paraelectric transition temperature [Fig.1.2(b)].

Strontium titanate ($SrTiO_3$), the primary material system studied in this thesis, is a

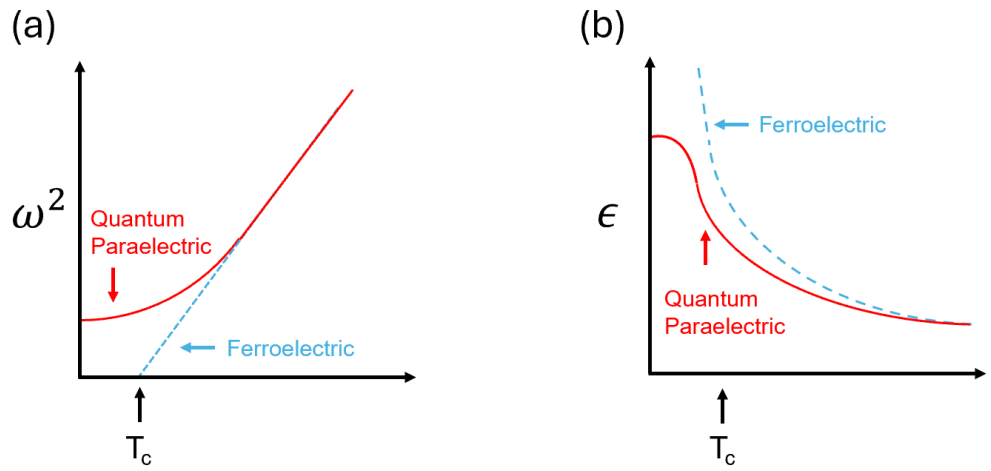

Figure 1.2: **Signatures of Quantum Paraelectricity** (a) Temperature dependence of the soft phonon mode. Here, T_c denotes the transition to either the ferroelectric phase (blue) where the mode softens completely to zero, or the quantum paraelectric phase (red), where the softening is aborted due to quantum fluctuations. (b) Temperature dependence of the dielectric function which diverges at T_c for a ferroelectric (blue) and saturates for a quantum paraelectric at T_c (red).

perovskite oxide and a quantum paraelectric in the bulk phase. Experimental measurements of the soft transverse optical mode and the dielectric electric constant as functions of temperature exhibit the expected behavior of the quantum paraelectric [6].

1.2.3 Polar metals

Polar metals are an example of a contra-indicated material: a material which enables the coexistence of phenomena typically considered to be mutually exclusive. Examples of contra-indicated properties include ferroelectricity and magnetism, or magnetism and superconductivity. An excellent review of polar metals can be found in [7].

Some clarifications should be made, from a semantic standpoint, about polar metals versus ferroelectrics. A polar space group possesses a polar direction (where two directional senses are inequivalent), which permits the existence of a permanent dipole

moment. The condition for ferroelectricity that there should be a measurable macroscopic polarization holds only for insulating systems. Furthermore, ferroelectricity requires switchability of the spontaneous polarization, which is not a requirement for polar metals. Thus, a polar metal is defined as a material with a polar space group with free carriers that lead to electronic conductivity.

Conventional ferroelectric materials are insulating. Whether ferroelectric order is achieved at low temperatures depends on the competition between two energies: short-range Coulomb repulsion and long-range dipole-dipole Coulomb interactions which favor the ferroelectric phase. These dipole-dipole interactions are screened by free carriers, so metallicity disfavors polar order. Most conventional metals adopt centrosymmetric structures due to the non-directionality of metallic bonding. Coulomb repulsion between ions is minimized at a particular density for evenly spaced ions. Additionally, chemical bonding that occurs between cations and ligands in the second-order Jahn-Teller effect leads to the off-centering of ions favored by empty valence shell cations, which are correlated with insulating behavior.

Anderson and Blout [8] suggested that a polar transition could occur in a metal if the metallic electrons do not interact strongly with the soft transverse optical phonons responsible for ferroelectricity. Polar metallicity can be achieved by doping polar semiconductors or adding carriers to conventional or unconventional ferroelectrics. Ferroelectrics driven by stereochemically active lone pairs that displace their host cations may be more robust to doping than those driven by the d^0 driven distortions, since the lone pairs are far from the Fermi level. Polar metals may posses nontrivial topological properties, or host unconventional superconducting phases. By tuning strain and other parameters, the polar phase of $SrTiO_3$ can be stabilized. When polar $SrTiO_3$ is doped, a polar metallic phase is achieved [9].

1.3 Quantum Criticality

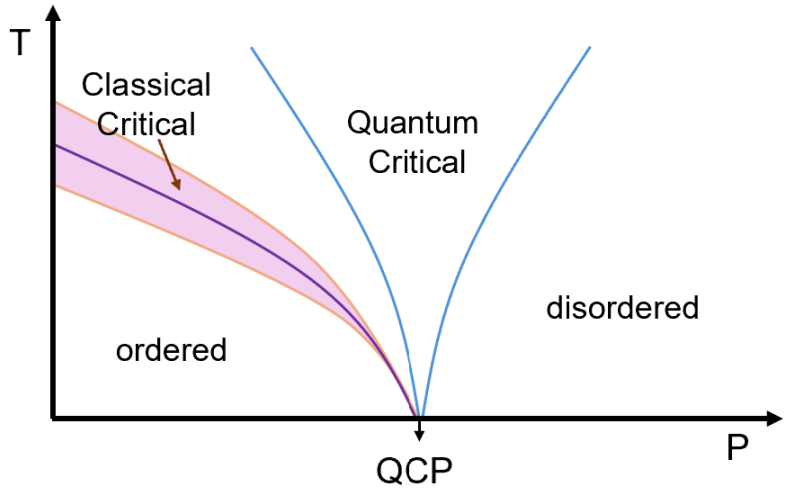

Figure 1.3: **Quantum Critical Phase Diagram.** The temperature dependence of the order parameters depends on a tuning parameter P. While the phase transition takes place at 0 K, quantum critical behavior fans out to finite temperatures in the vicinity of the quantum critical point (QCP).

In recent years, condensed matter physics research has revealed a new type of phase that is driven by quantum fluctuations associated with Heisenberg's uncertainty principle, rather than thermal fluctuations. When motion ceases at absolute zero, atoms and molecules cannot be at rest according to the uncertainty principle which states that the velocity and position of a particle cannot be simultaneously known with complete certainty. As a consequence of quantum uncertainty, atoms undergo zero-point motion at extremely low temperatures. If this zero-point motion becomes significant, it can "melt" order, much like thermal motion can melt ice. In the case of a quantum critical phase transition, this "melting" takes place at absolute zero.

A phase transition taking place at absolute zero cannot happen in practicality, but the quantum critical effects fan out through a finite-temperature regime, as depicted in Fig.1.3. This leads to interesting behavior, such as the fluctuation of bosonic order

parameters, which can facilitate Cooper pairing in superconductors. Since the phase transition is not driven by temperature, another tuning parameter (P) parameterizes the phase diagram [10]. In $SrTiO_3$, for example, strain or isotope substitution can drive the material from a quantum paraelectric into the polar phase [11].

1.4 Superconductivity

Superconductivity is characterized by two main properties: perfect conductivity and perfect diamagnetism. In a perfect conductor the resistivity is exactly zero, making the conductivity infinite. As a result, current can flow in a superconducting circuit indefinitely without the loss of energy to heat. A perfect diamagnet is completely impermeable to magnetic fields and expels any internal magnetic field.

Since the discovery of superconductivity in 1911 by Kamerlingh Onnes, superconductors have been implemented in a number of practical applications. Superconductors are currently used in MRI machines, particle accelerators, magnetic levitating transportation, and the detection of small magnetic fields. However, use of superconductors in technological applications is limited by the fact that they almost exclusively operate at extremely low temperatures, close to absolute zero.

Discovering new types of superconductors may expand their possible applications. These new functional materials will likely not adhere to the established theoretical paradigm for superconductivity. Future technologies of interest include lossless power transmission in high-temperature superconductors, and quantum computers which could use superconductors with non-trivial band topology to encode information. Unconventional superconductors provide an opportunity to discover novel physical phenomena and may open the door to technologies that are not yet imaginable.

1.4.1 BCS Theory

Before discussing unconventional superconductivity, we must first understand the conventional theory of superconductors presented by Bardeen, Cooper, and Schrieffer in 1957 [12]. Within the BCS paradigm, an attractive interaction between electrons results from the exchange of virtual phonons under the condition that the energy difference between the electronic states ($\Delta\epsilon$) is less than the phonon energy ($h\omega$). The discussion below will follow closely the description provided by Tinkham et al. [13].

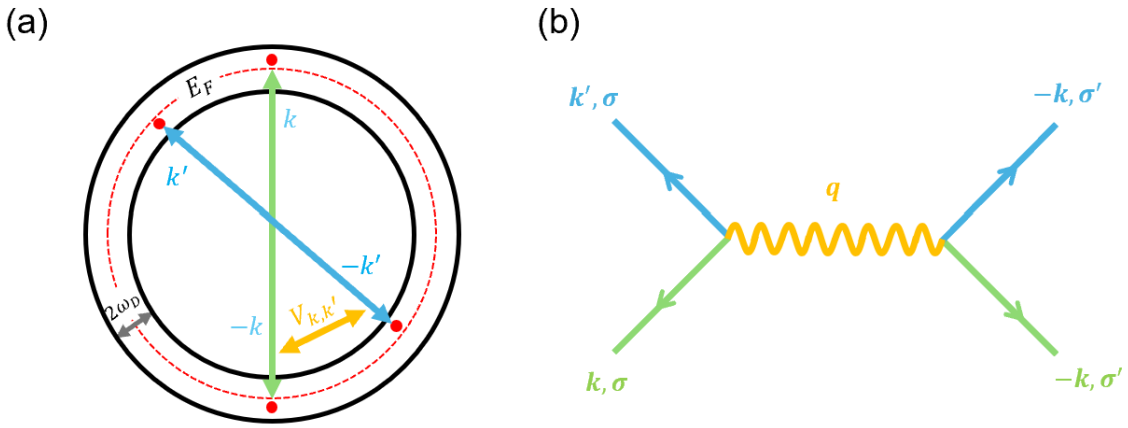

Figure 1.4: **Cooper Pairing** (a) Schematic of Cooper pairing of electrons within $2\omega_D$ of the Fermi energy E_F via the interaction energy $V_{k,k'}$. Figure adapted from [14]. (b) Feynman diagram of Cooper pairing via interaction with virtual phonon.

In his seminal 1956 paper, Cooper demonstrated that an arbitrarily small attractive interaction between two electrons will lower their energy, forming a bound state with negative energy with respect to the Fermi level [15]. To see how this might occur, we can consider two electrons within $\hbar\omega$ of the Fermi energy E_F, with $k > k_F$, such as those depicted in Fig.1.4(a), connected by the green arrow. The two-particle wave function describing these electrons will have zero total momentum, as this will minimize the total energy according to Bloch's theorem. The pair wavefunction is given by:

$$\psi_0(r_1, r_2) = \sum_k g_k e^{ik\cdot r_1} e^{-ik\cdot r_2} \tag{1.2}$$

Where (r_1, r_2) are the positions of the electrons, k represents a point in momentum space, and the values of g_k give the weighting coefficients of the eigenstates. Electrons are fermions, so the total wavefunction (ψ_0) must be antisymmetric; if the orbital component of the wavefunction is even, the spin component must be odd. From Eq.1.2, ψ_0 can be written as a sum of cosinusoidal products with an odd spin-singlet function $(\alpha_1\beta_2 - \beta_1\alpha_2)$, where α corresponds to spin-up and β to spin-down. Alternatively, one could write ψ_0 as sinusoidal products with an even spin-singlet function $(\alpha_1\beta_2 + \beta_1\alpha_2, \alpha_1\alpha_2, \beta_1\beta_2)$. The function $\cos(\mathbf{k}\cdot(r_1 - r_2))$ results in the highest probability that electrons will be in close spatial proximity to one another and most likely to pair, meaning that the accompanying form of the spin function should be a singlet to preserve the overall antisymmetry:

$$\psi_0(r_1, r_2) = \left[\sum_{k>k_F} g_{\mathbf{k}} cos\mathbf{k}\cdot(r_1 - r_2)\right](\alpha_1\beta_2 - \beta_1\alpha_2) \tag{1.3}$$

We can insert Eq.1.3 into the Schrodinger equation to determine the energy eigenvalue E and the weighting coefficients g_k:

$$(E - 2\epsilon_k)g_k = \sum_{k'>k_F} V_{kk'} g_{k'} \tag{1.4}$$

Here, $V_{kk'}$ is the magnitude of the scattering potential of a pair of electrons with momenta $(k', -k')$ to $(k, -k)$. This interaction $V_{kk'}$ is approximated according to the following condition:

$$V_{kk'} \begin{cases} -V & \text{for } \zeta_k \leq \hbar\omega_c \\ 0 & \text{otherwise} \end{cases} \tag{1.5}$$

Where $\zeta_k = \epsilon_k - E_F$ is the energy of an electron relative to the Fermi surface. By replacing the sum in Eq.1.4 with an integral and simplifying we obtain:

$$\frac{1}{V} = N(0) \int_{E_F}^{E_F + \hbar\omega_c} \frac{d\epsilon}{2\epsilon - E} = \frac{1}{2} N(0) ln \frac{E_F - E + 2\hbar\omega_c}{2E_F - E} \tag{1.6}$$

Where $N(0)$ is the density of states at the Fermi level. Assuming weak coupling, $N(0)V << 1$, a condition that is met in most superconductors, we can write Eq.1.6 as:

$$E \approx 2E_F - 2\hbar\omega_c E^{-2/N(0)V} \tag{1.7}$$

We have shown in Eq.1.7 that an arbitrarily small potential (V), so long as it is attractive, will outweigh the excess kinetic energy for a pair of electrons with $k > k_F$, forming a bound state with $E < E_F$, shown in Fig.1.4(a) as states connected by the blue arrow. However, there must be justification for why $V_{kk'}$ should be negative.

After accounting for the bare Coulomb interaction $V(r) = (e^2/r)$ and the dielectric function of the medium ($\epsilon = 1 + k_s^2/q^2$) which incorporates the screening effect of the conduction electrons, we are still left with a positive interaction potential. An attractive interaction only occurs when the interaction of the electrons with the lattice vibrations (phonons) is considered.

$$V_{k,k'}^{eff} = \frac{4\pi e^2}{q^2 + k_{TF}^2} + \frac{4\pi e^2}{q^2 + k_{TF}^2} \frac{\omega_q^2}{\omega^2 - \omega_q^2} \tag{1.8}$$

In Eq.1.8, a solid material is modeled as a fluid of electrons containing point ions, referred to as the "jellium" model. If momentum is conserved scattering a phonon from **k** to **k'**, the phonon must have momentum $\mathbf{q} = \mathbf{k} - \mathbf{k}'$. From the last resonance term in Eq.1.8, we get a net negative interaction when $\omega < \omega_q$. The cutoff energy for an attractive $V_{k,k'}^{eff}$ is on the order of the Debye energy $\hbar\omega_D$, which characterizes the cutoff

of the phonon spectrum.

Phonon-mediated pairing, subject to the condition that phonon frequency must be slow compared to the energy of the electrons, can be understood intuitively as follows: if lattice deformation is slow compared to the velocity of the electrons, by the time the lattice deforms in response to the motion of one electron, the first electron will be far away by the time a second electron is attracted to the modulation of charge density generated by the motion of the first electron through the lattice. In this framework, it is justified to ignore Coulomb repulsion between electrons.

Following the processes described above, electrons can form bosonic quasiparticles called Cooper pairs with spin zero and an effective charge of negative two. These quasiparticles condense into a single coherent quantum state, the Bose-Einstein condensate, that can be described by a many-body wavefunction. Superconductivity is an example of a quantum phenomenon that can be observed on a macroscopic scale.

The order parameter which characterizes the superconducting phase transition is the energy gap Δ, where an energy of 2Δ is required to destroy a Cooper pair. The gap results from the hybridization of electron-like and hole-like quasiparticles, which leads to the formation of new quasiparticles, called *Bogoliubons*, that act as superposition of electron and holes. The energy gap is subject to a similar condition as the interaction potential in Eq.1.4:

$$\Delta_k = \begin{cases} \Delta & \text{for } |\zeta_k| < \hbar\omega_c \\ 0 & \text{otherwise} \end{cases} \tag{1.9}$$

Properties of BCS Cooper Pairs

1. Opposite spin ($|\uparrow\rangle, |\downarrow\rangle$)
2. Isotropic gap ($\Delta_k = \Delta$)
3. Zero total momentum ($|k\rangle, |-k\rangle$)
4. Slow phonons, fast electrons ($\omega_D << E_F$)

In summary, a conventional Cooper pair consists of time-reversed quasiparticle states that form an antisymmetric spin singlet with a symmetric, nodeless orbital component of the wavefunction, and a superconducting energy gap that is isotropic reciprocal space. The attractive interaction is mediated by exchange of a virtual phonon with $\hbar\omega << E_F$.

1.4.2 Unconventional Superconductivity

In an unconventional superconductor, the nature of Cooper pairing deviates from the conditions outlined by BCS theory. This can manifest in a variety of ways depending on the material system. In the previous section, we discussed how the pair wavefunction can be decomposed into its spin and orbital components. Here, we will write the total wavefunction as, $\Psi_{k,ss'} = \phi(k)\chi_{ss'}$, with $\phi(k)$ representing the orbital component and $\chi_{ss'}$ representing the spin component with (s, s') indicating the spins of the two electrons. The parity of the wavefunction is related to the angular momentum, with even parity corresponding to $l = 0, 2, 4$ and odd parity $l = 1, 3, 5$, analogous to angular momentum of electronic orbitals. Conventional s-wave pairing is spherically symmetric with $l = 0$, and all states with $l \neq 0$ are considered unconventional [16]. To preserve the total antisymmetry of Ψ, the orbital and spin components of must have opposite parity, as outlined in Tab.1.1. An odd orbital wavefunction is accompanied by a spin-triplet pairing, with three possible pairing channels. The superconducting energy gap will reflect the symmetry of the pair wave function.

Table 1.1: Conditions for even and odd pairing symmetries, adapted from[16]

Pairing Type	Orbital	Spin
Even Parity	$\phi(\vec{k}) = +\phi(-\vec{k})$	$\chi(ss') = \frac{1}{\sqrt{2}}(\|\uparrow\downarrow\rangle - \|\downarrow\uparrow\rangle)$
Odd Parity	$\phi(\vec{k}) = -\phi(-\vec{k})$	$\chi(ss') = \begin{cases} \|\uparrow\uparrow\rangle \\ \frac{1}{\sqrt{2}}(\|\uparrow\downarrow\rangle + \|\downarrow\uparrow\rangle) \\ \|\downarrow\downarrow\rangle \end{cases}$

For an even parity gap, we can write a 2×2 matrix in spin space represented by a scalar function Ψ, where $\Psi(-k) = \Psi(k)$:

$$\Delta(\vec{k}) = i\Psi(\vec{k})\hat{\sigma}^y = \begin{bmatrix} 0 & -\psi \\ \psi & 0 \end{bmatrix} \tag{1.10}$$

For odd parity spin-triplet superconductors, we use the odd vector function $d(\vec{k})$, where $d(\vec{k}) = -d(-\vec{k})$:

$$\Delta(\vec{k}) = i\vec{d}(\vec{k}) \cdot \hat{\vec{\sigma}}\hat{\sigma}^y = \begin{bmatrix} -d_x(k) + id_y(k) & d_z(k) \\ d_z(k) & d_x(k) + id_y(k) \end{bmatrix} \tag{1.11}$$

Depending on the specific form of $d(k)$, the superconducting gap can take on different symmetries, some examples of which are shown in Fig.1.5. Other possible symmetries which are not shown here include f-wave, or $p_x + ip_y$.

Although p-wave pairing [Fig.1.5(b)] has been experimentally observed in the superfluid ^{3}He [18], it can be difficult to obtain definitive evidence for the symmetry of the order parameter since the thermodynamic signatures for p-wave pairing can often resemble that of s- or d-wave superconductors. Materials which are posited to have potential p-wave pairing states include Fe-based superconductors, such as NdFeAs(O,F) [19].

The cuprate family of high-temperature superconductors is an example of unconventional d-wave pairing symmetry[Fig. 1.5(c)]. Cuprate crystals contain 2D planes of Cu

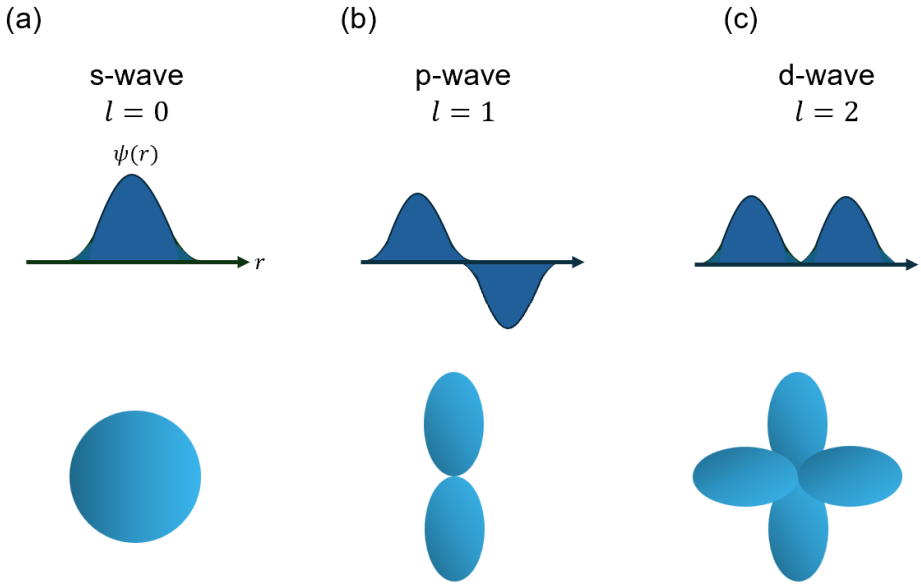

Figure 1.5: **Superconducting Gap Symmetries** (a) Conventional s-wave superconductivity. Cooper pairs are spin singlets with an isotropic gap. (b) Unconventional odd parity p-wave pairing. (c) Unconventional even parity d-wave pairing. Figure adapted from [17].

and O atoms arranged in a square lattice within 2D planes that order into antiferromagnetic Mott insulating ground state. Upon hole doping, superconductivity emerges with critical temperatures of up to 145 K. The superconducting state is characterized by the strong $d_{x^2-y^2}$ symmetry of the energy gap, where electrons pair strongly parallel to the Cu-O-Cu bond directions, but do not pair along the diagonals of the square lattice. This directional dependence of the pairing strength manifests in the symmetry of the gap function in reciprocal space [20].

In materials where the phonon frequency is fast relative to the velocity of the electrons, phonon-mediated pairing may not be sufficient to overcome Coulomb repulsion and an unconventional pairing glue may be required. The superconducting critical temperature is limited by the adiabatic criterion ($\hbar\omega > E_F$), so other pairing glues may be the key to discovering new high-temperature superconductors. When superconductivity

occurs near a second-order phase transition that has been suppressed to $T = 0$ K, critical fluctuations of a bosonic order parameter may mediate pairing. Spin fluctuations in materials with strong antiferromagnetic exchange interactions, such as the cuprates, are posited to mediate superconductivity [21]. Other families of unconventional superconductors include heavy fermion materials, where localized f electrons actively participate in pairing. Due to their large effective mass, certain heavy fermion materials are candidates for the Fulde–Ferrell–Larkin-Ovchinnikov (FFLO) phase, in which Cooper pairs have finite momentum [22].

In addition to providing possible routes to high-temperature superconductivity, unconventional superconductors, particularly those with odd or mixed parity, can possess nontrivial band topology. Topological superconductors can give rise to emergent quasiparticles whose properties can be harnessed for use in practical applications, such as quantum computing.

Strontium titanate is not only a quantum paraelectric which can be tuned into a polar metallic state, it is also superconductor with a critical temperature on the order of several hundred millikelvin. The adiabatic criterion is not met in $SrTiO_3$, making it an unconventional superconductor. The unconventional nature of the superconducting phase will be discussed in detail in Chapter 4.

1.5 Topological Materials

While the computational methods used in this thesis do not explicitly involve topological classifications of materials, the search for materials systems with nontrivial topology is the underlying motivation for each project. It is therefore worthwhile to understand what topological materials are and how they can be used. It is of particular interest to discover superconductors with nontrivial topology because of their potential applications

in quantum computing technology.

Broadly speaking, topology is a mathematical concept used to classify geometries. When two geometries can be continuously deformed into one another, such as a donut and a coffee mug, they are said to have the same topology. Similarly, when one Hamiltonian can be adiabatically transformed into another without closing the energy gap, they are considered topologically equivalent.

1.5.1 Topological Insulators

Before discussing topological superconductors, it is helpful to understand the basic characteristics of topological insulators. Topological insulators are distinct from either metals or insulators. A metal contains half-filled bands which allows electrons to move freely to unoccupied states within the same band, allowing for electrical conduction. In an insulator, however, there is an energy gap between a valence band of filled electronic states and a conduction band of unfilled states. In the atomic limit, electrons are completely localized onto individual atoms. The Hamiltonian of a topological insulator cannot be adiabatically transformed into that of an atomic insulator without closing the energy gap. Therefore, a topological insulator necessarily contains topologically protected gapless (conducting) edge states. These states typically exist on the surface of the material, where the nontrivial topology of the bulk must transition to the trivial topology of the vacuum, thus closing the energy gap. This transition from nontrivial to trivial topology is accompanied by a mixing of the valence and conduction band states referred to as band inversion. The phenomenon of characteristics of the bulk band structure affecting states at the surface is known as *bulk-boundary correspondence*.

In topological band theory, classifications are made by computing a number called a topological invariant. If a material is topologically nontrivial, the wavefunctions of the

Hamiltonian may have a twist in the parameter space that defines its eigenstates. A quantity called the Berry phase (λ) can be used to quantify these twists in parameter space, which in the context of electronic band structures is momentum space.

$$\lambda = \oint_P A(\lambda) \cdot d\lambda \tag{1.12}$$

The Berry connection, $A(\lambda)=\langle u_\lambda | \, i\partial_\lambda \, | u_\lambda \rangle$, measures the rate of change of the wavefunction in momentum space. The Berry curvature is defined as $\Omega = \nabla \times A$. According to the Chern theorem, the Berry curvature of a fully closed loop in momentum space is quantized.

$$2\pi C = \oint_S \Omega \cdot dS \tag{1.13}$$

Here, C is the topological invariant known as the Chern number. The Chern number can be used to classify topological materials according to their Hamiltonians, under the constraints required by different symmetries [23].

1.5.2 Topological Superconductors

Topological superconductors are distinct from the Bose-Einstein condensate of Cooper pairs which forms a trivial superconducting state, just as topological insulators are distinct from the trivial limit of an atomic insulator. To understand how the topological invariant is defined for superconductors, where there is no gap between the valence and conduction bands, we must consider a special symmetry of superconductors: particle-hole symmetry.

A superconductor creates and annihilates pairs of electrons from the Fermi sea by breaking apart and forming Cooper pairs. The effective Hamiltonian for a superconduct-

ing ground state is given by:

$$\mathcal{H} = \sum_{nm} H_{nm} c_n^\dagger c_m + \frac{1}{2}\left(\Delta_{nm} c_n^\dagger c_m^\dagger + \Delta_{nm}^* c_n c_m\right) \tag{1.14}$$

Note that this expression $\mathcal{H}$ does not conserve the number of electrons, since Cooper pairs are being created (annihilated) by the operators $c(c^\dagger)$. However, the parity of the electrons, whether the number of electrons is even or odd, is conserved, since Cooper pairs are comprised of two electrons. By grouping the creation and annihilation operators into a vector, we can write $\mathcal{H}$ as:

$$\mathcal{H} = \frac{1}{2} C^\dagger H_{BdG} C \tag{1.15}$$

The Bogoliubov-de Gennes (BdG) Hamiltonian (H_{BdG}) has the following structure:

$$\psi = \begin{bmatrix} H & \Delta \\ -\Delta^* & -H^* \end{bmatrix}$$

The BdG Hamiltonian acts on wavefunctions whose first half consists of annihilation operators of electrons, and whose second half contains creation operators of those same electrons. The creation operators can be thought of as annihilation operators of an extra set of holes, which effectively doubles the number of degrees of freedom in the system. The H_{BdG} automatically has an extra symmetry that exchanges electrons with holes, and has an antiunitary operator that acts on the hole blocks.

The spectrum of H_{BdG} must be symmetric about zero, where zero energy corresponds to the Fermi level. For each eigenvector with energy E, a symmetric particle-hole eigenvector exists with energy $-E$. The negative energy states are all filled, much like in a topological insulator, which allows topological invariants to be defined for superconductors. Considering one H_{BdG} Hamiltonian being transformed into another, the energy crossings, which typically occur in the presence of a conserved quantity, are associated

with changes in fermion parity, which is the conserved quantity in a superconductor due to particle hole symmetry.

Majorana Fermions

The emergence of special particles, called Majorana fermions, is a prominent feature of topological superconductors which renders them of great practical interest to physicists. In 1937, Majorana found that the Dirac equation describes a particle that is its own antiparticle [24]. Majorana fermions may exist as emergent collective excitations of electrons at the boundaries of topological superconductors, or within certain spin liquid states [23].

In order for a collective excitation to classify as a Majorana fermion, the excitation must (1) obey the Dirac equation (2) be its own antiparticle. Gapless excitations which obey the Dirac equation arise due to bulk-boundary correspondence in a topological superconductor. As a consequence of particle-hole symmetry, electron and hole states are indistinguishable in the superconducting state, making the topological gapless boundary excitations Majorana fermions.

Majorana fermions obey non-abelian statistics, which characterizes their symmetries under the exchange of two particles. The wavefunction of a fermion is antisymmetric under exchange, while that of a boson is symmetric under exchange. This wavefunction symmetry underlies the Pauli exclusion principle, superfluidity, metallicity, Bose-Einstein condensation, and more. In three dimensions, only bosons and fermions exist. In two dimensions, however, a particle loop that encircles another particle cannot be deformed to a point without cutting through the other particle, as depicted in Fig.1.6(b). So, when two particles are interchanged twice in a clockwise manner, the system does not necessarily come back to the same state (Fig.1.6(c). When one particle is exchanged in a

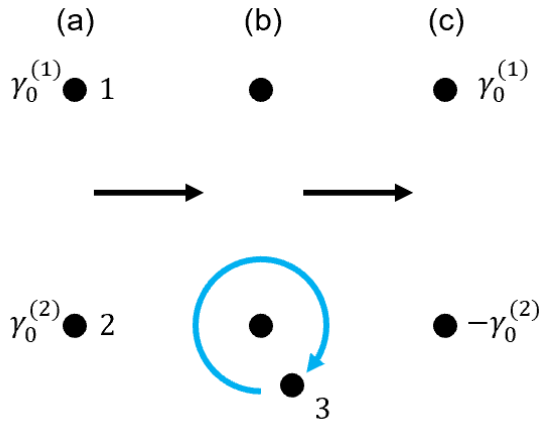

Figure 1.6: **Exchange of Majoranas** (a) Initial state of two Majorana fermions (1) and (2) with operators $\gamma_0^{(1)}$ and $\gamma_0^{(2)}$ (b) A third Majorana (1) is braided around (2). (c) Due to the non-abelian statistics of Majorana anyons, $\gamma_0^{(2)} \rightarrow -\gamma_0^{(2)}$. Figure adapted from [23].

counterclockwise manner with the other, the wavefunction picks up an arbitrary phase.

$$\psi(r_1, r_2) \rightarrow e^{i\theta}\psi(r_1, r_2) \tag{1.16}$$

A second clockwise exchange may lead to a state distinct from the initial state with a nontrivial phase.

$$\psi(r_1, r_2) \rightarrow e^{2i\theta}\psi(r_1, r_2) \tag{1.17}$$

The cases where $\theta = 0, \pi$ correspond to bosons and fermions, respectively. Particles with other values of this statistical angle are called anyons. Let's consider a quantum state $|\Psi\rangle$ with a ground state manifold of 2^N where two Majoranas are exchanged and the initial and final quantum states are connected by a unitary operator U written as a $2^N \times 2^N$ matrix. To exchange Majoranas γ_m and γ_n, we have the operator U defined as:

$$U = exp\left(\pm\frac{\pi}{4}\gamma_n\gamma_m\right) = \frac{1}{\sqrt{2}}\left(1 \pm \gamma_n\gamma_m\right) \tag{1.18}$$

For the braiding process in Fig.1.6 where γ_m and γ_n are exchanged twice we have:

$$(U_{23})^2\gamma_0^2(U_{23}^\dagger)^2 = -\gamma_0^2 \tag{1.19}$$

$$(U_{23})^2\gamma_0^3(U_{23}^\dagger)^2 = -\gamma_0^3 \tag{1.20}$$

$$U_{23}U_{12} \neq U_{12}U_{23} \tag{1.21}$$

The operators U_{12} and U_{23} do not commute, making this exchange process non-abelian.

The braiding of non-abelian anyons like Majoranas can be used to perform quantum computations. A network of $2N$ Majoranas can be thought of as a small computer with N bits. Unlike in a classical computer, this register of bits can exist in a superposition of states. By exchanging Majorana modes, different sequences of exchanges will yield different algorithms. The state of this register is encoded in the fermion parity degrees of freedom which are shared non-locally by the Majoranas. This means the information is topologically protected against decoherence. The environment cannot access the stored information so long as the Majoranas are kept far away from each other. Decoherence is a major barrier to engineering robust quantum computing platforms, and thus Majoranas could provide a solution [25].

There are several routes to engineer superconducting systems with non-trivial topology at an interface, or at the ends of a nanowire. However, it is of interest to discover so-called *natively entangled* materials that posses intrinsic topological properties without the need for device engineering. One possible route to such a system is through an odd-parity superconducting state, which can occur in a noncentrosymmetric material in the presence of strong antisymmetric spin-orbit coupling.

1.5.3 Topological Properties of Noncentrosymmetric Superconductors

Non-centrosymmetric superconductors (NCS) lack a center of inversion and therefore parity symmetry ($|k\rangle \rightarrow |-k\rangle$) no longer exists. $SrTiO_3$, within the polar phase, is an example of a noncentrosymmetric superconductor. The pairing symmetries of spin-singlet and spin-triplet Cooper pairs are given by $\Delta(k) = \psi(k)i\sigma_y$ and $\Delta(k) = i\Delta_0 d(k) \cdot \sigma\sigma_y$, respectively. As a consequence of the Pauli exclusion principle, spin-singlet states are even under inversion, and spin-triplet states are odd under inversion. Removing parity symmetry eliminates the strict separation between singlet and triplet states, allowing them to mix [26], giving the following expression for pairing:

$$\Delta(k) = \psi(k)i\sigma_y + d(k) \cdot i\sigma\sigma_y \tag{1.22}$$

While inversion symmetry breaking removes the constraint that separates singlet and triplet states, another ingredient is necessary to provide the specific mechanism for mixing. This missing ingredient is antisymmetric spin-orbit coupling (ASOC). Symmetric

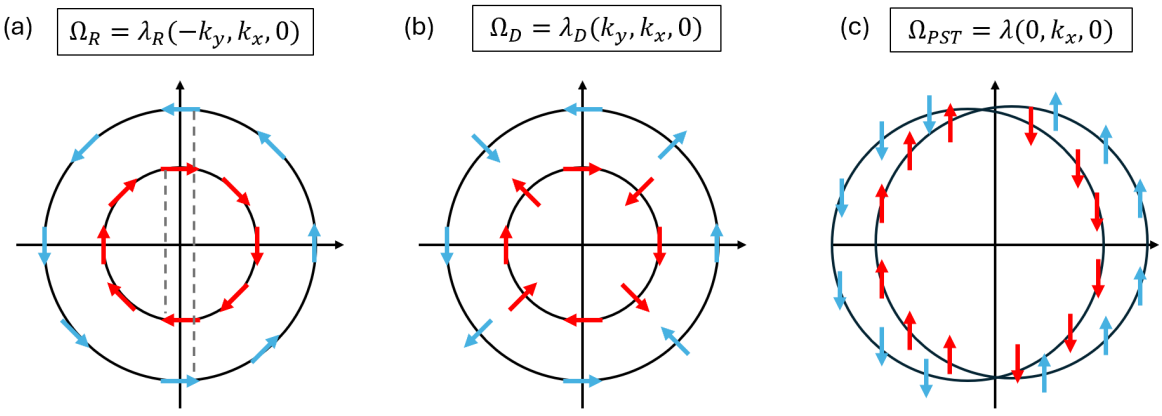

Figure 1.7: **Spin Textures induced by ASOC** (a) Rashba spin texture (b) Dresselhouse spin texture (c). Persistent spin texture (PST).

spin-orbit coupling is a relativistic effect through which the spin and orbital angular momentum become correlated due to the magnetic field generated by the accelerating positive nucleus in the reference frame of the electron. The spin-orbit coupling interaction in centrosymmetric systems is given by:

$$H_{SO} = \zeta(r)\mathbf{L} \cdot \mathbf{S} \tag{1.23}$$

Where $\zeta(r)$ is a radial function of the distance r from the nucleus, $\mathbf{L}$ is the orbital angular momentum and S is the spin angular momentum. Spin-orbit coupling leads to the splitting of electronic eigenstates observable in the hyper-fine splitting of the hydrogen spectrum.

In the absence of inversion symmetry, the strength of the spin orbit coupling interaction becomes momentum-dependent leading to spin orbit coupling that is asymmetric throughout momentum space. The antisymmetric spin orbit coupling interaction is given by:

$$H_{ASOC} = S \cdot (k \times E) \tag{1.24}$$

Where k is the electron wave vector and E is an effective electric field which is typically perpendicular to the plane in which inversion symmetry is broken. This effective electric field arises due to the variation in the potential felt by the electrons due the symmetry of the underlying lattice. As a consequence of this momentum-dependent electric field, the expectation value of the spin becomes dependent on the direction of k, resulting in diverse spin textures in reciprocal space. This correlation between the spin and momentum is referred to as *spin-momentum locking*.

There are three basic forms of spin textures resulting from ASOC, which are depicted in Fig.1.7 . The type of spin texture that arises in a specific materials system will depend

on the symmetries of the crystal. Linear combinations of these effective fields are also possible [27]. We will focus primarily on Rashba spin-orbit coupling (RSOC), as it is most relevant to $SrTiO_3$ which will discussed in Chapter 4. The RSOC interaction term is given by:

$$H_{RSOC} = \alpha \left(k \times \sigma\right) \cdot \hat{z} = \alpha \left(k_y \sigma_x - k_x \sigma_y\right) \tag{1.25}$$

Where α is the Rashba coupling constant, $\mathbf{k} = (k_x, k_y)$ is the electron wave vector in the plane, and $(\hat{z})$ is the direction of the effective electric field. For a given value of $\mathbf{k}$, spins couple to the momentum differently based on whether they are aligned parallel or anti-parallel to the effective magnetic field $B_{eff} = \alpha(\mathbf{k} \times \hat{z})$. The presence of B_{eff} breaks the degeneracy between spin states at each k-point, known as Kramer's degeneracy. Kramer's degeneracy is typically protected in centrosymmetric systems by parity $\mathcal{P}\left|k,\uparrow\right\rangle = \left|-k,\uparrow\right\rangle$and time-reversal $\mathcal{T}\left|k,\uparrow\right\rangle = \left|-k,\uparrow\right\rangle$ symmetries, giving the Kramer's pair:

$$\mathcal{P}\mathcal{T}\left|k,\uparrow\right\rangle = \left|k,\downarrow\right\rangle \tag{1.26}$$

Lifting the Kramer's degeneracy splits the energy bands, leading to the two helical bands with opposite spin textures, shown in Fig.1.7(a). In a noncentrosymmetric Rashba superconductor, if the RSOC interaction is sufficiently strong, the gap between helical bands is large enough that Cooper pairing between electrons on different bands can be ignored, giving the following expressions in the helicity basis for singlet and mixed parity pairing, respectively:

$$\left\langle\psi_s\right| = \frac{1}{\sqrt{2}} \left(\left\langle k,\uparrow\right| \left\langle -k,\downarrow\right| - \left\langle k,\downarrow\right| \left\langle -k,\uparrow\right|\right) \tag{1.27}$$

$$\left\langle\psi_{sp}\right| = \frac{i}{2\sqrt{2}} \left(-e^{-i\phi_k} \left\langle k,\uparrow\right| \left\langle -k,\downarrow\right| + e^{-i\phi_k} \left\langle k,\downarrow\right| \left\langle -k,\uparrow\right|\right) \tag{1.28}$$

Coupling takes place between electrons of opposite spin within the same band, indicated by the dashed lines in Fig.1.7(a). Note that there are no same-spin Cooper pairs. There

is no physical reason why the superconducting gap must be the same for both helicity bands, and indeed the presence of different gap magnitudes is an experimental signature of mixed parity [26].

The possibility of mixed-parity states has interesting consequences. In 2015 Kozii and Fu [28] proposed that in the presence of spin-orbit coupling, fluctuations of incipient parity-breaking order generate an attractive pairing interaction in an odd-parity pairing channel which competes with s-wave pairing. They demonstrated that Coulomb repulsion or an external Zeeman field suppresses the s-wave pairing and promotes the odd-parity superconducting state.

Wang et al. [29] expounded on this idea, demonstrating that the degeneracy between s- and p-wave superconducting order parameters was a result of the conserved fermionic helicity χ, and the two degenerate channels correspond to even and odd combinations of superconducting order parameters with $\chi = \pm 1$. As a result, the system has an enlarged symmetry $U(1) \times U(1)$, with each $U(1)$ corresponding to one value of the helicity χ. The enlarged symmetry allows for exotic topological defects like a fractional quantum vortex, which has a Majorana zero mode bound at its core.

In the polar phase, strontium titanate is a noncentrosymmetric superconductor. Signatures of mixed parity superconductivity have been predicted theoretically, and also observed experimentally by nonreciprocal charge transport measurements [30]. The unconventional and possibly topological nature of superconductivity in $SrTiO_3$ is our main motivation for studying this material.

1.6 Charge Density Waves

A charge density wave (CDW) is a static modulation of conduction electrons which lowers the electronic energy due to distortions of the underlying lattice. A clear example

of this is a Pierels distortion, depicted in Fig.1.8. Pierels suggested that a one-dimensional chain of atoms is susceptible to a distortion of the lattice which changes the periodicity. In Fig.1.8(a), the typical energy versus momentum dispersion is shown for a monovalent metal. The first Brillouin zone is half occupied and the periodic charge density is localized around the ion cores. Fig.1.8(b) shows a lattice distortion that doubles the size of the unit cell in real space, opening an energy gap at the zone boundary. This lowers the energy of the electrons at the Fermi energy and shifts the Fermi energy downwards. In this case, the periodic lattice distortion has a purely electronic origin. This process is referred to

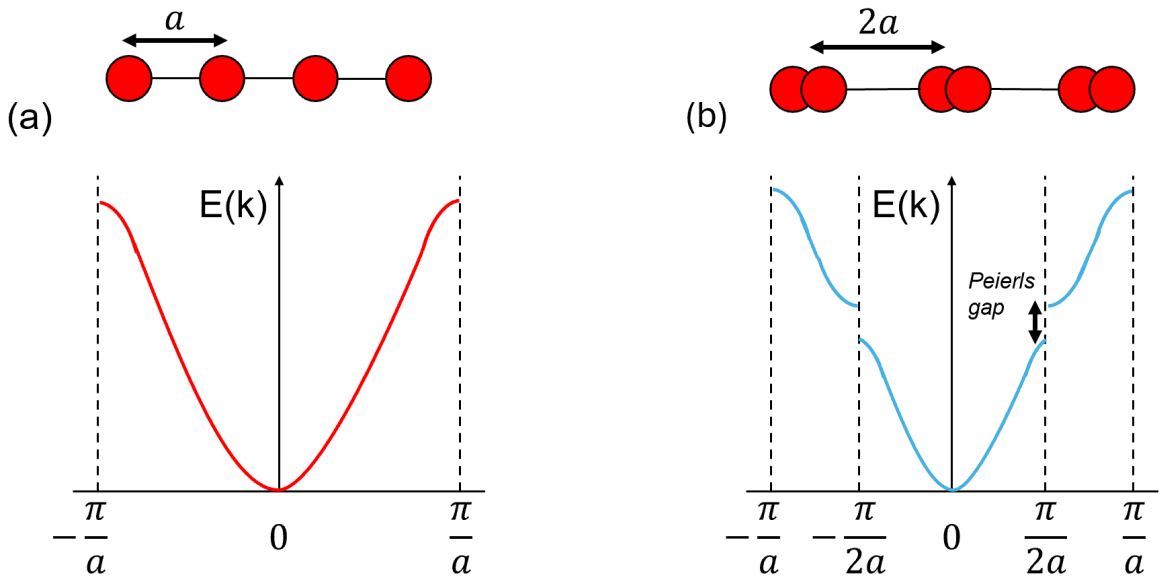

Figure 1.8: **Pierels Instability** (a) Band structure of a monovalent metal (b). Below the charge density wave transition, the unit cell doubles, opening an energy gap and lowering the Fermi energy.

as Fermi surface nesting and will occur when the Fermi surface permits a connection by the same wavevector Q. The modulation with wavevector Q will create gaps in the Fermi surface corresponding to the nested positions. If the energy gain obtained by creating the energy gaps overcomes the energy cost of the lattice distortion, the formation of a CDW will be favored [31].

In addition to a favorable geometry of the Fermi surface, strong electron-phonon coupling is also a requirement for CDW formation. If the electron-phonon interaction is not sufficient, the Coulomb repulsion caused by the lattice distortion will become prohibitive and a CDW transition will not occur.

Similar to CDW transitions, superconducting transitions are typically mediated by an attractive electron-phonon mechanism. It can therefore be expected that systems with CDW may also exhibit superconductivity at low temperatures. However, superconducting and CDW transitions are somewhat antithetical to one another. While a superconductor has infinite conductivity, the CDW state produces a semiconductor gap in the electronic energy dispersion, resulting in a nonconducting state. Furthermore, the microscopic mechanisms of superconducting and CDW transitions are distinct: superconductivity arises from electron-electron coupling into Cooper pairs mediated by virtual phonon exchange, while CDW arises from electron-hole coupling and charge redistribution.

The natural competition between superconducting and CDW order makes their coexistence unusual and indicates the possibility of unconventional superconductivity. The recently discovered family of kagome metals exhibits a charge density wave transition followed by a superconducting transition at lower temperatures. In Chapter 6, the nature of the charge density wave order in CsV_3Sb_5 is characterized using first-principles calculations, which support findings from experimental measurements of coherent phonon spectroscopy.

1.7 Quantum Spin Liquids

In the context of physics, "frustration" refers to the presence of competing forces that cannot be satisfied simultaneously. When magnetic moments, or spins, are localized on

atoms with certain geometric arrangements, competing exchange interactions between these spins make it impossible for the desired ground state to be acquired, thus giving rise to geometric frustration of the spins. Such materials are called frustrated magnets. Under a particular set of conditions, this geometric frustration of magnetic moments can lead to states of matter where spins fluctuate strongly down to zero temperature despite strong magnetic exchange interactions. For materials with large spin $s >> 1/2$, fluctuations of magnetic moments tend to be classical, and driven by thermal energy as they cycle through different microstates, randomly reorienting with time. Classical spin liquids usually freeze into a static order when $k_B T$ becomes too small [32].

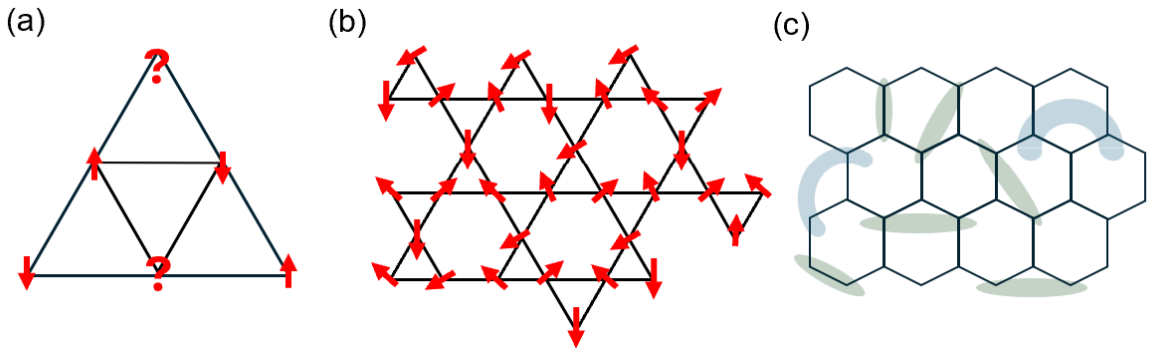

Figure 1.9: **Frustrated Magnetism** (a) In a triangular lattice, an antiferromagnetic ground state configuration is not possible. Question marks represent undetermined spins which are not able to satisfy the antiferromagnetic exchange interaction. (b) Frustrated spins on a kagome lattice can be in a superposition of many states at once. (c) Shaded ellipses represent spin singlets with $S = 0$ on a Kagome lattice. Figure adpated from [33].

For materials with smaller values of spin $s = 1/2$, quantum fluctuations due to the uncertainty principle are comparable to the size of the spin, and the fluctuations persist to absolute zero. If phase coherent quantum fluctuations are strong enough, the result is a quantum spin liquid (QSL). The ground state of a QSL is a superposition of many possible spin orientations. In other words, the spins are in a superposition of pointing in many directions at one, and they are highly entangled with one another.

Quantum entanglement between two states means that the result of a measurement of an observable affects the outcome of measurements, even when the observables are independent of one another. States of two observables can range from disentangled product states to maximally entangled states. The most intriguing implication of the many-body entanglement of spins in a QSL is the ability of these states to host non-local excitations. These excitations can have finite energy and behave as quasiparticles such as solitons, spinons, orbitons, and chargons.

In a quantum spin liquid, the many-body entanglement in the highly degenerate ground state can give rise to non-local excitations, or the fractionalization of elementary particles into quasiparticles, emergent gauge fields, and long-range entanglement. In topological quantum spin liquids, information can be encoded and topologically protected, with a higher ability to withstand decoherence than topological superconducting systems of qubits, and thus quantum spin liquids could be a promising platform for quantum computing.

Experimental verification of a QSL state is challenging. A QSL does not break fundamental lattice symmetries, and there is no local order parameter that describes the transition. When identifying a QSL, one must first show the absence of magnetic order down to low temperature, and the presence of strong, usually antiferromagnetic, superexchange interactions. Measurements of the magnetic susceptibility, heat capacity, or neutron diffraction patterns can be used to confirm the absence of magnetic order. Nuclear magnetic resonance and muon spectroscopy can detect spin freezing [33].

However, all of these things identify what a spin liquid is *not*, and may not definitively confirm the existence of a QSL ground state. For instance, the absence of magnetic order could be caused by the disorder of the lattice. The key features defining a QSL are long-range entanglement and the associated fractional spin excitations. It is difficult to characterize long-range entanglement, so we focus on the fractional excitations. For

example, spinons are deconfined from the crystal lattice and have their own dispersions. For U(1) gapless QSLs, spinons form a Fermi sea, similar to that of a metal. Techniques sensitive to magnetic excitations, like neutron scattering, thermal conductivity and thermal hall conductivity, electron spin resonance, specific heat, as well as Raman and THz spectroscopy, can be utilized to clarify whether fractionalized excitations are present.

The search for new quantum spin liquid candidates is an active field of research in condensed matter physics. One of the most promising materials candidates to date is herbertsmithite. In Chapter 7, we perform a combinatorial exploration of herbertsmithite-related compounds in search of other spin liquid candidates

Chapter 2

Methods

2.1 Density Functional Theory

Density functional theory (DFT) is a versatile tool for understanding the electronic properties of atoms, molecules, and crystalline solids. Like many powerful computational frameworks, density functional theory is successful because of its ability to simplify computationally intractable problems into simpler approximations that are feasible to compute. An excellent introduction to this field is provided in [34].

The goal of DFT is to calculate the energy of an atomic system and how this energy changes when the atoms move. Nuclei are much heavier than electrons, and thus the computational problem can be divided into two pieces: (1) solving for positions of the fixed nuclei and (2) finding the lowest energy state of the electrons. This separation of the system is known as the Born Oppenheimer Approximation, where for N fixed nuclei with positions $R_1, ...R_M$ the energy of the ground state can be expressed as an adiabatic potential surface $E(R_1...R_M)$.

Typically, to determine how the energy changes, one would solve the time independent Schrodinger equation:

$$\left[\frac{h^2}{2m}\sum_{i=1}^{N}\nabla_i^2+\sum_{i=1}^{N}V(r_i)+\sum_{i=1}^{N}\sum_{j<i}U(r_i,r_j)\right]\psi=E\psi \tag{2.1}$$

The terms in Eq.2.1 are, respectively, the kinetic energy of each electron, the interactions between nuclei and electrons, and the interactions between electrons. Solving the above equation for any significant number of particles would quickly become prohibitively costly to calculate. Fortunately, two mathematical theorems, proved by Kohn and Hohenberg in in 1964 [35], can greatly simplify the computational task at hand. First, the energy of the ground state calculated by the the Schrodinger equation is a unique functional of the electron density. Second, the true ground state of the system is given by the electron density which minimizes this functional.

Hohenburg-Kohn Theorems

1. The ground state energy from the Schrodinger equation is a unique functional of the electron density.

2. The electron density that minimizes the energy of the overall functional is the true ground state density corresponding to the full solution of the Shrodinger equation.

By implementing these theorems, we can use the electron density, a function of three spatial coordinates, instead of the full Schrodinger equation which is a function of $3N$ variables, where N is the number of particles. While a function takes as input the values of variables and returns a single number from those variables, a functional takes a function as input, and returns a single number from that function. The energy functional takes

the wave function as input, which is a function of the electron density $n(r)$, given by:

$$n(r) = 2\sum_i \psi_i^*(r)\psi(r) \tag{2.2}$$

The energy functional is written as:

$$E[\psi_i] = E_{known}[\psi_i] + E_{XC}[\psi_i] \tag{2.3}$$

The term E_{known} in the energy functional can be solved for exactly, and is written as:

$$E_{known}[\psi_i] = \frac{h^2}{m}\sum_i \int \psi_i^* \nabla^2 \psi_i d^3r + \int V(r)n(r)d^3r + \frac{e^2}{2}\int\int \frac{n(r)n(r')}{|r-r'|}d^3r d^3r' + E_{ion} \tag{2.4}$$

Where the terms above are respectively, the kinetic energy of the electrons, the attractive Coulomb repulsion between nuclei and electron, and the repulsive Coulomb interaction between electron pairs. However, some quantum mechanical effects are not included in E_{known} and must be approximated in the exchange-correlation term E_{XC}.

The exchange-correlation term accounts for interactions that cannot be captured by the mean-field approximation of the system's electron density. The exchange energy describes the asymmetry of the wavefunction upon the exchange of two electrons. The correlation term accounts for correlations in the motion of electrons which can be non-local. The true form of E_{XC} is not known, except in one case for a uniform electron gas where $n(r)$ is a constant. The uniform electron gas provides a starting point to approximate the true E_{XC} for real materials. Two of the main approximations are the local density approximation (LDA), and the generalized gradient approximation (GGA).

The minimization of the energy functional can be achieved by solving a set of single-particle equations, called the Kohn-Sham equations, which are similar to the full Schrodinger

equation shown above, but without the summation, since the Kohn-Sham equations are for single electron wavefunctions depending on only three spatial variables. The Kohn-Sham equations have the form:

$$\left[\frac{h^2}{2m}\nabla^2 + V(r) + V_H(r) + V_X C(r)\right]\psi_i(r) = \epsilon_i \psi_i(r) \tag{2.5}$$

Solutions to the Kohn-Sham equations can be found through an iterative, self-consistent work flow. First, an initial trial electron density is defined and the Kohn-Sham equations are solved. Then the electron density is calculated using the Kohn-Sham equations from the second step. The densities from the first and second steps are compared, and the process is iterated until they match within a certain tolerance.

Density functional theory (DFT) has been used in the present work in a variety of ways, to perform structural relaxations, to compare energies of different structures, to explore the effects of changing carrier concentration, and to studying the electronic and vibrational degrees of freedom of different materials. DFT remains one of the most robust and versatile tools in the field of computational materials science, which is demonstrated by the pivotal role DFT has played in each project discussed in this thesis.

2.2 Landau Theory

Landau theory is a phenomenological theory, meaning that the microscopic details of the system, such as pairing interactions in a superconductor or dipole interactions in a ferroelectric, are not considered. Landau theory is the theory of phase transitions based on the appearance or disappearance of some element of symmetry. While the presence or absence of a certain symmetry is discontinuous (there is no intermediate state) the change of other related quantities, such as the energy, may be continuous.

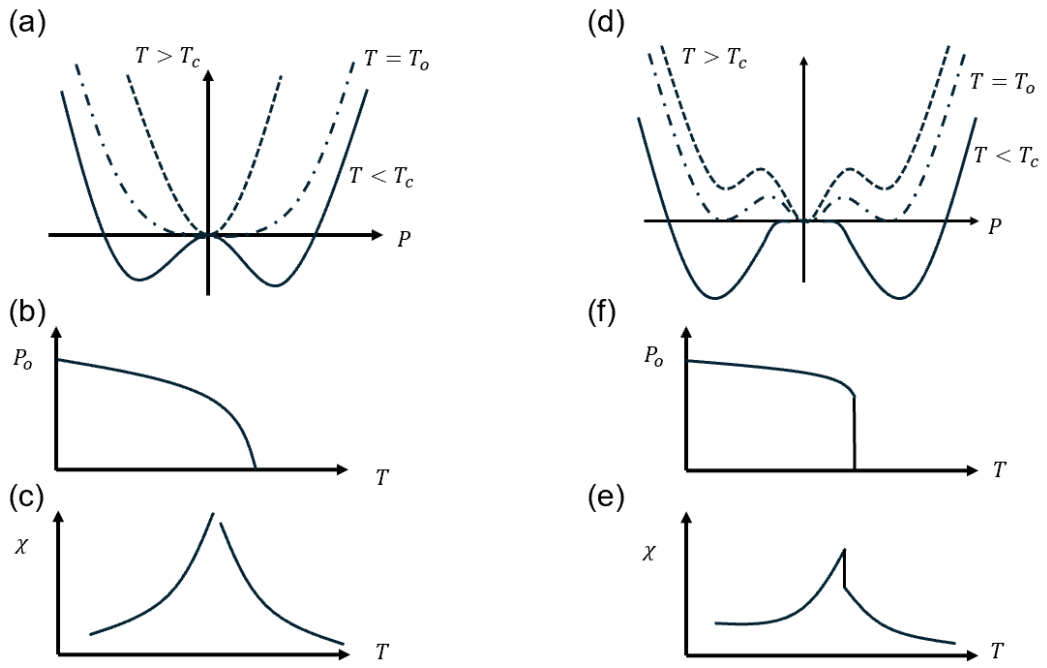

Figure 2.1: **Landau Free Energy** (a) Potential energy landscape of a second order phase transition (b) Schematic of order parameter versus temperature (second order phase transition) (c) Susceptibility versus temperature (second order phase transition) (d) Potential energy landscape for a first order phase transition (e) Temerature dependence of the order parameter (first order phase transition) (f) Susceptibility versus temperature (first order phase transition)

Landau introduced the concept of the order parameter: a measure of order before and after a phase transition. The order parameter is zero above some critical temperature and takes on a finite value below the critical temperature. The central component of Landau theory is the construction of the Landau free energy $\mathcal{F}$, which is a function of the order parameters relevant to the phase transitions of the system. According to Landau theory, the stable state of the system is the state for which the $\mathcal{F}$ is minimized with respect to the internal degrees of freedom given a set of external parameters.

A high-symmetry phase is assumed to exist in the phase diagram, typically at high temperatures. In this high symmetry phase the order parameters of the relevant modes

are zero. The free energy functional can be written as:

$$\mathcal{F} = \mathcal{F}_0 + \Delta\mathcal{F}(\eta^i) \tag{2.6}$$

In the vicinity of the phase transition, $\Delta\mathcal{F}(\eta^i)$ is assumed to be small, and $\mathcal{F}_0$ does not influence the phase transition. Since $\Delta\mathcal{F}(\eta^i)$ is small, one can perform a Taylor series expansion in powers of η^i. In the case of a one-dimensional real order parameter, the Taylor series expansion of the Landau free energy will resemble:

$$\Delta\mathcal{F}(\eta^i) = -\eta H + \frac{a}{2}\eta^2 + \frac{c}{3}\eta^3 + \frac{b}{4}\eta^4 + o(\eta^5) \tag{2.7}$$

Only terms allowed by symmetry will exist in the final polynomial expression. Linear terms are not included unless there is coupling to an external field. It is imperative that $\Delta\mathcal{F}$ is invariant by all symmetry elements of the high-symmetry group.

In this thesis, Landau theory is employed to model the structural phase transitions in strontium titanate. These simulations will be discussed in detail in Chapter 3.

2.3 Metropolis Monte Carlo

The Monte Carlo method was initially developed in the 1940s at Los Alamos National Laboratory as a means to evaluate intractable numerical problems such as multidimensional integrals. In the context of materials science, the Monte Carlo method is a powerful tool for providing thermodynamic information for a given system. It is based on the direct evaluation of the ensemble average, and therefore does not yield dynamical information, but can be extremely useful in calculating thermal averages of material properties. The descriptions provided in this section follow closely those outlined in [36].

The objective of the Monte Carlo method is to simulate trajectories that represent a

system at thermal equilibrium, where a trajectory is defined as a chronological sequence of configurations. A typical Monte Carlo simulation considers a system with constant temperature, volume, and number of particles. The thermal average of a quantity in the canonical ensemble of such a system is given by:

$$\langle P \rangle = \frac{\sum_\alpha e^{-E_\alpha/k_b T} P_\alpha}{\sum_\alpha e^{-E_\alpha/k_b T}} = \sum_\alpha P_\alpha \rho_\alpha \tag{2.8}$$

In the above expression P is a quantity representing some property of the system and the α subscript represents all possible configurations of the system. The probability of finding the system in a specific configuration is given by:

$$\rho_\alpha = \frac{e^{-E_\alpha/k_b T}}{\sum_\alpha e^{-E_\alpha/k_b T}} = \frac{e^{-E_\alpha/k_b T}}{Q} \tag{2.9}$$

where Q is the partition function:

$$Q = \sum_\alpha e^{-E_\alpha/k_b T} \tag{2.10}$$

The relative probability of the system being in one state α or another state β is:

$$\frac{\rho_\beta}{\rho_\alpha} = \frac{e^{-E_\beta/k_b T}}{Q} \frac{Q}{e^{-E_\alpha/k_B T}} = e^{-(E_\beta - E_\alpha)/k_b T} \tag{2.11}$$

The energy difference, $\Delta E_{\alpha,\beta} = E_\beta - E_\alpha$, completely determines the relative probability between the states α and β.

In principle, evaluating the true thermal average of a system would require a list of all possible configurations of the system. However, while many configurations will be possible, very few are probable. In 1953 Metropolis et al. [37] developed an algorithm that employs importance sampling; while we cannot know the true probability of the

system being in a certain configuration, if we consider a sufficiently large and sufficiently random sample of configurations, the probability we calculate from that sample will be representative of the true probability

Using the Metropolis algorithm we begin in a starting configuration and make a trial move to a new configuration. By considering the relative probabilities between the old and new configurations, we decide whether the new configuration should be added to our trajectory through the phase space. Let us begin in configuration i with energy E_i. We perform a trial move to configuration $i+1$ with energy E_{i+1}. We determine whether $i+1$ is added to our trajectory based on the ratio of probabilities between the two states $\rho_{i+1}/\rho_i = exp(-\Delta E_{i,i+1}/k_B T)$. Within the Metropolis algorithm, the trial move is accepted or rejected based on the following criteria:

$$\begin{gathered} \Delta E_{i,i+1} \leq 0 \quad \text{accept since probability is 1} \\ \text{or} \\ \Delta E_{i,i+1} > 0 \quad \text{accept move with probability } e^{-\Delta E_{i,i+1}/(k_B T)} \end{gathered} \tag{2.12}$$

By performing many trial moves, a list of n configurations with energies E_n can be generated with probability representative of the true probability. Therefore, the average of a thermodynamic quantity P can be calculated as for a total number of m trial moves:

$$\langle P \rangle = \frac{1}{n} \sum_{\alpha=1}^{m} P_\alpha \tag{2.13}$$

In this thesis, the Monte Carlo Metropolis algorithm is used in combination with a free energy model developed using the prescription of Landau to simulate the structural phase transitions in strontium titanate. The details of these simulations will be discussed in Chapter 3.

2.4 Lagrangian Mechanics

In addition to Newtonian and Hamiltonian mechanics, Lagrangian mechanics provides an elegant framework for obtaining the equations of motion for systems of particles. The key principle underlying this formalism is the principle of least action.

Principle of Least Action

The principle of least action states that the path of a particle between two points in configuration space is the path that minimizes the action integral.

$$S = \int_{t_1}^{t_2} L(y, \dot{y}, t) dt \tag{2.14}$$

In the formalism of Lagrangian mechanics, the action is the integral of the Lagrangian over time, where the Lagrangian function (L) is defined as the kinetic energy (T) minus the potential energy (U) of the system.

$$L = T - U \tag{2.15}$$

This Lagrangian function characterizes the state of a physical system. The Euler-Lagrange equation, formulated from the calculus of variations, is the function that minimizes the action integral.

$$\frac{d}{dt}\left(\frac{\partial L}{\partial \ddot{x}}\right) - \frac{\partial L}{\partial x} = 0 \tag{2.16}$$

The trajectory of a system will evolve according to Eq.2.16. While Newtonian mechanics sums over all forces in the system, Lagrangian mechanics offers a different formulation based on energies instead of forces. Instead of considering the unwieldy vector equations required by Newtonian mechanics, the Euler-Langrange equation simplifies the computational problem by considering energies in a generalized coordinate system. Lagrangian

mechanics can also simplify the implementation of constraints and the consideration of various symmetries.

In Chapter 3, Lagrangian mechanics is used to calculate the low energy phonon bands in the ground state of strontium titanate. Instead of considering the motion of all atoms in all three Cartesian directions, we consider the value of the overall polar and antiferrodistortive distortions within a unit cell and solve the Euler Lagrange equation. Using Lagrangian mechanics reduces the dimensionality of the problem from $15N$, where N is the number of atoms in the unit cell, to only four degrees of freedom.

2.5 Langevin Dynamics

Brownian motion, or the random motion of small particles, was described formally in 1827 by Thomas Brown. In 1908, Paul Langevin demonstrated that Brownian motion could be described by an equation of motion called the Langevin equation, a stochastic differential equation that describes the time evolution of a subset of degrees of freedom. The following discussion of Langevin dynamics follows closely with that provided in [36].

$$m\frac{d^2\mathbf{r}}{dt^2} = \mathbf{F} - \gamma\frac{d\mathbf{r}}{dt} + \mathcal{F}_{rand}(t) \tag{2.17}$$

In the above equation, $\mathbf{r}$ is the position of the particle, γ is a drag or friction coefficient, m is the mass of the particle, and $\mathcal{F}_{rand}(t) = \sqrt{2\gamma k_B T}\mathcal{R}(t)$ is a random force term. This stochastic noise term, $\mathcal{F}_{rand}(t)$, typically describes the collision of a particles with molecules of a surrounding fluid. The random variable $\mathcal{R}(t)$ is uncorrelated in time, meaning that the random force at a given time t is unaffected by the force at any other time. The form of this force is given by the fluctuation-dissipation theorem. The random force must be drawn from a normal Gaussian distribution according to the central limit

theorem.

The Langevin equation is a powerful tool for including temperature effects in dissapative systems. Modeling of complex systems with many particles can be simplified by considering only a subset of the total degrees of freedom. For example, solvent molecules in a solute can be modeled by considering the drag on the solute molecules and random forces due to the thermal motion of the solvent molecules, ignoring the detailed motion of each solvent particle. The faster, microscopic variables are encompassed in the stochastic portion of the Langevin equation, while the macroscopic degrees of freedom that evolve more slowly are simulated explicitly.

The presence of a dissipative force term, $(-\gamma\frac{d\mathbf{r}}{dt})$, has a dramatic effect on the dynamics of the system. An object dropped in a vacuum, subjected only to gravity, will accelerate until it hits the ground, while an object falling through a viscous fluid will quickly reach a constant velocity. Therefore, a large damping coefficient can shorten the time required to reach equilibrium.

In this thesis, Langevin dynamics is used to calculate the temperature-dependent phonon spectral function of strontium titanate. The potential force term is derived from a free energy model developed using Landau theory. Temperature effects, including through the stochastic force term in the Langevin equation, allow us to model the frequency of the polar phonon modes with respect to temperature in a large, disordered supercell.

Chapter 3

Polar Order in Strontium Titanate

3.1 Lattice Dynamics

At high temperatures, bulk $SrTiO_3$ has a cubic structure with the space group $Pm\bar{3}m$. The unit cell contains five atoms and has a total of $3 \times 5 = 15$ normal vibrational modes comprised of 12 optical modes, and 3 acoustic modes. At the Γ point, there are four triply degenerate T_{1u} modes. Three of these four modes are associated with the polar eigenvectors shown in Fig.3.1(a-c). The degeneracy of polar triplets is broken by energy splitting of the longitudinal and transverse optical modes [6, 38]. Frequencies of the polar modes are given in Tab.3.1.

The polar displacements at the Γ point are associated with cations moving in opposition to anions, which produces an electric dipole moment. Due to the coupling between lattice distortions and the electric polarization, the polar phonon modes are subject to long-range Coulomb interactions, and as a result, each triplet of polar modes splits into one longitudinal optical mode with frequency $\omega_{L,j}$ and a doubly degenerate transverse optical phonon mode with frequency $\omega_{T,j}$. For the longitudinal mode, ions displace parallel to the direction of wave propagation and parallel to the electric field. Therefore, it takes

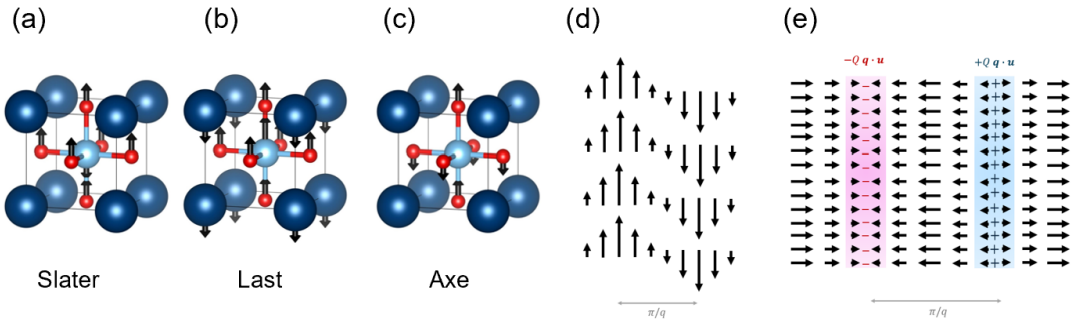

Figure 3.1: **Eigenvectors of Polar Modes** (a) Slater mode (b) Last mode (c) Axe mode (d) Transverse optical modes where displacements occur perpendicular to the direction of propagation. (e) Longitudinal optical mode where displacements occur parallel to the direction of propagation. Figure adapted from [39, 38].

more energy to excite these modes, and the LO mode has higher energy. Schematics of LO and TO phonon modes are depicted in Fig.3.1(d,e). The large LO/TO splittings in $SrTiO_3$ indicate the strong polar nature of this material.

Table 3.1: Frequencies of Polar Phonon Modes in $SrTiO_3$. Adapted from [39]

TO Mode	Frequency [meV]	LO Mode	Frequency [meV]
TO1	(1,11.3)	LO1	21.3
TO2	21.7	LO2	58.7
TO3	67.4	LO3	98.1

The proximity to a ferroelectric-like transition in $SrTiO_3$ is characterized by the divergence of the dielectric function upon temperature lowering. The dielectric function can be approximated by a generalized Lyddanne-Saches-Teller relation:

$$\epsilon_p(\omega, q) = \epsilon_\infty \prod_{j=1}^{3} \frac{\omega_{L,j}^2 - \omega^2}{\omega_{T,j}^2 - \omega^2} \tag{3.1}$$

The frequency of the TO1 mode (ω_{TO1}) is sensitive to factors like temperature, doping, and electric fields, which can be summarized in the phenomenological equation:

$$\omega_{T,1}^2(q, T, E, n) = \omega_0^2 + (c_T q)^2 + (\gamma_T T)^2 + (\gamma_E E)^2 + \gamma_n n \tag{3.2}$$

Which can be substituted into Eq.3.2. As temperature decreases, the static dielectric function ϵ_0 of $SrTiO_3$ increases from 300 to 2×10^4 following Curie-Weiss behavior $\epsilon_0(T) \propto (T - T_o)^{-1}$. This behavior signals a ferroelectric instability around $T_0 \approx 36K$. However, the increase in ϵ_0 saturates at this temperature instead of diverging, indicating a transition from a classical to a quantum paraelectric, where an ordered polar state is suppressed by quantum fluctuations. Methods for stabilizing polar order will be discussed in the next section. At 105 K, a triply degenerate T_{2u} mode softens at the R-point, leading to zone folding [40]. Below this transition, the soft TO1 mode has the irrep E_u. Within the polar phase, the irrep of polar mode is A_{1g}.

3.2 Stabilizing Polar Order

A polar transition can be induced through uniform epitaxial strain [41, 42, 43], plastic deformation [44], or other methods including chemical substitution and optical excitation [45, 46, 47, 48, 49, 50, 51]. As discussed in Chapter 1, superconductivity is enhanced in proximity to the quantum critical point, as well as within the polar phase. A rigorous understanding of the polar order is therefore essential in elucidating the superconducting pairing mechanism. The characteristics of the polar phase, including the space group symmetry, the direction of the polar eigenvector, and the critical temperature of the transition will depend on the method used to induce the polar transition. Isotope substitution with ^{18}O can facilitate the condensation of the TO1 mode at 23 K, as the heavier oxygen isotopes soften the phonon frequency. This leads to an orthorhombic low-symmetry space group with a polarization vector along [110] and symmetry-equivalent directions, with a quantum critical point at 35 % ^{18}O substitution [45, 52, 53].

Exchange of Sr with isovalent Ca ions in $Sr_{1-x}Ca_xTiO_3$ leads to local electric dipoles as the smaller Ca ions take off-center positions. Above a threshold concentration of

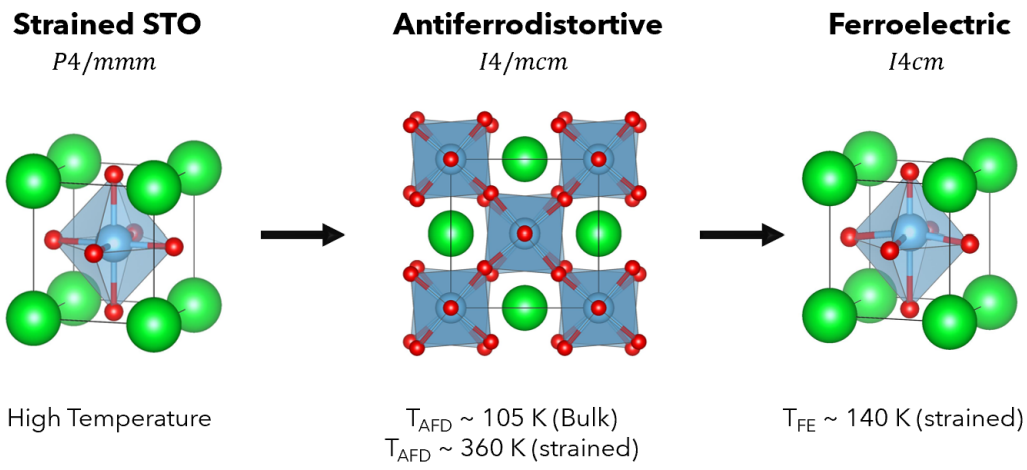

Figure 3.2: **Structural Transitions** (a) High-temperature strained, centrosymmetric structure (b) Transition to the tetragonal phase with antiferrodistortive rotations occurs at $\approx$ 360 K in the strained system, compared to to 105 K in the bulk (c) The polar transition to the low-temperature noncentrosymmetric structure occurs around 140 K in the strained system in the absence of dopants.

$x = 0.002$, long-range polar order is stabilized below a Curie temperature of around 10 K, with a maximum Curie temperature of 27 K at $x = 0.009$ [46].

Room temperature ferroelectricity can be achieved through tensile strain of up to 2%. In systems under high levels of tensile strain with a polar vector along the [100]/[00] directions within the orthorhombic $mm2$ space group. The formation of polar nanodomains at high temperatures are observed through experimental imaging techniques and the results of molecular dynamics simulations [43]. In this work, we will focus on a system under 1% biaxial compressive strain that transitions from the high-temperature P4/mmm (Fig.3.2(a)) structure to the tetragonal I4/mcm structure (Fig.3.2(b)) at 360 K, and to the polar I4cm structure at 140 K (Fig.3.2(c)). The polarization vector is along the [001] axis. In following sections we will define the different classes of polar transitions and provide an overview of previous work characterizing the polar phase before discussing our results.

3.3 Classifications of Polar Phase Transitions

Polar phase transitions are generally categorized into one of two main classes: displacive or order-disorder. The two types of ferroelectric phase transitions can be described by the same Hamiltonian, with different limiting conditions on its parameters.

$$\mathcal{H} = \frac{1}{2}\alpha\sum_{\vec{r}} u(\vec{r})^2 + \frac{1}{4}\beta u(\vec{r})^4 + \frac{1}{2}c\sum_{\vec{r},\vec{r^*}}(u(\vec{r}) - u(\vec{r^*}))^2 \tag{3.3}$$

Here, $\alpha < 0$ and $\beta > 0$. The first term describes the motion of the A (cation) and B (anion) ions against one another, i.e. the ferroelectric distortion within the unit cells. The second term describes the interaction of intersite A atoms, i.e. the coupling of dipoles in neighboring cells. The coefficient c can be thought of as the "stiffness" of the force between neighboring sites. The potential acting a single A atom is:

$$\mathcal{U} = \frac{1}{2}(\alpha + 6c)u(\vec{r_o})^2 + \frac{1}{4}\beta u(\vec{r_o})^4 \tag{3.4}$$

In a displacive transition $|\alpha| << c$, indicating that the strength of the interactions between neighboring dipoles is large compared to the potential well. Individual A atoms move in a potential well with a single minimum, the value of which shifts approaching the transition temperature, T_c. The displacive Hamiltonian is expressed in terms of a local normal coordinate which describes the magnitude of the uniform ferroelectric distortion at a given time. In the order-disorder limit $|\alpha| >> c$, the potential barrier is high relative to interactions, so each atom occupies one of the two minima, even at high temperatures. The order-disorder Hamiltonian can be reduced to the Ising model [54]. Since the relative importance of these contributions depends on the ratio of continuous parameters, there exist some intermediate values of these coefficients where the distinction between the two types of transitions is no longer well-defined [55]. A polar transition with mixed

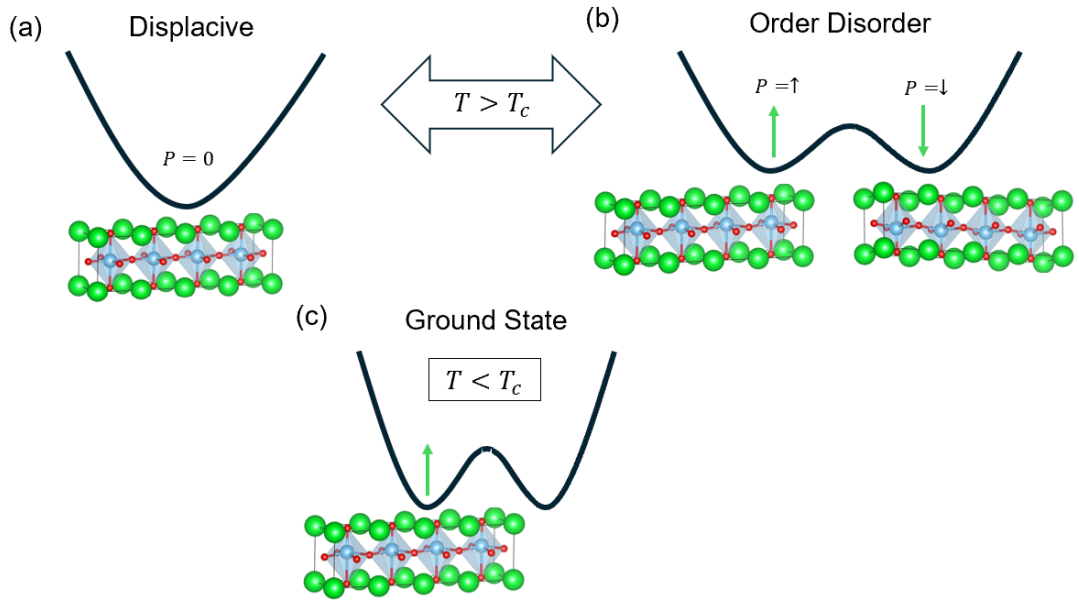

Figure 3.3: **Two Main Classes of Polar Transitions** (a) In a displacive transition above T_c, all unit cells are centrosymmetric. (b) For an order-disorder transition above T_c, unit cells are randomly polarized up or down. Polar distortions exist but there is no global polar order. (c) In the ground state below T_c, all dipole moments align.

character is observed in $SrTiO_3$. Scattering experiments show a soft phonon mode whose frequency decreases with temperature (displacive character), while imaging techniques show polar nanodomains (order-disorder character). The data supporting each type of phase transition in $SrTiO_3$ will now be presented, followed by a discussion of how they may coexist.

3.3.1 Displacive Characteristics in STO

Scattering experiments have measured the temperature dependence of the lowest energy TO phonon mode. Only one study has provided data showing *complete* softening of the mode ($\omega \rightarrow 0$ at T_c) in ferroelectric samples [56], while others show incomplete softening [57] [58] [46] [53], where the frequency plateaus at a finite value approaching T_c. A summary of this evidence is given in Tab.3.2.

Table 3.2: Soft Mode Data

Material	Technique	References
Bulk STO	Neutron	[59] [6] [60] [61]
	Infrared	[6] [62]
	Raman	[63][64] [65]
	Computation	[66] [67]
Thin Films	Raman	[68] [69]
	Infrared	[70]
	Dielectric Permittivity	[70]
	THz Time Domain	[71]
Doped STO	Raman	[72]
	Neutron	[72]
	Computation	[73] [74]
$SrTi^{18}O_x^{16}O_{1-x}$	Raman	[56] [57] [53]
$Sr_{1-x}Ca_xTiO_{3-\delta}$	Raman	[46]
	Computation	[75]
Strained STO	Raman	[58]
	Infrared	[76]
	Dielectric Permittivity	[58] [77] [78]
	Neutron	[79]
	Computation	[80] [81] [82] [75]

In bulk $SrTiO_3$, the frequency of the TO1 mode decreases following Curie-Weiss type behavior down to low temperature where it saturates around 1 meV [60]. It is assumed that this behavior is due to quantum fluctuations which prevents complete softening of the mode, however, clusters of polar order could also result in the same effect.

In thin films, the soft mode hardens significantly compared to bulk single crystals. This discrepancy is likely due to formation of local polar regions with reduced grain size in thinner films [70] [68] [71] [69].

Below the AFD transition, the TO1 mode has the irreducible representation (irrep) E_u, which is infrared active but can be observed by Raman spectroscopy due to local symmetry breaking. The intensity of the polar mode can be enhanced by an applied electric field [69]. Below the ferroelectric transition temperature, the irrep of the polar

mode is A_1 and the mode is Raman active [56].

The effect of free carriers on the soft mode is explored in [72], where the temperature dependence of the TO1 mode was measured using Raman spectroscopy for various levels of doping via oxygen reduction. Increasing free carriers leads to the hardening of the TO1 mode due to the influence of free electrons, local changes in potential, and changes in potential due to long-range interactions. A-site La-doped and B-site Nb-doped STO also display soft mode hardening as measured by terahertz time-domain spectroscopic ellipsometry [83]. Hydrostatic pressure [77] [78] also has the effect of hardening the soft mode and suppressing ferroelectricity.

Mode softening, on the other hand, can be achieved by inducing ferroelectricity. In a classic displacive ferroelectric the TO1 mode would be expected to soften completely ($\omega \to 0$ at T_c). As discussed above, only one study observed complete softening while others saw softening. Whether the frequency of the TO1 mode decreases completely to zero is largely irrelevant in terms of the superconducting pairing mechanisms that involve the soft mode. The same qualitative effects would be seen for complete versus incomplete softening. Theories for pairing mechanisms involving the soft phonon mode will be discussed in detail in Chapter 4.

3.3.2 Order-Disorder Characteristics in STO

Despite the broad assumption that $SrTiO_3$ is a classic displacive ferroelectric, there are also experimental and computational studies showing the existence of polar nanodomains in $SrTiO_3$ films at high temperatures. A summary of this evidence is given in Tab.3.3. Early dielectric permittivity [84] [85] [86] and birefringence experiments [87] [88] confirmed the relaxor-type behavior of $Sr_{1-x}Ca_xTiO_{3-\delta}$ (STO:Ca), where off-center calcium ions lead to domain formation.

Quadrupole NMR experiments also showed off-center titanium atoms at high temperatures in STO18 [89] [90]. Nanodomains have been observed using piezoelectric force microscopy in $SrTiO_3$ samples under 2% tensile strain, and accompanying molecular dynamics simulations showed a double-peaked histogram of the polar vector at high temperatures, indicative of oppositely ordered domains [43].

Table 3.3: Nanodomain Data

Material	Technique	References
Bulk STO	Computation	[91]
STO18	Quadrupole NMR	[89] [90]
$Sr_{1-x}Ca_xTiO_{3-\delta}$	Dielectric Permittivity	[84] [85] [86]
	Birefringence	[87] [88]
	Raman	[88]
Strained STO	PFM	[92] [43]
	HAADF-STEM	[93] [94] [95]
	Computation	[43] [96] [74]

More recently, nandomains have been observed by HAADF-STEM imaging in both strained and unstrained films at room temperature. The possible relationship between polar clusters and superconductivity will be discussed in Chapter 4.

It should be noted that in the soft mode experiments for STO18 discussed previously, the polar E_u mode in the Raman spectra was only visible due to local symmetry breaking, implying the existence of precursor order [69] [56]. It was also suggested that the soft mode hardening in thin films compared to bulk $SrTiO_3$ was due to reduced domain size [71] [68] [70].

The technical challenges in measuring the size of the nanodomains down to low temperatures make it difficult to experimentally study domain dynamics. The statistical mechanical methods implemented in this work allow for the simulation of domains across the phase transition at various doping levels.

3.3.3 A More Complex Picture

Considerable experimental evidence exists both for a ferroelectric soft mode and for the presence of polar nanodomains. The important question remains as to which dynamics are key in the superconducting pairing mechanism. We must also examine how phonons and polar domains coexist, as phonons are technically defined in the context of a perfect crystal. Displacive transitions may take on order-disorder character in the critical region as the soft mode begins to condense inhomogeneously, and ordered clusters may form before percolating into the uniform low-energy state. Likewise, the growth and ordering of domains in an order-disorder type transition may involve fluctuations of phonon-like excitations with finite lifetimes. Simulations of both the phonon spectrum and polar order using the same model parameters will be useful in gaining a more holistic understanding of the complex dynamics of mixed character phase transitions.

3.4 Characterizing Polar Order in Strontium Titanate

[1]To investigate the nature of the polar order in strontium titanate, we develop a simplified free energy model that only includes the degrees of freedom necessary to capture the relevant physics in a biaxially compressively strained system. Our model can calculate the energies of large, disordered systems with near DFT-level accuracy. We simulate the ferroelectric and antiferrodistortive phase transitions using the Monte Carlo method and discuss the coupling between various order parameters. Finally, we assess the character of the polar transition, which we find to be neither strictly displacive nor order-disorder.

[1]The contents of this section are adpated from [97]: "Modeling polar order in compressively strained strontium titanate," Alex Hallett, and John W. Harter, *Physical Review B*, 106, (2022): 214107.

3.4.1 Computational Procedure

Before simulating large-scale systems, it is necessary to first find the ground state strained structure at zero temperature. Through a series of structural relaxations, the ground-state structure of $SrTiO_3$ was calculated by DFT as implemented in the Vienna *ab intio* simulation package (VASP) [98, 99, 100]. We used the supplied projector-augmented wave (PAW) potentials [101] within the generalized gradient approximation (GGA) and Perdew-Burke-Ernzerhof (PBE) scheme [102]. Electronic wave functions were expanded in a plane-wave basis set with a kinetic energy cutoff of 800 eV, and the reciprocal space was sampled using an $8 \times 8 \times 8$ Γ-centered k-point mesh for a single 5-atom unit cell. The k-point density was appropriately scaled for any supercell calculations.

After fully relaxing the cubic structure, the a and b lattice parameters were decreased to 99% of their equilibrium values to replicate the effect of compressive epitaxial strain. After obtaining the equilibrium c-axis lattice parameter in the strained centrosymmetric state, iterative calculations were performed which varied the rotation, polarization, and additional elongation of the c-axis until the energy was minimized. We confirmed the stability of the ground state structure by calculating the phonon dispersion using the finite displacement method within the PHONOPY code [103] and verifying the absence of imaginary frequencies. The phonon dispersions of the strained, centrosymmetric reference structure and the polar structure with in-plane polarization components included are shown in Fig. 3.5. We found it was necessary to include slight in-plane polarization displacements to eliminate small imaginary frequencies at the Γ-point. However, the in-plane components of the polarization were neglected in subsequent calculations as they become insignificant at any finite temperature due to the shallowness of their potential well. After calculating the phonon dispersion in Fig. 3.5(b), the structure was relaxed further, without in-plane polarization components since they become insignificant at fi-

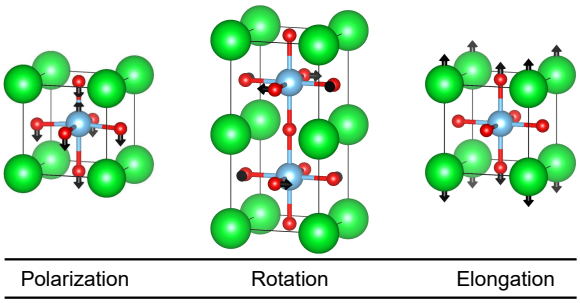

Figure 3.4: **Structural distortions in $SrTiO_3$.** Three main order parameters are considered in our model: the polarization along the c-axis, in-plane antiphase octahedral rotations, and the elongation of the c-axis.

Table 3.4: Ground state distortions.

Ion Type & Direction	Displacement (Å)
Titanium ($\hat{z}$)	0.035
In-Plane Oxygen ($\hat{z}$)	-0.100
Out-of-Plane Oxygen ($\hat{z}$)	-0.112
Rotation ($\hat{x}/\hat{y}$)	0.172
Elongation ($\hat{z}$)	0.051

nite temperature compared to the out-of-plane polarization. The final ground state was lower in energy than the structure shown in this dispersion. Due to the arduous process of finding the correct in-plane polarization components to eliminate tiny imaginary frequencies at the Γ-point, an optimized dispersion was not calculated for the fully relaxed ground-state structure. The non-analytical correction (NAC) term was used in PHONOPY to account for energy splitting of the transverse-optical and longitudinal-optical modes.

The progression of the structural parameters at different stages of relaxation is summarized in Tab.3.5. The increase in c-axis elongation is presented in Tab.3.6, and the ratio of the in-and out-of-plane oxygen displacement to the titanium displacement is shown in 3.7. Due to the changes in ratio of titanium to oxygen displacements, the movements of the ions comprising the overall polar eigenvector were treated as separate degrees of freedom.

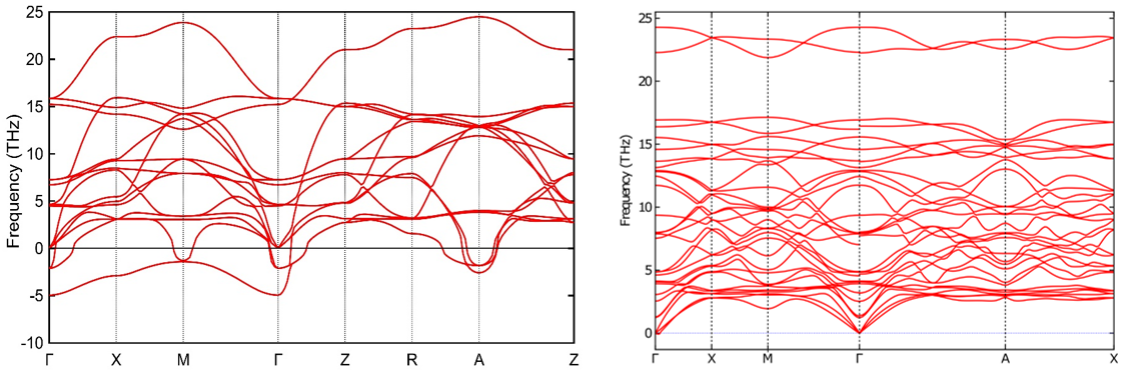

Figure 3.5: **Phonon Dispersion** (a)Phonon dispersion for the strained, centrosymmetric reference state calculated using DFT and Phonopy software using the finite displacement method. (b) Phonon dispersion of structure close to the ground state. This structure includes in-plane polarization displacements to eliminate small imaginary frequencies at the Γ-point

Table 3.5: Ionic displacements for the rotation and polarization displacements.

Structure	Ti (Å)	O_{in} (Å)	O_{out} (Å)	R (Å/°)	ΔE (meV)
Cubic	–	–	–	–	–
Strained	–	–	–	–	–
Polarized	0.0169	-0.0988	-0.0972	–	-8.0237
Polarized/Rotated	0.0303	-0.0675	-0.0726	0.1712/5.0181	-12.5920
Pol./Rot./Elongated	0.0352	-0.1001	-0.1119	0.1722/5.0484	-17.7073

The order parameters in subsequent discussions are defined by the displacements of the ions in the ground state structure relative to the strained, centrosymmetric reference state. Schematics of these orders parameters are shown in Fig. 3.4, and their numerical values in the ground state are given in Table 3.4. With this definition, the individual order parameter amplitudes vanish in the reference state and are equal to exactly one in the ground state, which corresponds to a ground state polarization of 0.294 C/m^2.

The net polarization order parameter is calculated as the component of the titanium and oxygen ion displacement vector along the direction of the ground state displacement ($\hat{z}$) comprised of the three components: titanium (Ti), axial in-plane oxygens ($O_{in,1}, O_{in,2}$), and apical out-of-plane oxygen (O_{out}) displacements. The squared frac-

Table 3.6: Change in c-axis Δc from the reference state.

Structure	c-axis (Å)	Increase from cubic (%)	c/a ratio	Δc (Å)
Cubic	3.9389	–	–	–
Strained	3.9647	0.6530	1.0167	0
Polarized	3.9647	0.6530	1.0167	0
Polarized/Rotated	3.9647	0.6530	1.0167	0
Pol./Rot./Elongated	4.0154	1.9403	1.0297	0.0507

Table 3.7: Ratios of oxygen displacements to titanium displacement.

Structure	O_{in}/Ti	O_{out}/Ti	O_{in}/O_{out}
Cubic	–	–	–
Strained	–	–	–
Polarized	-5.8963	-5.8027	1.0161
Polarized/Rotated	-2.2281	-2.3950	0.9303
Pol./Rot./Elongated	-2.8443	-3.1780	0.895

tional ground state displacements are multiplied by the amplitude of each degree of freedom and then normalized by dividing by the sum of the squared displacements. Recall that the amplitude of the order parameter is X_{disp}/X_{GSD}, and thus the ground state displacements must be squared in the numerator. The resulting expressions ensure that the order parameter is equal to one in the ground state, and equal to zero in the absence of polar distortions.

$$P = \frac{Ti^2_{GSD}(Ti_{OP}) + O^2_{in,GSD}(O_{in,1}) + O^2_{in,GSD}(O_{in,2}) + O^2_{out,GSD}(O_{out})}{Ti^2_{GSD} + 2(O^2_{in,GSD}) + O^2_{out}} \tag{3.5}$$

The rotation order parameter is defined as the absolute value of the displacement of the axial oxygen ions along $(\hat{x}, \hat{y})$, accounting for averaging between neighboring unit cells. The ground-state structure has an octahedral rotation angle of 5.04°. The values R_x within Eq.3.6 correspond to the amplitude of the order parameter (R_{disp}/R_{GSD}) in different unit cells.

The full rotation order parameter is given by:

$$R_n = \frac{1}{2}\left(\frac{R_{1,n} - R_{1,n+\delta=100}}{2} + \frac{R_{2,n} - R_{2,n+\delta=010}}{2}\right) \tag{3.6}$$

The elongation degree of freedom describes the lengthening of the c-axis lattice parameter from its reference state value of 3.965 Å (a 0.65% increase from the cubic structure) to its ground state value of 4.015 Å (a 1.9% increase from the cubic structure). The in-plane lattice parameters remain constant at 3.900 Å for all calculations.

3.4.2 Free Energy Model

DFT is limited due to its inability to account for thermal effects and the prohibitive computational cost of large, disordered systems. To simulate the thermal phase transitions in $SrTiO_3$, we construct a simple model that can efficiently incorporate both temperature and disorder. Following the prescription of Landau, we approximate the free energy of the system by a Taylor series expansion about the relevant order parameters, which yields a linear sum of invariant polynomials. We consider five total degrees of freedom in formulating the free energy expression: the three components of the polarization (titanium and in- and out-of-plane oxygen ions), the octahedral rotations, and the additional elongation of the c-axis in the ground state relative to the reference state. We used the ISOTROPY software suite [104, 105] to calculate invariant polynomials and find all symmetry-allowed free energy terms up to fourth-order in rotation and polarization and included coupling to the elongation up to linear order. Coupling of order parameters between neighboring sites (26 neighbors per site) was also included. The final expression for the free energy consisted of a polynomial containing 109 distinct terms.

In the harmonic spring model of a lattice with a quadratic interatomic potential, the

total potential energy of the lattice is given by:

$$V = \sum_{i',n'} K_{\alpha,\beta} \phi^2_{i',n'} \tag{3.7}$$

Where $K_{\alpha,\beta}$ is a $3N \times 3N$ matrix of interatomic force constants where N is the total number of ions, the indices (α, β) correspond to the cartesian directions (x, y, z), and $\phi_{i',n'}$ is the ionic displacement of ion i in unit cell n. For a large, disordered system, the matrix $K_{\alpha,\beta}$ is extremely large. In our model, we greatly reduce the phase space by defining ϕ_n as the amplitude of an order parameter (as defined in Eq.3.5 and Eq.3.6) in a given unit cell . The potential energy including the coupling to nearest neighbors is given by:

$$V = \sum_{n,\delta} a_\delta \phi_n \phi_{n+\delta} \tag{3.8}$$

Where n represents a sum over all unit cells, δ indicates the high symmetry direction of the nearest neighbor, and a_δ is the force constant along δ and all equivalent directions. Coupling to the 26 nearest neighbors in the 6 high-symmetry directions was considered. The fully expanded form of Eq.3.8 is:

$$\begin{aligned} V = a_{000} \sum_n \phi_n^2 + a_{100} \sum_{n,\delta} \phi_n \phi_{n+\delta} + a_{001} \sum_{n,\delta} \phi_n \phi_{n+\delta} ... \\ ... + a_{101} \sum_{n,\delta} \phi_n \phi_{n+\delta} + a_{110} \sum_{n,\delta} \phi_n \phi_{n+\delta} + a_{111} \sum_{n,\delta} \phi_n \phi_{n+\delta} \end{aligned} \tag{3.9}$$

For brevity, a shorthand for Eq.3.7 can be used:

$$V = \sum_{n,\delta} a_\delta \phi_n \phi_{n+\delta} \rightarrow a_{x-(x+5)} \phi^2 \tag{3.10}$$

The coefficients a_x are numbered from $x = 0 - 109$ to reach the total terms in the free

Table 3.8: Types of calculations and the number of calculations performed.

Type	Count
Random	1863
Uniform	1265
Specific Distortions	514
$4 \times 4 \times 4$ Supercerll	131
Total	3773
Test	100

energy polynomial. A full list of the polynomial terms in the model is given in Appendix A. Note that even though the terms with higher than quadratic order do not take nearest neighbor coupling into account, the averaging between oxygens is still accounted for, as shown here:

$$R_n^4 = \frac{1}{2}\left[\left(\frac{R_{1,n} - R_{1,n+\delta=100}}{2}\right)^4 + \left(\frac{R_{2,n} - R_{2,n+\delta=100}}{2}\right)^4\right] \tag{3.11}$$

To find the coefficients in the free energy expression, we used DFT to calculate the energies of $2 \times 2 \times 2$ supercell configurations, with random values chosen for every degree of freedom in each unit cell. In addition to these random calculations, we also included a set of specific uniform distortions. Larger $4 \times 4 \times 4$ supercells were also incorporated to determine if the exclusion of longer-range interactions affected the accuracy of the model. Specific configurations that lead to divergences in the model energy were also included to train the model to accurately calculate their energies and eliminate divergences to negative energies at finite temperature. A total of 3,773 configurations were considered. To further verify the accuracy and generality of our model, we also tested a set of 100 random $2 \times 2 \times 2$ configurations that were not used to calculate the model parameters. The error in the calculated energies for these test structures was comparable to that of the training data set. The different types of calculations are summarized in Tab.3.8. We solved for the values of the coefficients by minimizing the error between the model

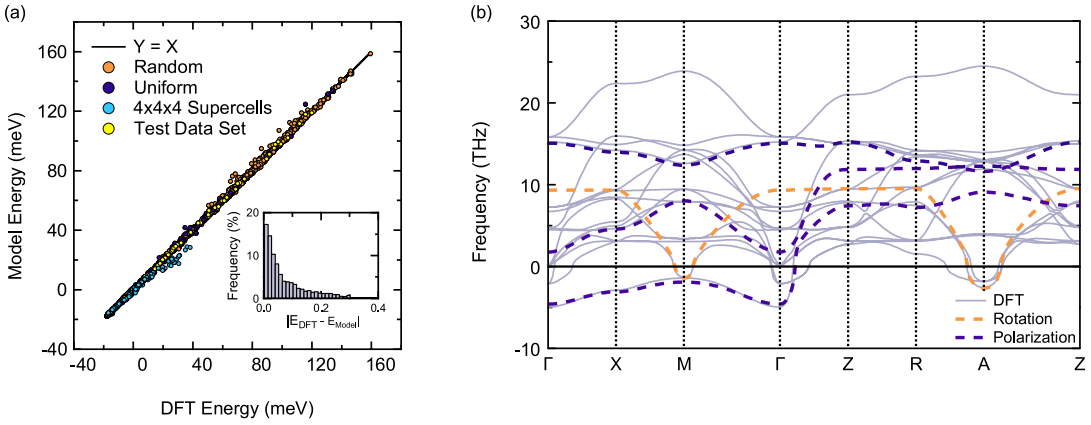

Figure 3.6: **Verification of the free energy model.** (a) A plot of the energies of 3,873 configurations calculated by our model versus the DFT-calculated energies. The model energies are in excellent agreement with DFT, with a root-mean-square error of 0.21 meV/atom. The inset shows the error distribution as the frequency of the error versus the error itself, which is defined as the discrepancy per atom between the DFT and model energies. (b) The 4 low-energy phonon bands (3 polarization, 1 rotation) calculated using our phonon dispersion expression are overlaid on the dispersion calculated using PHONOPY for the strained, centrosymmetric reference structure, showing that the simple model is able to capture the relevant instabilities with near DFT-level accuracy.

and DFT energies using the general formulat for least-squares linear regression given by:

$$M = (AA^T)^{-1}A^T E \tag{3.12}$$

Here M is the 109×1 vector of the model parameters, A is a 3773×109 matrix where each row represents a different configuration calculated by DFT and each column represents a term in the polynomial. The vector E is the 3773×1 vector of DFT energies. The order parameters were randomly or uniformly varied in different ways to ensure the physically relevant distortions were captured by the model and that there was an even distribution of configurations over a large range of energies. In order to eliminate divergences to large negative energies for physically irrelevant structures, Eq.3.12 was modified to weight certain configurations corresponding to specific instabilities more heavily, and impose certain constraints on the oxygen degrees of freedom.

The full expression to solve for the model coefficients, including the constraints and weighting matrix is:

$$M = \text{inv}[A^t W A] A^t W E - \text{inv}[A^t W A] Q * \text{inv}[Q^t \text{inv}[A^t W A] Q] * (Q^t \text{inv}[A^t W A] A^t W E - C) \tag{3.13}$$

The weighting matrix W is a 3773×3773 square diagonal matrix whose elements correspond to the weighting value of a particular configuration. The matrices Q and C place constraints on the oxygen ions. As previously discussed, oxygen ions are shared between neighboring cells, so the amplitudes of the degrees of freedom between these unit cells must be averaged. The model must calculate the same energy for a configuration in which the oxygen components of the polarization order parameters have high, out-of-phase amplitudes (or the rotation order parameter has high in-phase amplitudes) as it does for configurations where all amplitudes are zero. We impose a set of 32 constraints where the ion motion must equal zero at certain wavevectors. The matrix Q in Eq.3.13 has dimensions of 109×32, corresponding to the number of terms in the polynomial (rows) and the number of constraints (columns), and C is a 32×1 vector, for the 32 constraints. In this case, since the oxygen amplitudes must average to zero at certain wavevectors, C is a vector of zeros.

To solve for the entries in the Q matrix, we begin with the quadratic potential energy terms for the degrees of freedom which need to be constrained (O_{in}, O_{out}, R). We also need to include terms in which these degrees of freedom couple to other degrees of freedom or one another. At high symmetry points where the motion of the oxygen ions must average to zero, we set the energy contribution of these polynomial terms to zero. We then use a plane wave ansatz for all ϕ and input the relevant values for the 26 relevant nearest neighbor vectors δ and the relevant wavevector (q).

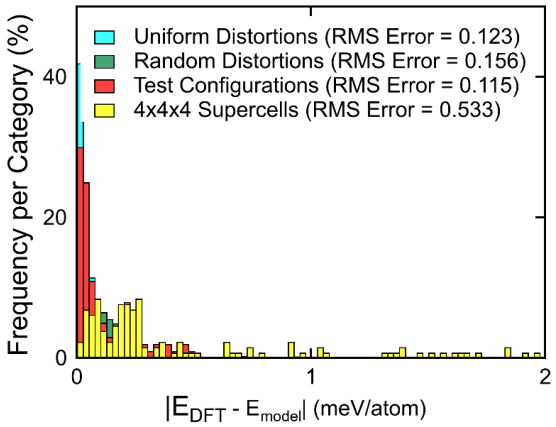

Figure 3.7: **Histogram of errors** The root mean square error and error distributions are shown for the different supercell constructions plotted in Fig. 3.6

Plugging in the plane wave ansatz to Eq.3.14 and simplifying we have:

$$0 = a_{000} + a_{100}\sum_{\delta} e^{-iq\cdot\delta} + a_{001}\sum_{\delta} e^{-iq\cdot\delta} + a_{101}\sum_{\delta} e^{-iq\cdot\delta} + a_{110}\sum_{\delta} e^{-iq\cdot\delta} + a_{111}\sum_{\delta} e^{-iq\cdot\delta} \tag{3.14}$$

For a given term in the polynomial (row of Q matrix), and a given constraint (column of Q matrix), the values of $\sum_{\delta} e^{-iq\cdot\delta}$ will give the corresponding Q matrix element. The full list of constraints is given in Appendix A.

In Fig. 3.7, the error distribution of the various supercell constructions plotted in Fig. 3.6 of the manuscript are compared. As expected, uniform distortions have the lowest error, while the randomly distorted supercells have the same general error distribution, but less sharply peaked near zero error. The test configurations, which were randomly constructed supercells not included in calculating the model parameters, were well-approximated by the model. The larger supercells do have higher error, possibly due to domain walls of the rotation order parameter which cannot occur in the smaller supercells, as well as the fact that next-nearest neighbor interactions are not considered. While the error of the $4 \times 4 \times 4$ supercells deviates from the model energies at higher

energies, configurations close to the ground state, which are most important in our simulations, are still well approximated. For instance, if considering only those $4 \times 4 \times 4$ configurations within 35 meV of the ground state energy, the RMS error is 0.175, which is comparable to the error of the random distortions of smaller supercells.

Finally, we calculated the phonon dispersion of our free energy model and compared it to the dispersion calculated by PHONOPY for the strained, centrosymmetric reference structure. Figure 3.6(b) compares the two phonon dispersions. Our model does not include all phononic degrees of freedom, and we therefore do not expect to accurately capture the high frequency bands. Instead, by using a simple model with a significantly reduced phase space volume, we are able to capture the relevant structural instabilities in the low energy phonon bands with near DFT-level accuracy.

Phonon dispersions are typically calculated by solving for the eigenvalues of the $3N \times 3N$ dynamical matrix. We simplify the computational problem by considering the amplitude of the polarization vector of the unit cell along $\hat{z}$ and the displacements of the oxygen ions in the rotations along $\hat{x}$ and $\hat{y}$ instead of considering the motion of every ion in all directions. To accomplish this, we use Lagrangian mechanics to work in a generalized coordinate system, and solve the Euler-Lagrange equations for the wavevector dependent frequency expressions. The full derivation of the phonon model is shown in Appendix A.

3.4.3 Zero-Temperature Calculations

After confirming the accuracy of the model, we used it to investigate the coupling between the polarization (P), rotation (R), and elongation (C) order parameters at zero temperature. These results are shown in Fig. 3.8. For each panel, the amplitude of a single order parameter (X) was fixed while the other order parameter (Y) was varied to

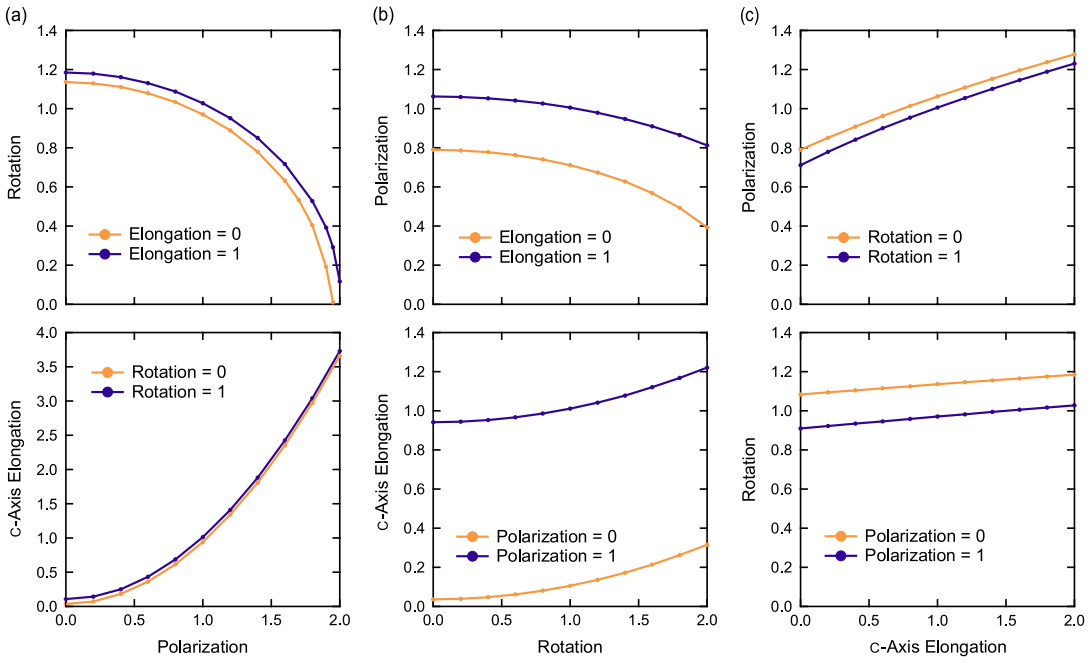

Figure 3.8: **Coupling between order parameters.** Dependence of the polarization (P), rotation (R), and elongation of the c-axis (C) on one another through minimization of the free energy. The axes are unitless and correspond to the normalized order parameters described in the main text. (a) The dependence of R (top) and C (bottom) on P. R is completely suppressed as P increases, while C becomes much larger with increasing P. (b) Dependence of P (top) and C (bottom) on R. P is suppressed while C increases slightly with larger R. (c) Dependence of P (top) and R (bottom) on C. P and R both increase with increasing C, although P has the strongest dependence on C.

minimize the free energy. The value of Y at this minimum is plotted in the figure for both the reference state and ground state values of the third order parameter (Z). A total of six combinations of X and Y are possible, and each pairing was explored. As shown in Fig. 3.8(a), increasing the polarization amplitude suppresses the rotation entirely and dramatically increases the elongation. When the rotation is increased [Fig. 3.8(b)], polarization is moderately suppressed and there is a slight elongation of the c-axis. Elongation [Fig. 3.8(c)] enhances both polarization and rotation, but the increase in P is much greater than the increase in R. In general, the change in $Y(X)$ is approximately the same for $Z = 0$ and $Z = 1$, but the overall amplitude is shifted in some cases. The

exception to this rule is that $P(R)$ decreases faster when $C = 1$ compared to $C = 0$. In summary, rotation and polarization are negatively correlated, although P suppresses R more strongly than R suppresses P. Elongation is positively correlated with both polarization and rotation, but the positive correlation between C and P is more significant than between C and R.

In addition to examining the coupling between order parameters, we performed calculations to determine the stability of polar domains. We found that abrupt domain walls between two oppositely oriented domains have a significant energy costs. It can be energetically favorable, however, for polar domains to form within an unpolarized reference state, which is likely to exist (at least on average) at temperatures above the ferroelectric transition. We performed zero-temperature calculations for clusters of varying dimensions to explore the energetics of domain formation within an unpolarized background. Clusters were embedded in an unpolarized supercell for two types of systems: one without octahedral rotations ($R = 0$), representing a system before the AFD transition, and one with rotations ($R = 1$) to emulate the system after the AFD transition. The elongation of the c-axis occurs concomitantly with the ferroelectric transition, so $C = 0$ in both cases. Inside the cluster, the magnitude of P was set to the value which minimizes the energy for a homogeneous system with the relevant amplitudes of R and C.

3.4.4 Monte Carlo Simulations

To incorporate temperature into our model, we used the Monte Carlo Metropolis algorithm to simulate the ferroelectric and AFD phase transitions with our free energy expression. We considered temperature-dependent fluctuations of the five separate degrees of freedom (the three components of the polarization order parameter, octahedral rotations, and the global elongation of the c-axis) for a $16 \times 16 \times 16$ supercell.

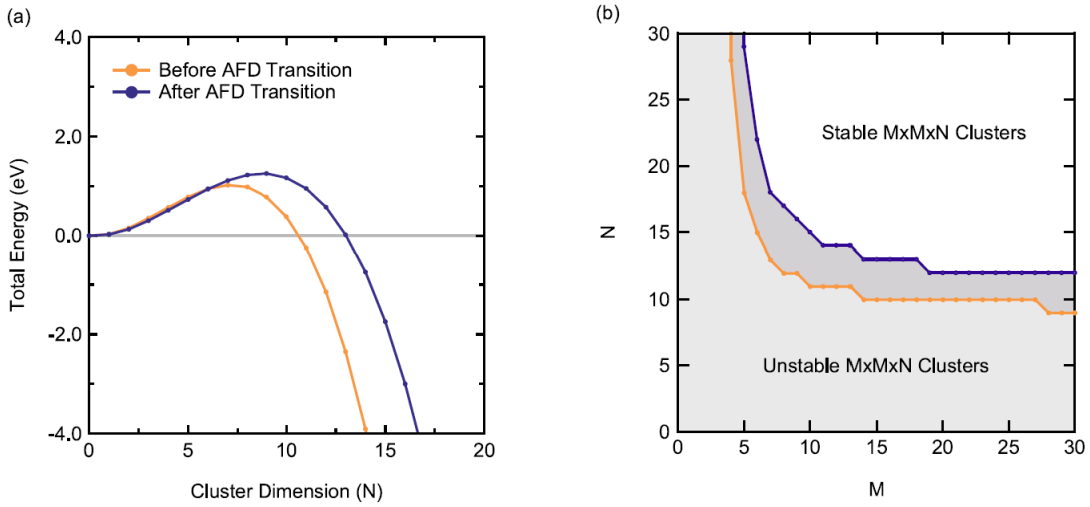

Figure 3.9: **Stability of polar clusters.** (a) Energy versus cluster size for $N \times N \times N$ polar domains embedded in an unpolarized background with $C = 0$ throughout the system and for both $R = 0$ (orange curve) and $R = 1$ (purple curve). (b) Map of stable cluster dimensions (negative cluster formation energies). The value of N for which the energy of an $M \times M \times N$ cluster becomes negative is plotted versus M.

Thermally-averaged order parameters are plotted versus temperature in Fig. 3.10(a,b). The transition temperatures for the ferroelectric and AFD transitions for our 1% compressively strained system were 280 K and 540 K, respectively.

We simulate the phase transition from low to high temperature. Within each iteration of the Metropolis algorithm, a separate trial move is made for each of the five degrees of freedom (DOF). Each trial move consists of adding random fluctuations of the DOF to each unit cell. The energy of the new configuration is calculated to determine whether the trial will be accepted or rejected. The step size of the fluctuation was adaptively adjusted to ensure an acceptance ratio of approximately 0.5. Acceptance rates for each degree of freedom are tracked separately, and each degree of freedom has its own adaptively updated fluctuation value. The average order parameter over all unit cells is calculated and stored for each DOF in every iteration. Iterations before reaching equilibrium are ignored. The final value of the order parameter at each temperature step is averaged

over millions of Monte Carlo iterations after ignoring the pre-equilibrium runs. Note that though we are individually updating the three separate DOF that comprise the polarization, only the global polarization is considered in the determination of T_c. The averaging of oxygen ions for both the rotation and polarization order parameters is taken into account in the Monte Carlo simulations by averaging between different unit cells as previously described.

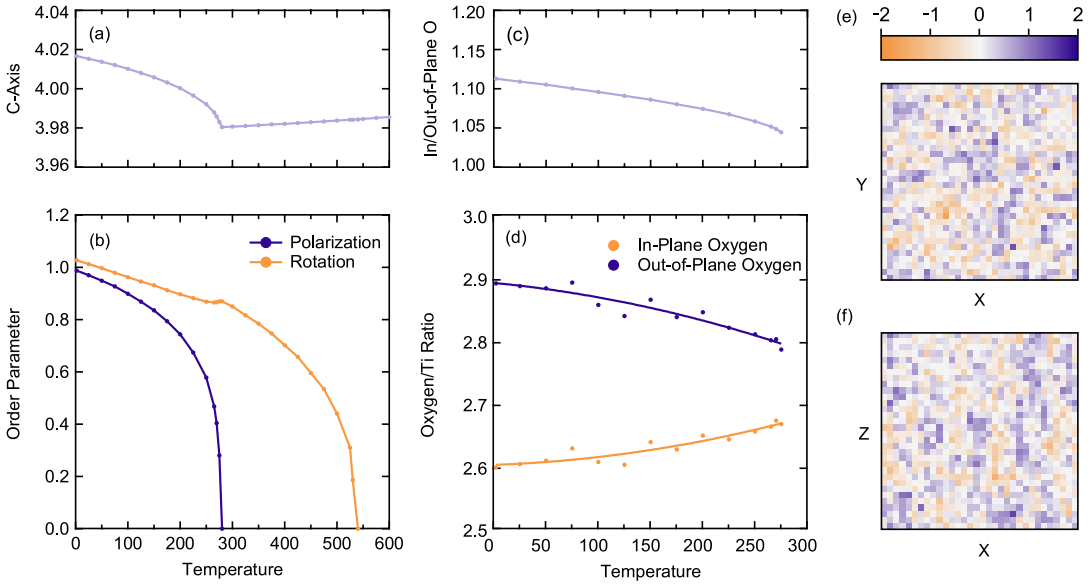

Figure 3.10: **Simulation of thermal phase transitions.** (a) The value of the c-axis lattice constant versus temperature. From low to high temperatures, the lattice constant decreases rapidly across the ferroelectric transition, then increases slightly due to thermal expansion. (b) The rotation and polarization order parameters plotted versus temperature. The ferroelectric transition occurs at 280 K and the AFD transition occurs at 540 K. The slight kink in the rotation curve at the polarization transition is due to coupling between the order parameters. (c) The ratio of the in- and out-of-plane oxygen displacement versus temperature, which decreases towards the ferroelectric transition. (d) Ratios of the oxygen to titanium displacement versus temperature. The ratio for in-plane oxygen atoms increases while that for out-of-plane oxygen atoms decreases slightly towards the polar transition. (e) Representative snapshot of the polarization order parameter in the xy-plane, showing polar clusters on the order of several unit cells. (f) Snapshot of the polarization order parameter in the xz-plane showing dominant correlations along the c-axis.

Table 3.9: Comparison of room temperature lattice parameters and transition temperatures.

Type	$\epsilon_{\parallel}$ (%)	$\epsilon_{\perp}$ (%)	a (Å)	b (Å)	c (Å)	T_{FE} (K)	T_{AFD} (K)	Δc (Å)	Ref.
Comp	-1	1.04	3.900	3.900	3.98	280	540	0.035	[97]
Comp	2	–	3.934	3.857	3.834	400	–	–	[43]
Comp	-0.8	–	–	–	–	110	320	–	[108]
Exp	-1.6	1.24	3.842	–	3.953	210	510	0.008	[107]
Exp	-0.92	0.71	3.869	–	3.933	155	370	0.004	[107]
Exp	-0.9	0.8	–	–	–	140	360	0.005	[109]

Near the transition temperature, finite size effects are evident in the plots of the average order parameter versus iteration number, and the system can flip from a positive value of the order parameter to a negative one. After several sign flips of the order parameter, we assume the order parameter will average to zero with infinite iterations. Temperature steps above the phase transition are not plotted in Fig. 3.10.

The influence of the DFT-calculated c-axis should be considered when evaluating the accuracy of our transition temperatures. It is well-known that while the LDA exchange-correlation functional underestimates the lattice parameters, the GGA functional (used in this work) overestimates them [106]. Table 3.9 compares our results to other experimental and computational studies of strained films. Shown are the room-temperature experimental and computational lattice parameters, ferroelectric (T_{FE}) and antiferrodistortive (T_{AFD}) transition temperatures, as well as the elongation of the c-axis in the ground state compared to the room-temperature phase (Δc). The room-temperature c-axis lattice constant in our simulation is approximately 3.98 Å, with an out-of-plane strain ($\epsilon_{\perp}$) of 1.04%. Experimental values of T_{FE} and T_{AFD} for a sample with $c = 3.953$ Å and $\epsilon_{\perp} = 1.24$ are 210 K and 510 K, respectively [107]. Given the overestimation of the lattice parameters by DFT, our transition temperatures approximately align with experimentally expected values for films with similar $\epsilon_{\perp}$.

A possible solution to the overestimation of the c-axis lattice constant could be pro-

vided by the strongly constrained and appropriately normed (SCAN) functional, which has been shown to give accurate energies and structural parameters for perovskite oxides [110]. In addition, the discrepancy in the transition temperatures could be due to the exclusion of anharmonic coupling effects of the low energy bands with higher energy phonon bands of the same symmetry. We also acknowledge that previous studies have found long range dipole-dipole interactions to be important, although they are computationally expensive to consider [111].

3.4.5 Evaluating Hamiltonian Parameters

In addition to simulating the thermal transition, we calculated the spatial correlation functions and probability distributions of the order parameters. The spatial correlation of the polar order parameter is defined as:

$$C(\delta) = \sum_i \frac{p_i p_{i+\delta} - \langle p_i \rangle^2}{\langle p_i^2 \rangle - \langle p_i \rangle^2}, \tag{3.15}$$

where p_i is the value of the polarization at site i and the vector δ indicates the distance and direction to the neighboring unit cell at site $i+\delta$. We find the strongest correlations are in the [001] direction. Figure 3.11(a) shows the correlation function along the [001] direction at several temperatures across the transition. Correlations are strongest at 290 K just above T_{FE} as random thermal fluctuations form domains that percolate into an ordered state.

The correlation lengths plotted in Fig. 3.11(b) were extracted by fitting the correlation functions to an exponential $C(\delta) = \exp(-\delta/L)$. The correlation length (L) is expected to diverge near the transition temperature. Finite-size effects in our simulation, however, limit this divergence, and $C(\delta)$ instead is found to approach a constant value as the spatial correlations exceed the system size. The maximum correlation length occurs just

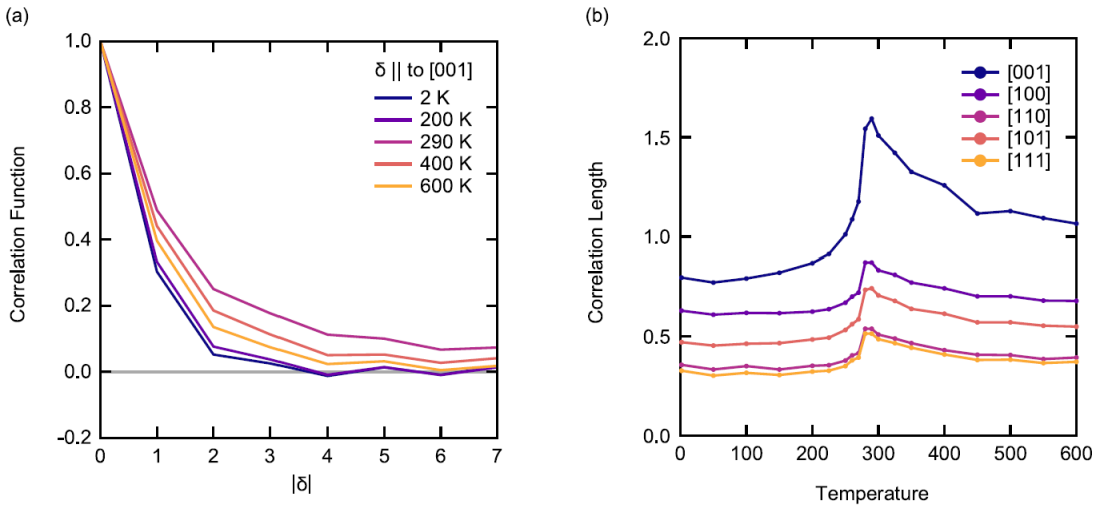

Figure 3.11: **Spatial correlation of the polar order.** (a) Calculated correlation functions, as defined in Eq. 3.15, versus $\delta \parallel [001]$ for various temperatures across the transition. (b) Correlation lengths extracted from the correlation functions for 5 high symmetry directions.

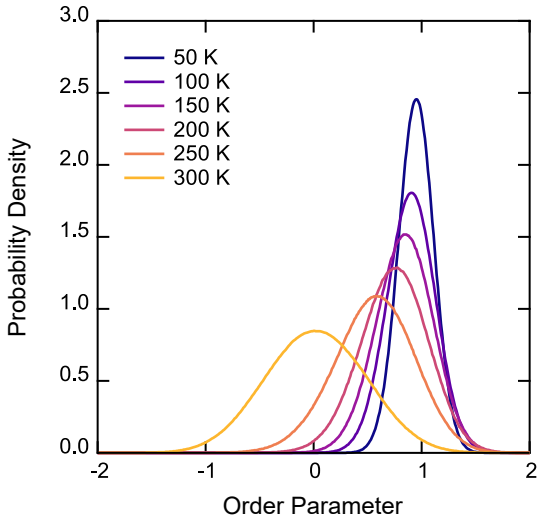

Figure 3.12: **Histograms of the polar order parameter.** Probability distributions for the polarization order parameter at various temperatures throughout the transition.

above the transition, with a value of 1.5 unit cell lengths, in accordance with the small domains visible in Fig. 3.10(e,f).

Histograms representing the probability distribution of the polarization order parameter at several temperatures across the transition are plotted in Fig. 3.12. The histograms are normalized such that the area under each curve equals one. The peaks shift from one for $T < T_{\mathrm{FE}}$ to zero for $T > T_{\mathrm{FE}}$. In a displacive transition, the probability distribution is sharply peaked at a single value that shifts with temperature. For an order-disorder system below T_{FE} we expect a double-peaked distribution with no amplitude where the order parameter equals zero.

Both experimental [42] and computational studies have found the ferroelectric transition in $SrTiO_3$ to have signatures of both order-disorder and displacive character. Computational studies using molecular dynamics to simulate phase transitions in strained $SrTiO_3$ have found double-peaked probability distributions with non-zero amplitude at zero polarization, indicating mixed displacive and order-disorder character [43, 108]. Our simulations do not exhibit this behavior. Given significant differences in the models, simulation techniques, DFT parameters, and the amplitude and direction of applied strain, it is challenging to reconcile this difference. Nevertheless, our high-temperature polarization histogram is sufficiently broad to indicate a mixed-character transition, and thus we are in qualitative agreement with the conclusions drawn from prior studies.

To quantify the displacive versus order-disorder character more precisely, we compared the relative strength of the single-site potential barrier and the intersite interactions. For displacive transitions, the coupling strength between neighbors outweighs the potential barrier, while the reverse is true in the order-disorder limit [112, 54].

Consider the general energy expression

$$H = \sum_i \left(-\frac{A}{2} p_i^2 + \frac{B}{4} p_i^4 \right) + \frac{C}{2} \sum_{i,j} (p_i - p_j)^2 , \tag{3.16}$$

where p_i represents the polarization in unit cell i. The first and second summation terms in Eq. 3.16 give the energy contribution of the single-site potential and intersite interactions, respectively. By examining the relative magnitudes of the A and C coefficients, the character of the transition can be approximated. The case where $C \ll A$ corresponds to the order-disorder limit, and $C \gg A$ to the displacive regime [54].

For our system, A and B were obtained by setting the rotation and elongation to their ground state values and varying the amplitude of the polarization order parameter. The DFT energy versus polarization amplitude was then fit to the polynomial $E(p) = -(A/2)p^2 + (B/4)p^4$. To calculate C, we considered the energy required to flip a single site in the ground state to the opposite polarization orientation, ΔE. This was calculated from DFT as the total energy of a $4 \times 4 \times 4$ supercell in the ground state with one site flipped, minus the total energy of the ground state structure. For the single-site-flipped configuration, the second sum in Eq. 3.16 will collapse since there is only a single flipped site, and the potential energy will cancel out when the ground state energy is subtracted, leaving $C = (B/4A)\Delta E$.

Our calculated C/A ratio is 1.26, indicating a slight tendency towards displacive character since $C > A$. This aligns with the single-peaked distributions shown in Fig. 3.12. The A and C parameters, however, are of nearly the same magnitude, and the observed signatures of order-disorder behavior are not surprising. These signatures include the stability of polar domains in an unpolarized reference state (Fig. 3.9), polar domains simulated by Monte Carlo [Fig. 3.10(e,f)], and the broadening of the probability distributions at high temperatures (Fig. 3.12), although overall the probability distributions

have characteristics of a displacive transition.

As first pointed out in prior experimental and computational work, $SrTiO_3$ is not easily classified into either limiting character. Indeed, the same Hamiltonian can describe both order-disorder and displacive ferroelectrics, and the overall character of the transition is ultimately determined by the comparative strength of continuous parameters of this Hamiltonian. As such, most real materials will fall somewhere along a continuous spectrum between the two extreme cases. We find that the binary classification of the polar transition in $SrTiO_3$ is limited in its descriptive power, and it is far more instructive to investigate the specific characteristics of the system, such as its lattice dynamics and domain structure.

3.5 Effects of Doping on Polar Order

[2] Our primary motivation for studying $SrTiO_3$ is to better understand the relationship between the polar order and superconductivity in this material. Superconductivity, of course, can only occur in the presence of free carriers, so we must expand our model to incorporate the effects of doping. We begin with the same relaxed ground state described in Section 3.4.1. Computational parameters are identical as those previously described. To obtain more accurate transition temperatures and compensate for the overestimation of the c-lattice parameter by the GGA approximation [106], the out-of-plane strain was set at the experimental value of 0.71% [107].

The relaxed lattice parameter for the bulk, cubic unit cell calculated by DFT was c_{bulk} = 3.939 Å, making the in-plane lattice parameters for the 5-atom unit cell under 1 % compressive strain a = b = 3.8995 Å. The out-of-plane strain was fixed at the experimental value of 0.71%, so that c = 3.9669 Å[107].

[2]The contents of this section are adapated from: "Effects of doping on lattice dynamics and polar order in strontium titanate," Alex Hallett and John W. Harter, *in preparation*.

Table 3.10: Ground state distortions for the three doping levels at $u_\perp = 0.71\%$.

Ion	Undoped	0.84 %	4%
Titanuium ($\hat{z}$)	0.196	0.174	0.142
In-Plane Oxygen ($\hat{z}$)	0.047	0.035	0.031
Out-of-Plane Oxygen ($\hat{z}$)	0.056	0.045	0.040
Rotation $\hat{x}/\hat{y}$	0.194	0.193	0.201

The out-of-plane strain, $u_\perp$, is given by:

$$u_\perp = [\frac{c_{strain}}{c_{bulk}} - 1] * 100 \tag{3.17}$$

After calculating the lattice parameters, a series of structural relaxations were performed at different doping levels, where only the atomic positions were allowed to relax. We found the ground state displacements of ions for $u_\perp = 0.71\%$ strain for three doping levels: undoped, 1.4×10^{19} cm^{-3} (0.84%), and 6.63×10^{20} cm^{-3} (4%). These displacements are tabulated in Tab.3.10. The carrier concentration was varied by setting the number of valence electrons in VASP using the NELECT tag. A compensatory background charge is applied to maintain charge neutrality.

3.5.1 Free Energy Model

Our free energy model for the doped system followed the same general procedure as described in Section 3.4.2, with some modifications. Coupling to the elongation degree of freedom of was not considered due to the fixed value of out-of-plane strain, reducing the total number of distinct terms in the free energy polynomial from 109 to 69. Similar to the previous formulation of the model, the ISOTROPY software suite [104, 105] was used to find all symmetry-allowed free energy terms up to fourth-order in rotation and polarization. In this formation of the model, we included onsite terms up to sixth order to eliminate divergences. The full energy expression is given in Appendix A.

Table 3.11: Types of calculations and the number of calculations performed

Type	Count
Random	489
Uniform	903
Total Included in Model	1392
Test Configurations	84
$4 \times 4 \times 4$ Supercell	34

Bulk $SrTiO_3$ does undergo a cubic-to-tetragonal phase transition which coincides with the onset of the octahedral rotations. The strained system, however, is already in the tetragonal phase and as the results of our previous simulation show in Fig.3.10(a), the additional elongation of the c-axis does not occur at T_{AFD}, but a large Δc is associated with the polar transition. Because the c-axis is already overestimated by DFT, we obtain much more accurate transition temperatures using the experimental out-of-plane strain of 0.71%.

After determining our polynomial expression for the free energy, we solved for the values of the coefficients using DFT to calculate the energies of $2 \times 2 \times 2$ supercell configurations and chose random values of each degree of freedom in each unit cell, as previously described in Section 3.4.2. In addition to these random calculations, we also included a set of specific uniform distortions. The energies of the same set of configurations were calculated for all three doping levels, obtaining three separate sets of model coefficients. A total of 1392 configurations were considered in calculating the model parameters for each doping level. The different types of configurations considered are listed in Tab.3.11.

After calculating the model parameters using least squares linear regression, we used the model to calculate the energies of 84 test configurations to confirm the generality of our free energy expression. The error in the calculated energies for these test structures was comparable to that of the training data set. We also calculated the energies of larger $4 \times 4 \times 4$ supercells to determine if excluding longer-range interactions affected

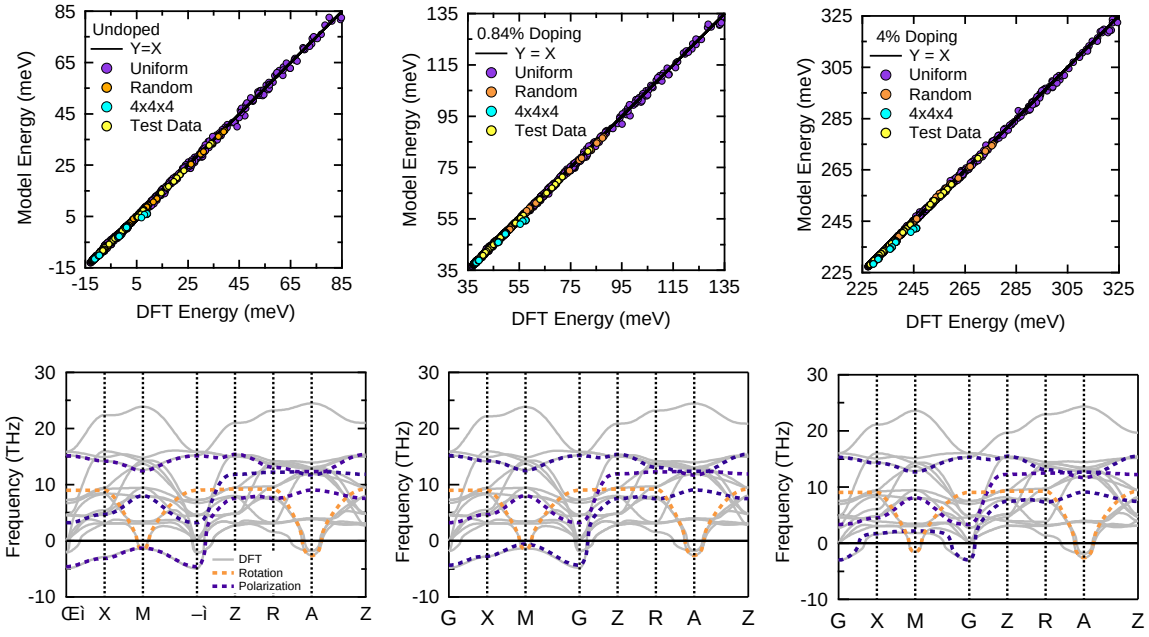

Figure 3.13: **Verification of the free energy model.** Plots of the energies of 1392 configurations calculated by our model versus the DFT-calculated energies for all three doping levels: (a) undoped (b) 1.4 $\times 10^{20}$ and (c) 6.63 $\times 10^{20}$. The model energies are in excellent agreement with DFT, with a root-mean-square error of 0.16, 0.14, 0.12 meV/atom from the lowest to the highest doping levels. (d-f) The 4 low-energy phonon bands (3 polarization, 1 rotation) calculated using our phonon dispersion expression are overlaid on the dispersion calculated using PHONOPY for the strained, centrosymmetric reference structure, showing that the simple model can capture the relevant instabilities with near DFT-level accuracy for all three doping levels.

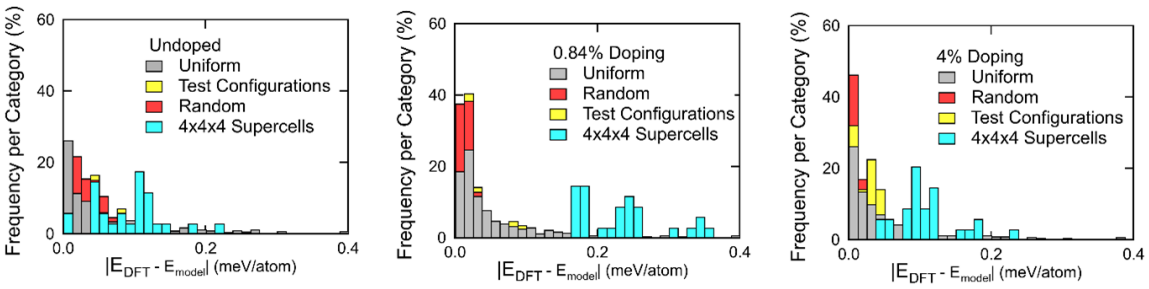

Figure 3.14: **Error distribution for different doping levels.** The histogram of errors for the different types of calculation are displayed for the three doping levels (a) undoped (b) 0.84% (c) 4%

the accuracy of the model. In this formulation of the model, we did not include the the $4 \times 4 \times 4$ supercells in the configurations used to calculate the model parameters, as the model does not account for next-nearest-neighbor interactions, and therefore including the larger supercells only worsens the overall performance.

The model energies are plotted versus DFT energies for each doping level in Fig. 3.13(a-c). The root-mean-square errors of the model energies relative to DFT for each doping level are 0.16, 0.14, and 0.12 meV/atom, ordered from lowest to highest doping. While the $4 \times 4 \times 4$ supercell energies deviate from the model at higher energies, they are accurately calculated by the model close to the ground state, which is most relevant in simulations of the phase transitions. The discrepancy between the DFT and model energies for the larger supercells far from the ground state could be due to domain walls in the rotation order parameter or increased coupling between next-neighbors at high displacement amplitudes.

Finally, we compared the phonon dispersion calculated by our free energy model to the dispersion calculated by PHONOPY, using inputs from density functional theory for the strained, centrosymmetric reference structure. Figure 3.13(d-f) plots the model and DFT phonon dispersions for each doping level. The derivation for the phonon model is provided in AppendixA. We do not expect to accurately capture the high-frequency bands with our model as we do not consider all phononic degrees of freedom. Our goal is to capture the relevant structural instabilities accurately with a dramatically reduced phase space volume. As seen in Figure 3.13(b), we successfully calculate the low-energy phonon bands with near DFT-level accuracy.

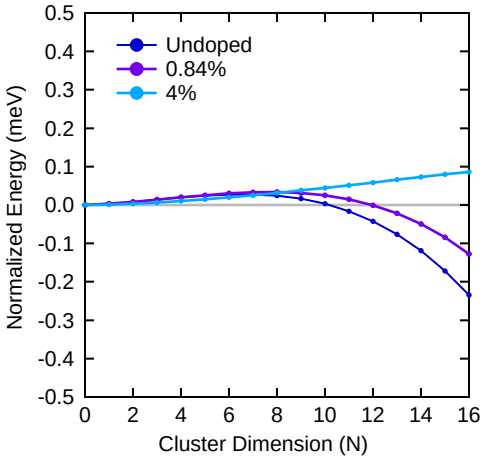

Figure 3.15: **Stability of polar clusters.** Energy versus cluster size for $N \times N \times N$ polar domains embedded in an unpolarized background where the rotation order parameter is set to the ground state value for each doping level.

3.5.2 Zero-Temperature Calculations

After validating the model's accuracy, we assessed the stability of polar domains across different doping levels according to the same procedure described in Section 3.4.3. Similar to the results shown in Fig. 3.9, our results reveal that abrupt domain walls between oppositely oriented domains incur significant energy costs. However, for an undoped or lightly doped system, it can be energetically favorable for polar domains to form within an unpolarized background. Such domains are likely to exist (on average) at temperatures above the polar transition. We performed zero-temperature calculations for clusters of varying dimensions to explore the energetic of domain formation within a reference state where the polar order parameter is zero, and the rotation is set to the ground state value for each doping level to represent the system after the AFD transition but before the polar transition. Inside the cluster, the magnitude of the polarization was set to the ground state value corresponding each doping level.

Figure 3.15 shows energy versus cluster size calculated using our free energy model.

When the system energy becomes negative, the formation of domains is favorable. This occurs for an $N \times N \times N$ domain when $N = 10$ for the undoped system, $N = 12$ for the 0.84 % system, and for the highest doping level, domain formation is never favorable. For the two lower doping levels, the energy increases initially from the cost of the domain wall ($\propto N^2$), but decreases when the cluster obtains a critical size as energy is lowered within the domain ($\propto N^3$). For the highest doping level, the energy is continually increased as domain formation is disfavored. These results are in agreement with the experimental observations that increased doping destroys polar nanodomains in strontium titanate [113].

3.5.3 Monte Carlo

We used the Monte Carlo Metropolis algorithm in combination with our free energy model to simulate the temperature-dependent ferroelectric and AFD phase transitions. We considered thermal fluctuations of the four separate degrees of freedom (the three components of the polarization order parameter and the octahedral rotations) for a 16 $\times$ 16 $\times$ 16 supercell. The thermally-averaged order parameters are plotted versus temperature in Fig. 3.16(a,b). The unitless order parameters are defined in section 3.4.3. The technical details of the Monte Carlo Simulation have been described in section 3.4.4.

Table 3.12 compares our results to experimental studies of strained, doped films. This table includes the doping levels, room-temperature experimental lattice parameters, ferroelectric (T_{FE}) and antiferrodistortive (T_{AFD}) transition temperatures. As previously mentioned, the out-of-plane strain in our simulation is set to the experimental value from [107]. The transition temperature of the undoped system is within 40 K of the experimentally measured transition temperature, which is an impressive quantitative agreement for such a simplified model. The polar transition temperature decreases with

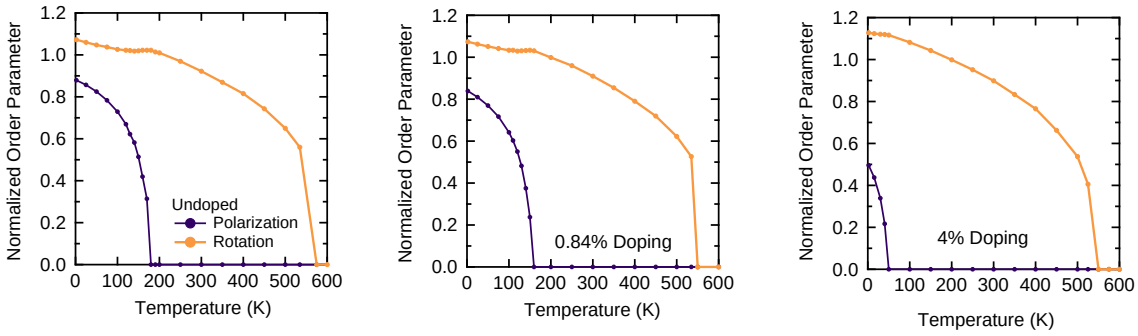

Figure 3.16: **Simulation of thermal phase transitions.** The rotation and polarization order parameters plotted versus temperature. The slight kink in the rotation curve at the polarization transition is due to coupling between the order parameters. (a) For the undoped system, the ferroelectric transition occurs at 180 K and the AFD transition occurs at 560 K. (b) At 0.84% doping, the ferroelectric transition occurs at 160 K and the AFD transition occurs at 550 K. (c) For the 4% doped system, the ferroelectric transition occurs at 50 K and the AFD transition occurs at 550 K.

increasing doping, which is in qualitative agreement with experiment [42].

In section 3.4.4, we pointed out that the overestimation of the c-axis lattice constant, and particularly the additional elongation form the reference to polar phase was a possible source of error in our transition temperature. Indeed, we found that by fixing the out-of-plane strain at the experimental value, we reduced the polar transition by 100 K, in much closer agreement with the experiment. An alternative solution could be provided by the strongly constrained and appropriately normed (SCAN) functional, which has been shown to give accurate energies and structural parameters for perovskite oxides [110]. The remaining discrepancies in the transition temperatures may be caused by the omission of anharmonic coupling effects of the low energy bands with higher energy phonon bands of equivalent symmetry. We also recognize that previous studies have found long-range dipole-dipole interactions to be significant. However, they are computationally expensive to consider [111].

Table 3.12: Comparison of transition temperatures for different doping levels.

Doping level	$\epsilon_{\parallel}$ (%)	$\epsilon_{\perp}$ (%)	a,b (Å)	c (Å)	T_{FE} (K)	T_{AFD} (K)	Reference
0	−1	0.71	3.8995	3.967	180	560	This Work
0.84	−1	0.71	3.8995	3.967	160	550	This Work
4	−1	0.71	3.8995	3.967	60	550	This Work
0	−0.9	0.8	–	–	140	360	[109]
0	−0.92	0.71	3.869	3.933	155	370	[107]
0.36	−1	–	–	–	92	–	[42]
0.84	−1	–	–	–	39	–	[42]
1.6	−1	–	–	–	None	–	[42]

3.5.4 Phonon Spectral Function

To observe the softening of the polar mode as a function of temperature and doping, we simulated the temperature dependence of the phonon spectral function using Langevin dynamics. As described in Chapter 1, the Langevin equation is a stochastic differential equation approximating the time evolution of a subset of macroscopic degrees of freedom in a system. The behavior of the faster, microscopic variables is incorporated through a stochastic term. The Metropolis Monte Carlo algorithm is useful for obtaining snapshots of the equilibrium polar order at different temperatures, but it cannot account for the dynamics of the system. To simulate for the dynamics of the system over time, which is required to obtain phonon frequencies, we use the Langevin equation. The majority of the simulation is performed in momentum space to simplify the computational problem. Oxygen atoms are shared between neighboring unit cells and therefore simulating in real space would necessitate solving many coupled differential equations simultaneously. The Langevin equation in momentum space is given by:

$$M(k)\ddot{\phi}_k = -K(k)\phi_k - \frac{\partial V_{NL}}{\partial x_k} - \gamma M(k)\dot{\phi}_k + M(k)^{\frac{1}{2}}\eta(t)\sqrt{2\gamma k_B T} \tag{3.18}$$

Eq.3.18 is written in the form of Newton's equation, $ma = \sum F$, summing over the quadratic, nonlinear, drag, and stochastic contributions to the forces, respectively. Similarly to the phonon model derived in Appendix A, Eq.3.18 can be written as a matrix equation, dividing both sides by $M(k)$ to isolate the acceleration term $\ddot{\phi}_k$. Here, ϕ_k is a 4×1 vector containing the values of the four order parameters at each k-point. The unitless, normalized order parameter is analogous to the "position" of a particle in classic Newtonian mechanics. The matrix form of $K(k)$ in the first term is of the same form for the ground state phonon dispersion discussed in Appendix A, where the force constants are given by the coefficients of the formulated free energy model for each doping level. The matrix $(\frac{\partial V_{NL}}{\partial \phi_k})$ is found by taking the derivative of the nonlinear terms of the free energy expression. These higher order contribution to the force must be computed in real space for computational efficiency. At each time step, the higher order forces are computed by plugging in the real-space values of the order parameters in each unit cell into the $(\frac{\partial V_{NL}}{\partial \phi_k})$ matrix.

The third term is the damping term, where the damping coefficient the value of γ is chosen to be 10^{12} Hz for the optimal convergence times. A larger γ is preferable, as it increases the degree of "thermalization" from one time step to another, decreasing the required length of the simulation. However, the damping coefficient will artificially broaden the spectral lines, and any spectral broadening we observe will ideally be from thermal or nonlinear effects, not damping, so a balance must be found between limiting artificial broadening and optimizing computational efficiency. The value of γ is chosen to be as large as possible while keeping the corresponding spectral broadening sufficiently narrow.

The last term is the random component of the force. We are simulating in momentum space, so the random components of the force at k and $-k$ must be complex conjugates to ensure that the forces are real when transformed into real space. In other words, k-points

are treated as time-reversed pairs. A separate random number is pulled from a Gaussian distribution for both the real and imaginary components. For the TRIM points, where $k = -k$, a single, real random force is used.

We begin in the ground state structure and simulate from high (500 K) to low (1 K) temperature for a 16 × 16 × 16 supercell. For every temperature step, we average over 10 runs after rejecting an initial, pre-equilibrium run. For each run, we simulate for a total of 65536 time steps of 10^{-15} s each, for a total 6.55×10^{-11} s. The minimum time step is chosen to be one tenth of the period of the fastest oscillation, and the total time is chosen to be 10 times longer than the slowest oscillation.

An individual run contains an outer loop over all time steps and an inner loop over all k-points. In the outer loop, the higher order forces are calculated with the real-space positions from the previous time step. Within the inner loop over each k-points, the sum over the forces is calculation for each k-points. To solve for the updated position (ϕ_k) and velocity ($\dot{\phi}_k$), we use the general scheme of Euler numerical integration:

$$v_{n+1} = v_n + F\Delta t \tag{3.19}$$

$$x_{n+1} = x_n + v_n\Delta t \tag{3.20}$$

In order to avoid divergences due to small numerical errors over time, the complex conjugate relationship between the forces at k and $-k$ is explicitly enforced at the end of each loop over the k points before storing the positions for each time step at a given temperature in a vector $\phi(t)$.

After a single run over all time steps is completed, the Fourier transform of the position versus time vector $\phi(t)$ is taken to get to frequency space $\phi(\omega)$. The intensity at each k-point is computed as the square of the Fourier amplitude $I(k) = \phi(k)^2$. For

the final simulation, we stored only the Γ point frequency for computational efficiency. The intensities at positive and negative time steps are added together to obtain the total intensity for a certain frequency value. The intensity maps are averaged together over the 10 runs performed at each temperature.

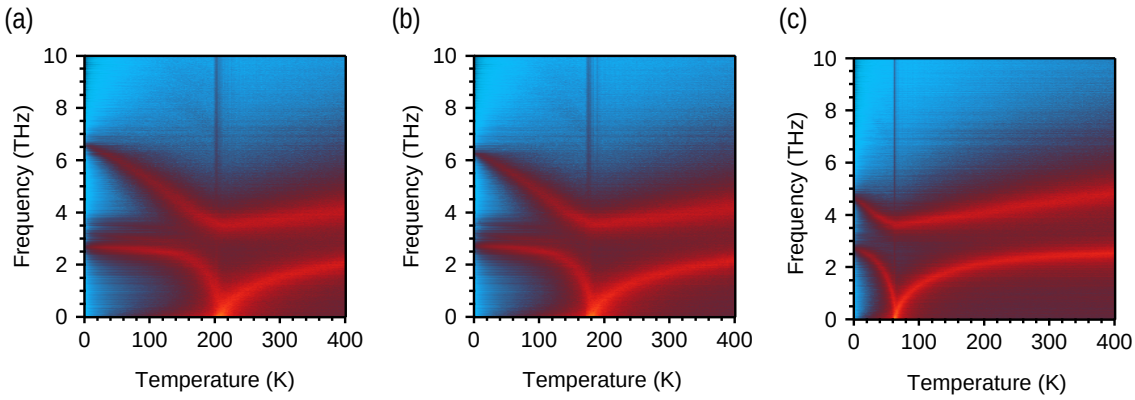

Figure 3.17: Temperature dependent phonon spectral function. The temperature dependence of the polar phonon modes at the gamma point are shown for the (a) undoped system ($T_c \approx 200$ K) (b) 0.84 % doping ($T_c \approx 180$ K) (c) 4% doping ($T_c \approx 60$ K). The transition temperatures are in qualitative agreement and within close quantitative agreement with the Monte Carlo simulations.

Before plotting the data, the logarithm of the intensity is taken to account for the wide range of values over the entire spectrum. The frequency of the polar modes at the Γ point is plotted as a function of temperature in Fig. 3.17 (a-c) for the undoped, 0.84%, and 4% doped systems. In Fig. 3.17 (a-c), the lowest energy polar mode softens to zero at the transition temperature, which is indicative of a displacive transition. The polar transition temperatures are 200 K, 180 K, and 60 K, in qualitative and close quantitative agreement with our Monte Carlo simulations.

The softening of the polar mode is in alignment with the many optical studies discussed in Section 3.3.1. Many optical studies show incomplete softening of the polar mode, where the frequency does not decrease all the way to zero. The complete softening ($\omega \rightarrow 0$) observed in our simulations may be a result of the uniformity of the charge

carriers, as we are not accounting for any local strain effects or disorder introduced by the dopant atoms. Additionally, film thickness is shown to lead to hardening of the polar mode, and we are not specifically simulating a thin film geometry. Similar to the experimental data available for $SrTiO_3$ we observe the presence of polar clusters, as shown by our Monte Carlo simulations, but still simulate the softening of the polar mode, further confirming the mixed character of the transition.

The relevance of the classification of the polar transition is to answer the question of whether Cooper pairing is likely mediated by quantum critical fluctuations of the polar mode. As previously discussed, binary classifications can be limited in their descriptive power, and it is important to look at the nuances of the specific electronic and structural degrees of freedom of the system. Within the polar phase, the soft mode frequency hardens again to $\omega_1 \approx 2.5$ THz for the lowest frequency mode and $\omega_2 \approx 6.5$ THz for the second polar mode. A third polar mode at $\omega_2 \approx 10$ THz is calculated, but is not plotted in Fig. 3.17 for clarity. Enhanced superconductivity is observed within the polar phase in compressively strained $SrTiO_3$ where this mode clearly has a finite frequency. This calls into question the relevance of quantum critical fluctuations of the soft mode as the mediator for Cooper pairing. In Chapter 4, we will discuss the relevance of the polar mode for pairing, within the ordered phase, in more detail.

3.6 Coexistence of AFD and Polar Order

[3]Our calculations of the ground state structures at different doping levels, as well as our Monte Carlo simulations, have demonstrated that doping suppresses the magnitude of the polar distortion and the likelihood that nanodomains will form. These conclusions are supported by prior imaging experiments [93, 113]. Recently, scanning transmission electron microscopy (STEM) imaging was performed on compressively strained, doped $SrTiO_3$ samples to investigate the effects of doping on the antiferrodistortive structural phase transition. We have performed first-principles calculations to support these experiments. In this work, Sm-doped $SrTiO_3$ 70-nm-thick films were grown by molecular

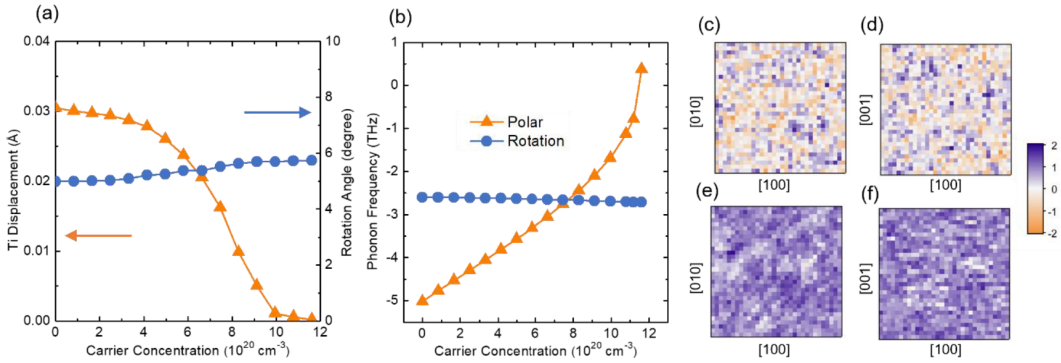

Figure 3.18: **First-principles simulations of AFD and polar order.** (a) The magnitude of ground-state Ti displacements (orange) and AFD rotation angles (blue) as a function of carrier concentration. (b) Imaginary phonon frequencies associated with the polar (orange) and AFD (blue) instabilities as a function of carrier concentration. (c)–(f) Representative snapshots calculated from Monte Carlo simulations at 300 K of the polarization (c,d) and rotation (e,f) order parameters for a $32 \times 32 \times 32$ supercell with carrier density 1.4×10^{20}cm^{-3}. The polarization snapshots show small domains with opposite polarization (orange and purple patches), while the rotation snapshots show a large single domain.

beam epitaxy on a (001) LSAT substrate which imposes a compressive biaxial strain of -0.9 % with carrier density of 9×10^{19} cm^{-3}, which corresponds to the peak of the

[3]The contents of this section are adapted from [114]:'Coexistence of antiferrodistortive and polar order in a superconducting $SrTiO_3$ film," Guomin Zhu, Alex Hallett, Nicholas G. Combs, Hanbyeol Jeong, Arda Genc, John W. Harter, and Susanne Stemmer, *Physical Review Materials*, 8, 001800 (2024): L051801.

superconducting dome. This film was previously observed to undergo ferroelectric (superconducting) phase transitions at 100 K (410 mK) [115]. Cross-section transmission electron microscopy (TEM) samples were prepared along two planes; the $(0\bar{1}1)$, parallel to the [001] direction, and $(1\bar{1}0)$, which is tilted by 45° against [001]. Annular bright field imaging of these planes gives the experimental rotation angle of $0.9° \pm 0.6$. The imaging experiments demonstrate the single-domain nature of the AFD order. More details on the experimental parameters and results can be found in [114].

To support these experimental calculations, we simulated the domain structure of both the polar and AFD orders using the free energy model described in Section 3.5.2. In Fig. 3.18(a), ground-state displacements associated with the polar and AFD orders, respectively, are displayed as a function of the free-carrier concentration at 0 K. As the carrier concentration is increased, the Ti displacements are reduced until the polar order is eventually destroyed. The AFD rotation angles, however, remain virtually unaffected by doping, though a moderate increase is associated with the destruction of polar order, as is expected due to the competition between these orders demonstrated previously in Fig.3.8. The calculated imaginary phonon frequencies (plotted as negative frequencies) of the polar and AFD instabilities are plotted as a function of carrier concentration in Fig. 3.18(b). While the polar distortion is strongly affected by doping, the rotation of the oxygen octahedra is essentially independent of the carrier density.

To visualize the domain structure at 300 K, representative snapshots of the polar and AFD-order parameters simulated by Monte Carlo are shown in Fig. 3.18(c) for a film with a carrier density of 1.4×10^{20} cm^{-3}. Each pixel represents a single 5-atom unit cell, with the color scale indicating the magnitude of the order parameter normalized to the ground-state value of the undoped system.

Table 3.13: Average Order Parameter

Doping concentration	No Doping	$1.4 \times 10^{20} cm^{-3}$	$6.63 \times 10^{20} cm^{-3}$
Rotation order parameter	0.8897	0.8863	0.8824

The rotation order parameter is multiplied by a phase factor where if i, j, k represent the unit cell indices in the x, y, z directions of the supercell, the final order parameter is:

$$R_{n,\text{uniform}} = R_n \times (-1)^{i+j+k} \tag{3.21}$$

This yields a uniform order parameter for the rotation, rather than a checkerboard pattern of out-of-phase displacements. Small variations of AFD order are primarily due to thermal fluctuations at 300 K; the rotation order parameter averaged over 500,000 Monte Carlo iterations shows small variations. Additionally, because the AFD and polar-order parameters are weakly coupled, polar domains may contribute to a small nonuniformity of the AFD order.

The relative independence of the AFD order parameter is further corroborated by the data in Tab.3.13, which shows the rotation order parameter averaged over a 16×16×16 supercell at room temperature for three different doping levels. A small variation of the average order parameter for separate Monte Carlo snapshots is to be expected, even at the same doping level. The room temperature AFD order parameter, in the absence of polar distortion, is independent of doping.

In summary, experiments and simulations demonstrate that the AFD transition in compressively strained, doped $SrTiO_3$ films occurs above room temperature, in agreement with previous results for undoped films [109][116]. The doped film studied in this work consists of a single, AFD domain similar to the undoped films [116]. The role of AFD domain walls in enhancing the superconductivity in compressively strained films [117] is ruled out by the single domain nature of the films. Our results demonstrate that the low-

temperature resistance anomaly seen in these films [117] and other ferroelectric $SrTiO_3$ samples [118] is not related the AFD transition or domain walls, as seen elsewhere [119], but rather with the ferroelectric transition, as found previously [117].

The relative insensitivity of the AFD transition to the presence of free carriers is demonstrated by simulations, and supported by the imaging experiments which find the AFD transition to occur above room temperature, similar to undoped strained films that have been studied previously [116]. The superconducting critical temperature depends strongly on doping, and thus the insensitivity of the the AFD order on carrier concentration suggests that there is no connection to the superconducting transition.

3.7 Conclusion and Outlook

We have derived a minimal free energy model of biaxially compressively strained $SrTiO_3$ that accurately reproduces the energies of disordered configurations and accounts for the coupling between rotation, polarization, and elongation of the c-axis. The thermal transition temperatures extracted from our model are consistent with experimental values, and our results show characteristics of both a displacive and order-disorder transition.

We have successfully incorporated the effects of doping into our model and found that doping suppresses the polar transition temperature and the magnitude of the polar order parameter, and makes the formation of polar domains unfavorable. Our simulations of the temperature-dependent phonon spectral function incorporate the effects of disorder and temperature into the phonon dispersion and demonstrate the broadening of spectral lines while showing transition temperatures in agreement with our Monte Carlo simulations. We observe similar phonon softening seen in experiments. In essence, we observe the coexistence of order-disorder and displacive character, the existence of polar nan-

odomains, as well as phonon softening, just as has been documented by the experimental studies outlined in Sections 3.2. We also confirm the hardening of the lowest energy TO1 mode to $\omega_{TO1} \approx 2.5$ THz within the polar phase, which is the relevant phase for superconductivity. Our model has also been used to complement STEM imaging experiments to confirm that the antiferrodistortive order, unlike the polar order, is relatively insensitive to doping, and is single-domain in nature, making it unlikely that antiferrodistortive domain walls influence superconductivity.

More broadly, the techniques implemented here to augment first-principles calculations to incorporate the effects of temperature and disorder can be applied to other systems. Many models which use Landau theory and density functional theory calculations to solve for the coefficients of invariant polynomials do not always take into account random fluctuations of individual order parameters and are therefore unable to simulate domain structure. Using Lagrangian mechanics in combination with a free energy model to calculate zero temperature phonon dispersions can also be implemented in a variety of material systems where calculating the full dispersion may be too computationally costly. We have also demonstrated that thermal effects and structural disorder can be incorporated into phonon spectral function models using Langevin dyanmics. Our methods can very easily be mapped to other perovksite oxides with similar structural degrees of freedom.

Chapter 4

Unconventional Superconductivity in Strontium Titanate

Our primary motivation for studying strontium titanate is to understand its unconventional superconducting phase, which emerges from an exceptionally dilute metallic state. Due to the presence of spin-orbit coupling and inversion symmetry breaking, a mixture of s- and p-wave order parameters is possible, which could result in a superconducting state with nontrivial topology.

This chapter will begin by giving a detailed overview of the electronic properties of the normal metallic state and our own electronic band structure calculations with spin orbit coupling for the polar phase will be discussed. Next, an overview of the proposed pairing mechanisms for strontium titanate will be outlined, focusing on two main theoretical frameworks; quantum critical fluctuations and broken inversion symmetry. Finally, we will discuss calculations of the Rashba splitting of bands in the polar phase, the density of states at the Fermi level as a function of doping, and the Migdal ratio as we place our results in the broader context of the literature.

4.1 Electronic Properties

In perovskite oxides, the O_h crystal field of the TiO_6 octahedra splits the five Ti $3d$ bands into two higher energy e_g and three lower energy t_{2g} bands. Strontium titanate is an insulator with an indirect gap between filled oxygen $2p$ states and three unoccupied Ti t_{2g} orbitals at the Γ point [39]. Spin-orbit coupling causes a splitting between the lower $j = 3/2$ multiplet and the higher energy $j = 1/2$ doublet in the high-temperature cubic structure. At low temperatures, the antiferrodistortive distortion is accompanied by a tetragonal transition, splitting the degeneracy of the $j = 3/2$ multiplet yielding three doubly degenerate bands at Γ [120]. The lowest energy band has a non-parabolic dispersion, beginning as a light band and becoming heavier at $k > 0.1/a$ due to an avoided crossing [9]. A schematic of the three Ti t_{2g} conduction bands is shown in the inset of Fig. 4.1. Doping can be achieved through the substitution of Sr^{2+} with a cation

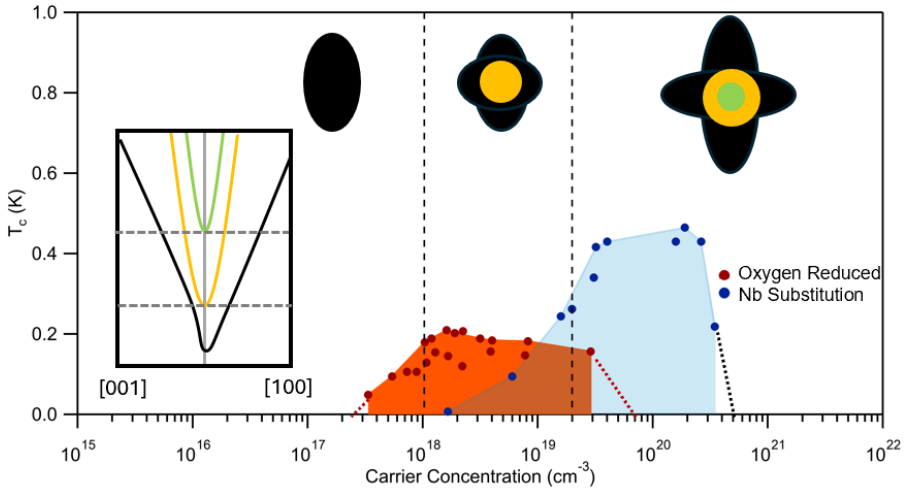

Figure 4.1: **Metallicity in Bulk $SrTiO_3$.** The x-axis spans the doping range of metallicity, from 10^{15}-10^{22} cm^{-3}. The one, two, and three band regimes are separated by two Lifshitz transitions at 10^{18} and $10^{19}cm^{-3}$, with schematic Fermi surfaces for each regime depicted at the top of the phase diagram. The lower left inset shows the Ti t_{2g} bands for the tetragonal I4/mcm structure along [001] and [100]. Superconducting domes with T_c on the order of several hundred millikelvin are shown for oxygen reduced [121] and Nb substituted [122] $SrTiO_3$. Figure adapted from [39].

containing an additional valence electron such as La [118] or Sm [117], substituting Ti^{4+} with Nb, or through oxygen reduction, which contributes two electrons per vacancy. Metallic behavior occurs at carrier concentrations as low as 10^{15} cm^{-3} [123], with a sharp Fermi surface emerging at 10^{17} cm^{-3} [124]. Fig.4.2 spans the range of carrier concentration where metallic behavior is observed for strontium titanate (10^{15} - 10^{22}). The dashed lines at 10^{18} cm^{-3} and 10^{19} cm^{-3} correspond to the Liftshitz transitions as the second and third bands begin to fill [39]. Schematics of 2D [001] slices of the Fermi surface in the one, two, and three-band regimes are depicted at the top of the phase diagram. The Fermi surface begins as an ellipsoid (blue), with a second semi-spherical Fermi surface emerging in the two-band limit (yellow), and a third emerging in the three-band regime (green). First principles calculations of the Fermi surface in the three-band regime for the polar structure will be discussed in the next section. Superconducting domes for oxygen-reduced [121] and Nb-substituted [122] $SrTiO_3$ are shown at carrier concentrations ranging from 2×10^{17} - 2×10^{21} cm^{-3} with a maximum critical temperature of around 500 mK.

The dilute metallic state is possible due to the large effective Bohr radius, which is defined as:

$$a^*_{Bohr} = \frac{4\pi\hbar^2}{e^2}\frac{\epsilon_0}{m^*} \tag{4.1}$$

The value of a^*_{Bohr} is determined by the permittivity (ϵ_0) and the effective mass (m^*). $SrTiO_3$ is a quantum paraelectric and therefore has an extremely high static permittivity, resulting in a^*_{Bohr} up to 600 nm. This exceptionally long effective Bohr radius protects the Fermi sea by increasing the Thomas-Fermi screening length, even though the Fermi energy (1 meV) is three orders of magnitude smaller than the band gap (3 eV) [9].

The unique metallic state in strontium titanate is characterized by the unusual temperature dependence of the normal state resistivity (ρ), which follows T^3 behavior at high

temperatures, before transitioning to T^2 in the low-temperature regime, following Fermi liquid behavior [125]. The T^2 dependence on the resistivity persists down to carrier densities as low as 2×10^{-5} per f.u. This behavior is similar to other aborted ferroelectrics, which suggests that the soft TO phonons may play a role in the form of $\rho(T)$ [9].

In $SrTiO_3$ samples where the polar order has been stabilized, anomalies in the resistivity occur at the onset of the polar phase transition, which can be attributed to a decrease in carrier density and increased film resistivity caused by the screening of polar charges which causes carriers to localize [42]. In our band structure calculations, we specifically investigate compressively strained $SrTiO_3$ within the polar phase, the effects of the polar distortion on the band structure, Rashba splitting, and the density of states.

4.1.1 Band Structure Calculations of the Polar Phase

Our band structure calculations for the cubic, tetragonal and polar phases presented in Fig. 4.2 were computed by DFT as implemented in VASP, following the same computational procedure as outlined in Chapter 3. Carrier concentration was varied by setting the number of valence electrons and applying a neutralizing background charge. Spin-orbit coupling is applied to all electronic band structure calculations within the noncollinear version of VASP, and symmetry is turned off. Non-spherical components to the charge density are included using LASPH = True to account for non-spherical components of the charge density, and LMAXMIX = 4 is used to account for the d-orbital contributions of the metal cations. In a compressively strained system, the ground state polar distortion causes the lowest energy band to shift downward. In the single band limit, the energy shift is dependent on the magnitude of the polar distortion, which in turn depends on the level of strain and doping. Similar to the low-temperature tetragonal phase, the Fermi surface of the polar phase is an ellipsoid elongated along $\hat{z}$. A 2D slice of the

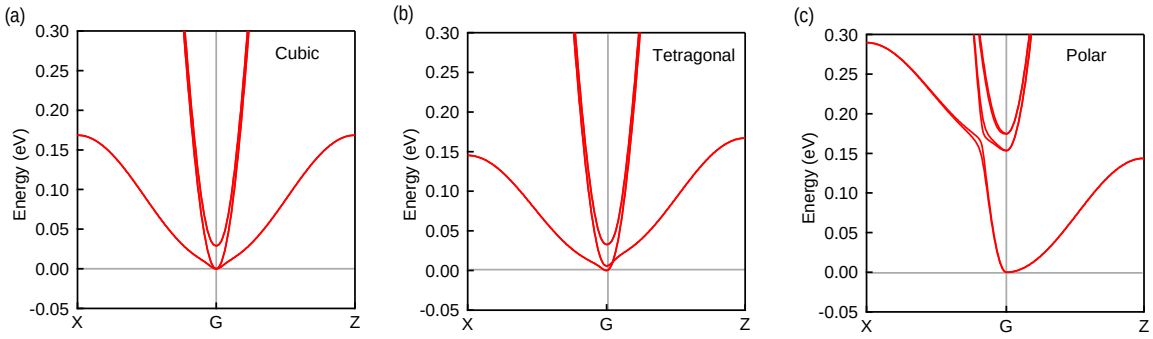

Figure 4.2: **Electronic Band Structures** Band structures for the undoped (a) cubic ($Pm\bar{3}m$) (b) tetragonal (I4/mcm) and (c) polar (I4cm) band structures along the path $X \to \Gamma \to Z$.

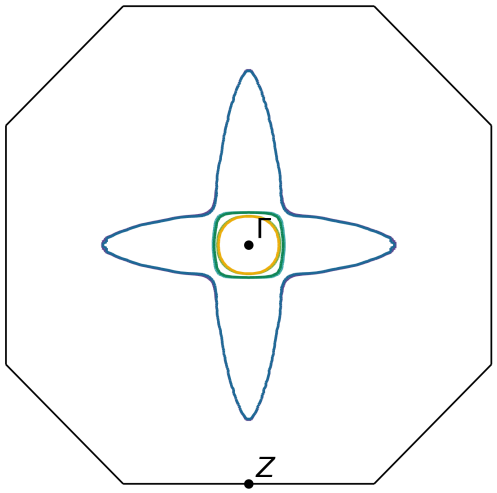

Figure 4.3: **Fermi surfaces of the polar phase in the three-band limit.** Three Fermi surfaces are presented corresponding to each of the three Ti t_{2g} bands. The topology of the Fermi surface for the I4cm polar structure, is similar to the I4/mcm tetragonal phase depicted schematically in Fig.4.1. Plotted using software from [126].

Fermi surface in the I4cm polar structure is shown in Fig.4.3, which evolves similarly as bulk $SrTiO_3$ with increased doping, depicted schematically in Fig.4.1. The primary difference between the polar and low-temperature tetragonal structures in the location of the Liftshitz transition, as the lowest energy Ti band is shifted downwards in energy, extending the region of the doping regime in the single band limit.

4.2 Overview of Proposed Pairing Mechanisms

Superconductivity was first observed in strontium titanate in 1964, yet a precise understanding of the microscopic pairing mechanism remains elusive. The first general theory for superconductivity in polar semiconductors developed by Gurevich, Larkin, and Firsov (GLF) in the early 1960s [127], and new mechanisms are being proposed up to the present. A summary of references that discuss these proposed mechanisms is given in Tab.4.1.

It is challenging to formulate apt theoretical descriptions of superconductivity in dilute systems due to the small density of states at the Fermi level, $N(0)$. In the weak coupling limit of BCS theory, the critical temperature can be expressed as:

$$T_c \approx T_D exp[-1/\lambda] \tag{4.2}$$

The electron-phonon coupling constant λ is given by $\lambda = N(0)V_{e-ph}$. An extremely strong e-ph interaction potential (V_{e-ph}) should be necessary to compensate for low $N(0)$, thus complicating theoretical treatments that implement approximations based on the assumption of weak coupling ($\lambda < 1$). The remainder of this section will outline the general principles behind the primary proposed pairing mechanisms to give context for our results.

4.2.1 Considerations for Polar Semiconductors

According to GLF theory, V_{e-ph} will never be strong enough to outweigh the Coulomb repulsion in non-polar semiconductors. However, exchange between *polar* LO phonons in the long-wavelength limit results in a lattice contribution to the dynamically screened Coulomb interaction which can account for pairing in the case where $\omega_{LO} << \epsilon_F$ [127].

In addition to providing a dynamical screening effect, long-range dipolar interactions also lead to energy splitting between LO and TO modes in polar materials. In $SrTiO_3$, the LO mode which originates from the same triplet as the soft TO1 mode is pushed to high energies (100 meV) in the long-wavelength limit. The low value of $N(0)$ in combination with high characteristic phonon frequency ω_{LO}, places STO outside the adiabatic regime, meaning that the conventional electron-phonon interactions described by BCS theory cannot account for Cooper pairing.

While the traverse optical mode remains within the adiabatic limit at 1-11 meV in doped thin films [39], coupling of the electron density to transverse optical phonons is not permitted by symmetry. Given a coupling of the form in Eq.4.3, the electron-phonon interaction vanishes for transverse modes.

$$H_{el-ph} = iV_0 \sum_q \mathbf{q} \cdot u_q \rho_{-q} \tag{4.3}$$

In 1974, Ngai proposed a mechanism involving the exchange of two TO phonons to circumvent this issue. Expanding the single-electron Hamiltonian in powers of the atomic displacements, one obtains a contribution from the second-order perturbation that consists of an effective electron-two-phonon interaction which involves an increase in the phonon density of states as compared to a single electron process. The interaction is expressed as a two-phonon deformation potential that can lead to an attractive interaction between electrons [128]. However, this higher-order interaction term is typically

too small to account for pairing [39]. Several other mechanisms involving the exchange of multiple LO phonons [129], LO-plasmon hybrid modes [130, 131, 78], plasmons [132], and polarons [133, 134] have also been proposed.

The superconducting critical temperature of strontium titanate is enhanced in proximity to and within the polar phase [117] [52]. Likewise suppressing polar order also suppresses T_c [77] [39]. This unique relationship between ferroelectric-like order and superconductivity has placed the polar instability at the center of many proposed pairing mechanisms.

Table 4.1: Superconducting Pairing Mechanisms

Mechanism	References
Intervalley Phonons (Disproof)	[135] [136] [137]
Transverse Optical Phonons	[40] [128] [52] [138] [139]
Longitudinal Optical Phonons	[140] [14] [78]
Critical Fluctuations	[11] [46] [14] [141] [142] [143] [75] [53]
Single TO Mode and SOC	[144] [145] [146]
Plasmon	[130] [132] [133]
Polaron Contributions	[134] [147] [148]
SOC/Inversion Symmetry Breaking	[28] [30] [149] [150] [151][139]
Filamentary Superconductivity	[152] [74] [153]

Due to the immense volume of research that exists on pairing mechanisms in $SrTiO_3$, it is not possible to discuss every proposed mechanism in detail here. The reader can refer to Tab.4.1 for references that support these theories. We will focus on two of the predominant theoretical frameworks for Cooper pairing established thus far: quantum critical fluctuations and inversion symmetry breaking in the presence of spin-orbit coupling.

The quantum critical fluctuation framework posits that the undoped edge of the superconducting dome corresponds to the emergence of the Fermi surface. The maximum T_c is pinned to the quantum critical point (QCP) where the soft mode goes approaches zero and the overdoped dome edge corresponds to the hardening of the polar mode[11].

There has recently been experimental evidence that does not align with the quantum critical framework. The enhancement of the superconducting critical temperature deep within the polar phase in combination with the observation of polar nanodomains above the polar transition temperature calls into question the validity of quantum critical fluctuations as the pairing glue. Instead, it is suggested that the primary condition for superconductivity is that Cooper pairing must occur in a noncentrosymmetric environment of greater length scale than the coherence length. In this framework, the overdoped side of the dome corresponds to the destruction of polar nanodomains rather than the hardening of the polar mode.

We will close by discussing the Rashba coupling mechanism, where symmetry arguments allow for coupling to a single polar phonon mode in the presence of inversion symmetry breaking and spin-orbit coupling. Theories supporting Rashba coupling do address the importance of inversion-symmetry breaking, but still align qualitatively with the idea the coupling will be enhanced in proximity to the quantum critical point and rely on a polar soft mode as the pairing glue. A unifying description that encompasses the superconducting behavior in the various structural phases of $SrTiO_3$ has yet to be formulated.

4.2.2 Quantum Critical Fluctuations

One of the early studies addressing the question whether quantum critical theory could be applied to quantum paraelectric was presented by Rowley et al. in 2014 [154]. It was found that a ϕ^4-quantum field model for critical behavior was relevant in to several quantum paraelectrics and could reproduce the temperature dependence of the dielectric function. In 2015, Edge et al. [11] investigated this idea by performing doping-dependent DFT calculations of the soft polar mode frequency. They found that the mode

became real at 10^{20} cm^{-3}, in alignment with the carrier concentration corresponding to the maximum T_c in the experimental data taken from [136]. They performed a theoretical treatment using the Eliashberg theory and obtained the following expression for the electron-phonon coupling in the limit of a van Hove singularity at $q = 0$:

$$\lambda = \alpha^2 \frac{1}{\omega_{q=0}(f_{18}, E_F)} \tag{4.4}$$

Here, α is a k-independent electron-phonon coupling, $\omega_{q=0}$ is the frequency of the soft TO1 phonon mode at the Γ point and f_{18} and E_F are the ^{18}O fraction and the Fermi energy, respectively. In this formulation, the electron-phonon coupling is clearly enhanced as the transverse optical mode softens.

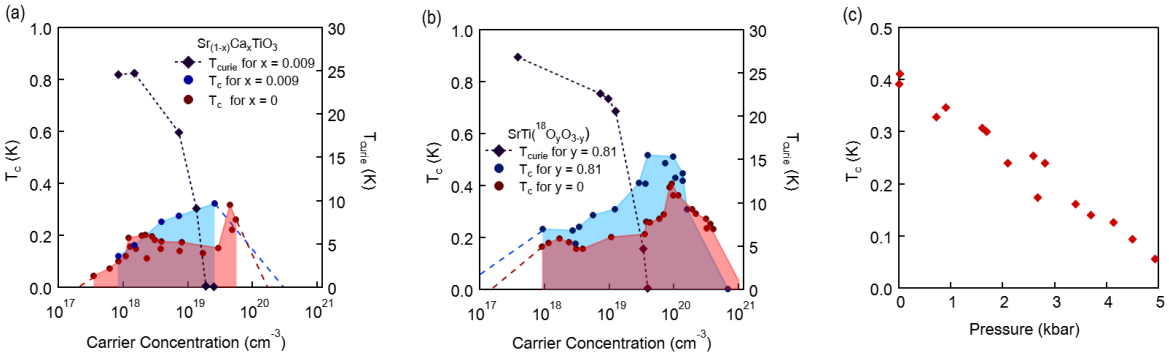

Figure 4.4: **Phase Diagrams supporting quantum critical fluctuation framework** (a) Superconducting dome of ferroelectric (blue) and paraelectric (red) $Sr_{1-x}Ca_xTiO_3$. The curie temperature (dashed line) is plotted along the right axis for $x = 0.009$. Superconductivity is enhanced in the vicinity of the quantum critical point. Data was re-plotted from [46]. (b) Critical temperature versus carrier concentration for paraelectric (red) $SrTiO_3$ and ferroelectric isotope exchanged STO18 (blue). The curie temperature is potted along the right axes. Superconductivity is enhanced near the quantum critical point. Data was replotted from [53] (c) Superconducting critical temperature versus hydrostatic pressure. Increased pressure leads to hardening of the polar mode and decreased superconducting T_c. Data was replotted from [77].

Fluctuations do not typically appear explicitly in the mathematical formulations provided by theorists, however, a unique perspective was given by Volkov et al., who sug-

gested that although the electron density cannot couple directly to the critical mode, indirect coupling could be mediated through the polar energy tensor [155].

Experimental studies have also been performed which support the enhancement of superconductivity in the vicinity of a quantum critical point from the paraelectric side. Schematic phase diagrams from these experiments are shown in Fig.4.4. In 2017, Rischau et. al measured the superconducting and critical temperatures in $Sr_{1-x}Ca_xTiO_{3-\delta}$ for $(0.002 < x < 0.2), (10^{-3} < \delta < 10^{-2})$ and found an enhancement of T_C in samples with $x = 0.009$. [46]. In 2022, a similar study was performed on $SrTi^{18}O_y^{16}O_{1-y}$, claiming that the trend of increasing T_c upon isotope substitution and decreasing T_c. This was combined with earlier work in 2018 from [77] showing the decrease in the normalized critical temperature with $1/\epsilon$, indicating a reduction of T_c correlated with the hardening of the polar mode.

While a great deal of work has been done in support of the quantum critical framework, it is still not clear precisely how the electron density couples to the $q = 0$ mode, nor is it in alignment with recent experiments showing the enhancement of superconductivity deep within the polar phase, which will be discussed in the next section.

4.2.3 Inversion Symmetry Breaking

As discussed in the previous chapter, HAADF-STEM studies were performed on STO films grown on LSAT under 0.9% compressive strain. Polarization orientation maps revealed the presence of polar nanodomains at room temperature, far above the polar transition temperature of 140 K. The observation of nanodomains in the paraelectric phase is consistent with an order-disorder phase transition [113]. The order-disorder character of the transition calls into question whether critical fluctuation of a soft phonon mode, a characteristic of a classic displacive transition, can fully explain Cooper pairing.

In Sm-doped films, polar nanodomains on the length scale of nanometers were observed at low doping levels (6×10^{19} cm^{-3}). Upon further doping (1×10^{20} cm^{-3}, 3×10^{20} cm^{-3}) both the length scale of the polar domains and the magnitude of the polar distortion decreased. In films where domains had been destroyed by dopants, no polar transition occurred [93], supporting the notion that cluster formation is a necessary precursor to global polar order. Furthermore, overdoped films that did not undergo a polar transition were not superconducting, indicating a connection between the inversion symmetry-breaking polar order and superconductivity [42].

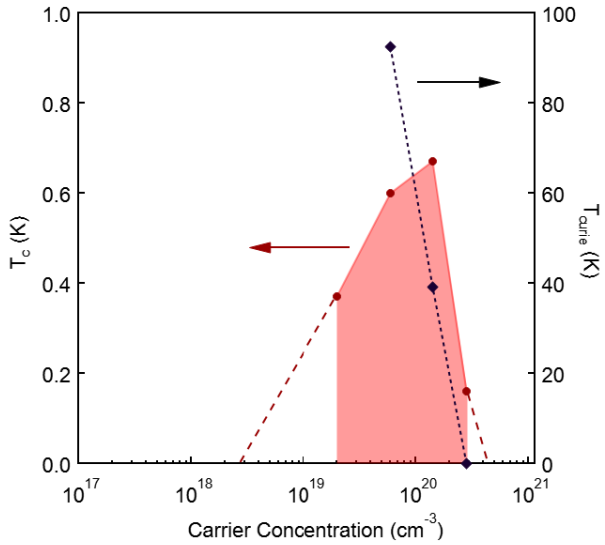

Figure 4.5: **Superconducting Phase Diagram** Superconducting critical temperature is plotted vs carrier concentration on the left axis, and the Curie temperature is plotted on the right axis. The highest superconducting T_c is in a sample with T_{curie} of $\approx$ 40 K, meaning that the film is deep within the polar phase at lower temperatures relevant to superconductivity. Data replotted from [42]

The relationship between precursor clusters of polar order and superconductivity was explored further by examining an unstrained paraelectric film at room temperature which was superconducting, but did not undergo any polar transitions. Polar nanodomains were present, and indeed were larger than those of a strained, overdoped sample with a lower critical temperature. [95]. Further evidence for the connection between the existence

of polar domains at high temperatures and enhanced superconductivity was provided by studies on partially strain-relaxed films. All films contained polar nanodomains and exhibited enhanced superconductivity compared to unstrained films, even though three out of the four films studied did not undergo a global polar transition [115]. These observations together suggest that inversion symmetry breaking may indeed be a *requirement* for pairing. In this framework, superconductivity occurs as long as the polar domains are larger than the coherence length of the Cooper pairs.

Superconductivity in noncentrosymmetric systems is often unconventional and can give rise to mixed-parity superconductivity [156]. Non-reciprocal transport, which is evidence of an odd parity superconducting channel has been measured in $SrTiO_3$ [30]. Support for an unconventional superconducting state in $SrTiO_3$ was also demonstrated by its insensitivity to magnetic impurities. Superconductivity persisted up to 3% doping with Eu, which is unexpected for conventional BCS superconductors that are highly sensitive to magnetic dopants [157].

There is a direct correlation between nanodomain size in the paraelectric phase and the superconducting and ferroelectric transition temperatures in doped, compressively strained $SrTiO_3$. As nanodomains are destroyed by nonmagnetic or magnetic dopants, or strain relaxation, films that do not have sufficiently large nanodomains at room temperature do not undergo a superconducting transition. These studies present strong evidence for inversion symmetry breaking and spin-orbit coupling as the key ingredients for pairing. In this framework, Cooper pairs effectively exist in a noncentrosymmetric environment, even in films that do not exhibit global polar order, such as unstrained or highly doped films. Superconductivity persists so long as the length scale of the nanodomains is longer than the coherence length of the Cooper pairs. The pairing glue in this scenario remains unknown, but the existence of a unconventional superconductivity is supported by nonreciprocal charge transport and insensitivity to magnetic dopants.

4.2.4 Rashba Coupling

Rashba coupling is a proposed pairing mechanism which combines aspects of both the quantum critical and inversion symmetry breaking frameworks. The suggested mediator for pairing is a single, soft TO1 phonon mode in the presence of strong spin-orbit coupling and inversion symmetry breaking. Coupling between the electron density and the TO phonons is typically prohibited since these modes do not generate a modulation of positive charge density. Tunneling between different t_{2g} orbitals on neighboring atoms is forbidden in an inversion symmetric system. Furthermore, pairing to TO modes is contrary to the idea presented by Anderson and Blout [8], that polar metallicity is possible when TO phonons do *not* interact with conduction electrons.

Several groups have presented possible pairing mechanisms based on the coupling of a single TO phonon mode in the presence of inversion symmetry breaking and anti-symmetric spin-orbit coupling [158, 146, 144]. They argue that because the TO phonon mode itself breaks inversion symmetry, new hopping channels between d-orbitals on nearest neighbor atoms are introduced, mediated by the oxygen p-orbitals. These hopping channels are shown schematically in Figure 4.6.

In 2022, Gastiasoro et al. [144] outlined a theory of Rashba coupling-mediated superconductivity in incipient ferroelectrics, considering only the paraelectric phase. They begin with a minimal tight binding model considering spin-orbit coupling, and the hopping channels introduced by the polar distortion of the lattice. The linearized gap equations at T_c can be written in terms of a four-component vector d_α for the even and odd-parity channels. The linearized gap equation is decoupled into orthogonal m channels $d^m_\alpha(\hat{k}) = \sum_l b^m_l y_{lm}(\hat{k})$ each with eigenvalue υ^m_a, which gives the BCS coupling constant:

$$\lambda^{(m)}_a = N_F \frac{g^2_{TO}}{\omega_{TO}} \upsilon^m_a \tag{4.5}$$

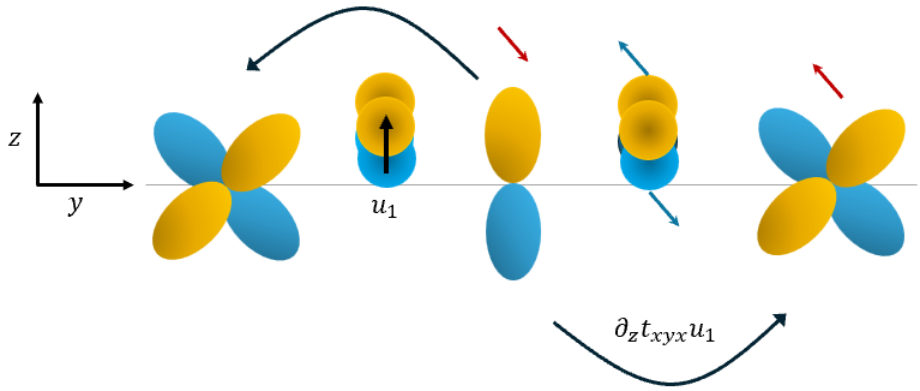

Figure 4.6: **Rashba coupling.** Inversion symmetry breaking of the polar mode u_1 along $\hat{z}$ allows for the hopping channel $\partial_z t_{xyx} u_1$ mediated by $|p_x \downarrow\rangle$ and $|p_z \uparrow\rangle$. Figure adapted from [159].

Here, $g_{TO} = \alpha_{TO} k_F$ gives the Rashba coupling strength. Numerical estimations of the coupling constant were made by considering $n \approx 2 \times 10^{18}$, corresponding to a T_c of 0.2 K. Using the experimental value for $N_F = 0.04 eV^{-1}$ obtained from specific heat measurements. The overall coupling was calculated as $\lambda_0^{m=0} \approx 0.01$ which is not sufficient to support $T_c \approx 0.2K$. They argue that since $\lambda_0^{m=0} \propto \omega_{TO}^{-2}$ the superconducting coupling constant grows as the system approaches the quantum critical point $\omega_{TO} \to 0$, and that tetragonal domains of AFD order may allow for variation of carrier concentration or the softness of the mode which may lead to filamentary superconductivity. However, as previously discussed, superconductivity persists in the polar phase, away from the quantum critical point, and within the polar phase, tetragonal domains of the AFD order are not observed. In 2023, they expanded on this formulation, deriving a generalized Rashba-like coupling between polar modes and conduction electrons at the zone center. They reproduce the dome-like dependence of $T_c/T_{c,max}$ in the single band limit, and find their optimum density in agreement with experiment [159].

Theoretical arguments based on Rashba coupling were presented by Yu et al. in 2022 [158]. They used experimental data to constrain their theoretical parameters and present

the most likely pairing mechanism for tetragonal, Nb-doped $SrTiO_3$ in the paraelectric phase. A single band approximation for the BCS eigenvalue for adiabatic pairing to a single TO1 phonon was compared to a three band model incorporating odd parity inter-orbital tunneling. The single-band approximation is given by:

$$\lambda_{BCS} \propto \frac{N_F}{\omega_T^2} \approx \frac{n^{1/3}}{K_0 + K_1 n} \tag{4.6}$$

An electron-phonon interaction term was then derived from a three-band tight-binding model including the symmetry-allowed d-orbital hopping channels for the noncentrosymmetric system. Using this electron phonon coupling, they derive the dimensionless BCS pairing interaction and compare the single-band and three band model presented in Eq.4.6 and find that the superconducting dome also arises with the unconventional, odd-parity electron-phonon coupling, where the optimal doping level is shifted slightly, but the suppression of superconductivity on the high density dome edge due to TO1 phonon hardening still remains.

Experimental data provided in [146], shows that the TO1 mode frequency remains below the Fermi energy across the doping range relevant to superconductivity, supporting the possibility of BCS-type pairing to this mode. They also performed planar junction tunneling experiments showing the superconducting gap was in agreement with the BCS value $2\Delta_0/k_B T_c$, and thus supporting the possibility of a conventional BCS pairing scenario with a single soft TO1 phonon mode.

While the studies discussed above consider only the paraelectric phase, one theoretical treatment, presented by Zyuzin et al. [139] proposed a theoretical model where conduction electrons interact with two phonons in the paraelectric phase. They generalize the two phonon mechanism to the ferroelectric case which allows for coupling to a single TO phonon.

While Rashba coupling takes into account the importance of inversion symmetry breaking and spin-orbit coupling, the arguments presented in this section generally align with the quantum critical framework. The aforementioned papers do not directly address the existence of superconductivity deep within the polar phase, where the polar mode has hardened.

4.3 Evaluation of Parameters Relevant to Superconductivity

[1]Much of the work done thus far to elucidate the pairing mechanism in $SrTiO_3$ (summarized in Tab.4.1) does not explicitly address the polar phase in the compressively strained system, with the exception of a few experimental studies [30, 117]. Here, we investigate parameters relevant to the superconducting phase including the Rashba splitting of the energy bands, the density of states at the Fermi level, and the Migdal ratio.

4.3.1 Rashba Splitting

As introduced in Chapter 1, in the presence of inversion symmetry breaking, antisymmetric spin-orbit coupling can split the energy levels of electronic bands and lead to spin-momentum locking. The splitting of the Fermi surface due to this inversion symmetry breaking is a key element of the Rashba coupling pairing mechanism.

The parabolic curve fits of the lowest, middle, and upper Ti t_{2g} bands for the undoped compressively strained polar structure are plotted in Fig.4.7(a-c), respectively along the path perpendicular to the direction of polar displacement ($-X \rightarrow \Gamma \rightarrow X$). The Rashba parameter is defined as $\alpha_R = \frac{2\Delta E_R}{k_R}$, where ΔE_R represents the difference

[1]The contents of this section are adapted from: "Effects of doping on lattice dynamics and polar order in strontium titanate," Alex Hallett and John W. Harter, *in preparation*.

between the energy at which the spin-up and spin-down bands cross, defined as zero energy in Fig.4.7(a-c), and the band minima. The value k_R is the wavevector corresponding to the band minima relative to the Γ point. The Rashba splitting decreases in intensity from the highest to lowest energy band. Fig.4.7(e) shows the decrease in the Rashba parameters of the lowest (α_{R1}), middle (α_{R2}) and, upper (α_{R3}) bands as the polar distortion is suppressed. Fig.4.7(e) shows the energy splitting between bands for the polar and

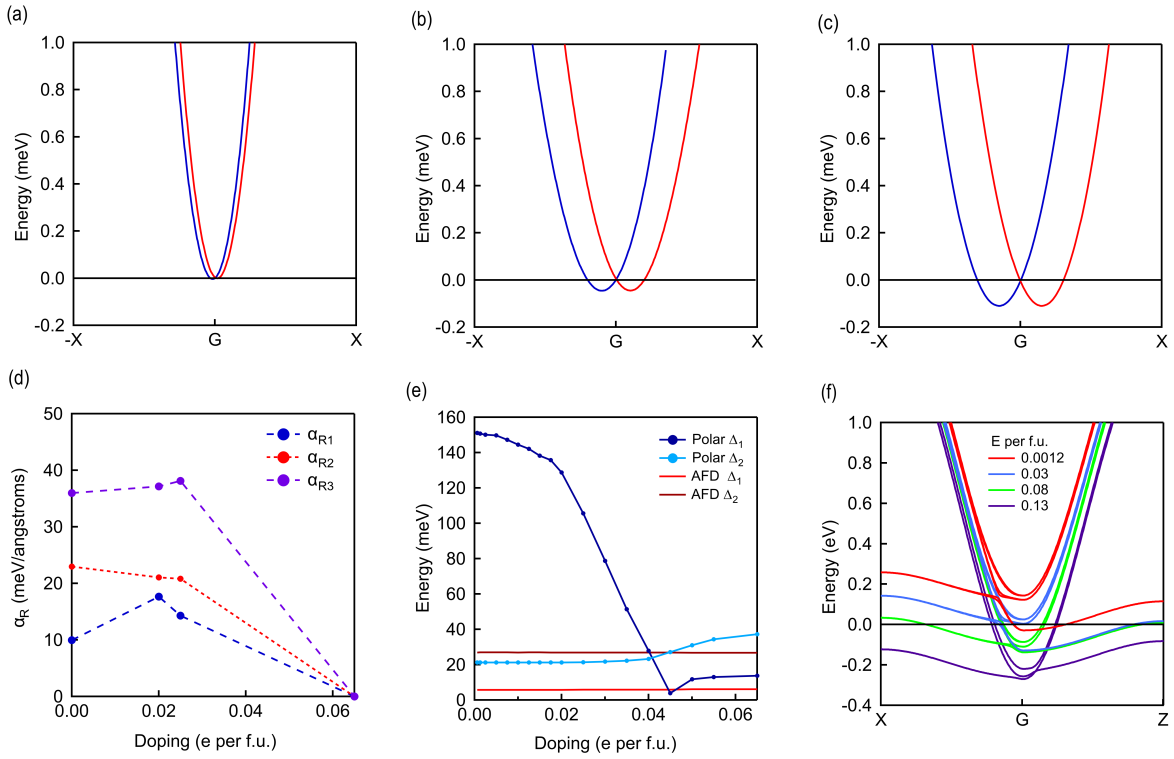

Figure 4.7: **Rashba Splitting** (a) Rashba splitting for the lowest ($\alpha_R = 10$ meV/Å) (a) middle ($\alpha_R = 23$ meV/Å) (b) and (c) highest energy ($\alpha_R = 34$ meV/Å) Ti t_{2g} bands of the undoped polar structure. The splitting decreases in magnitude from the highest to lowest energy band. (d) Rashba parameter versus doping. In the limit where the polar distortion is suppressed, the Rashba splitting goes to zero. (e) Energy splitting of the bands versus doping. While the energy splitting of the bands remains constant for the unstrained tetragonal structure (AFD Δ_1, Δ_2), the energy splitting due to the polar distortion (Polar Δ_1) changes drastically with doping, while Polar Δ_2 increases slightly as the polar distortion is suppressed. (f) Band structures at different doping levels showing the decrease in band splitting at higher doping levels as the polar distortion is suppressed.

AFD structures. The energy splittings Δ_1 and Δ_2 are the energy differences between the lowest and middle band, and the middle and upper bands, respectively, for both the polar structure and the unstrained structure with rotations (labeled as AFD). Since the AFD rotation angle is not dependent on doping, the bands rigidly shift below the Fermi level with increasing carrier concentration for the AFD structure, and the splitting between the bands remains constant. For the polar structure, the value of Δ_1 begins at around 150 meV, and then begins rapidly decreasing, until $n \approx 0.02$ e per f.u. as the polar distortion is suppressed, while Δ_2 remains constant until the structure approaches the unstrained centrosymmetric structure, and then increases slightly. At the highest doping levels where the polar distortion is completely suppressed, the energy splittings for the polar structure are slightly higher than those for the AFD structure, likely due to the increased elongation of the c-axis in the compressively strained system. The band structures at several doping levels are shown in Fig.4.7(f) depicting the change with doping as magnitude of the polar distortion decreases and the band structure approaches that of the strained, centrosymmetric strained.

As discussed in Section 4.2.4, previous work [144] found the overall coupling to be insufficient to support experimental transition temperatures, but argued that since $\lambda_0^{m=0} \propto \omega_{TO}^{-2}$ the superconducting coupling constant grows as the system approaches the quantum critical point $\omega_{TO} \to 0$, and that tetragonal domains of AFD order may allow for variation of carrier concentration or the softness of the mode which may lead to filamentary superconductivity. However, in the strained system, superconductivity is enhanced deep within the polar phase [42], where the phonon frequency has hardened to a finite value as we saw in our Langevin simulations in Chapter 3. Furthermore, both experimental and computational work has shown the AFD order to be single-domain in the compressively strained system, meaning that the filamentary superconductivity would not occur, and could not enhance or account for Rashba coupling. Furthermore, we find that in the strained system where the polar eigenvector is oriented along $\hat{z}$, the Rashba splitting is smallest in the lowest energy band, and that due to the increased energy splitting between the lowest and middle band, the strained system remains in the single-band regime up to higher doping levels compared to the AFD structure. This could mean that in the polar, compressively strained system superconductivity is occurring within the single band regime where the Rashba parameter is smallest and Rashba coupling would be expected to be weakest. Proposals for continued work quantifying Rashba coupling in the strained system will be discussed in Chapter 7.

4.3.2 Density of States

We have computed the density of states at the Fermi level $N(E_F)$, as well as the Fermi energy E_F from DFT calculations for the compressively strained polar phase, and unstrained tetragonal I4/mcm phase. The Fermi energy was taken to be the energy difference between the lowest band and the Fermi level computed by VASP. We first

performed self-consistent calculations to obtain the charge density file with spin orbit coupling, and then calculated the density of states using an 18×18×18 k-mesh for the primitive 10-atom unit cell.

Before computing $N(E_F)$ for the relevant low-temperature structures with spin-orbit coupling, we verified that our DFT calculations were yielding the expected dependence of $N(E_F)$ as a function of carrier concentration using an approximate ellipsoid model for the cubic and polar structures without spin-orbit coupling. In the single band limit, the Fermi surface of the polar structure is an ellipsoid elongated along $\hat{z}$. The energy dispersion in this limit can be approximated by a simple model:

$$E(k) = \alpha(k_x^2 + k_y^2) + \beta k_z^2 \tag{4.7}$$

The volume of an ellipsoid is given by $V = 4/3\pi abc$, where, in our case, a, b and c correspond to the length between the center and the edge of the ellipsoid along k_x, k_y, and k_z, respectively, as depicted schematically in Fig.4.8(a). The electronic band structures at different doping levels can be fit to parabolic curves $E_F = \alpha k_x^2$ and $E_F = \beta k_z^2$ to extract the curvature coefficients α and β. We can then compute $a, b = \sqrt{E_F/\alpha}$ and $c = \sqrt{E_F/\beta}$. The volume of the Fermi surface is then given by:

$$V_{FS} = \frac{4}{3}\pi\sqrt{\frac{E_F^3}{\alpha^2\beta}} \tag{4.8}$$

The number of carriers can be computed using Luttinger's theorem, which states that the volume enclosed by the Fermi surface is directly proportional to the particle density. The carrier density is given by the volume of the Fermi surface divided by the volume of the Brillouin zone ($N = V_{FS}/V_{BZ}$). We multiply by a factor of two to account for spin degeneracy at each k-point and plug in our volume expression from Eq.4.8 to obtain:

$$N = 2\left(\frac{L}{2\pi}\right)^3 \left[\frac{4}{3}\pi\sqrt{\frac{E_F^3}{\alpha^2\beta}}\right] \tag{4.9}$$

We can rearrange the constants and write Eq.4.9 as $N = S(E_F^{2/3})$, where the constant S is $S_{polar} = (V/3\alpha\beta^{1/2}\pi^2)$ for the polar structure and $S_{cubic} = (V/3\alpha\beta^{1/2}\pi^2)$ for the cubic structure. The expression for $N(E_F)$ can now be obtained by taking the derivative of N with respect to E_F:

$$DOS(E_F) = \frac{\partial N}{\partial E_F} = \frac{3}{2}SE_F^{1/2} \tag{4.10}$$

Similarly, we can verify the dependence E_F as a function of doping by inverting Eq.4.9 to obtain, $E_F = S^{-1}N^{2/3}$. The results from our ellipsoid model are compared to the DFT results in Fig.4.8(a,b). The DFT data is shown as markers for the cubic and polar structures. The values of $N(E_F)$ versus doping calculated from the ellipsoid model is shown as a shaded region, where the upper bound corresponds to the curvature coefficients for band structure with 0.015 additional carriers per formula unit, and the lower bound corresponds to the curvature coefficients of the undoped band structure.

A similar technique is used to calculate $N(E_F)$ and E_F for the cubic structure, where the Fermi surface can be approximated as three equivalent ellipsoids elongated along k_x, k_y, and k_z. To compare the density of states for the polar and cubic structures within the single band limit, we calculate $N(E_F)$ within a single ellipsoid, and divided the total density of states calculated from DFT by three.

The DFT calculations and ellipsoid model are in good qualitative and quantitative agreement, confirming that DFT gives reasonable results for $N(E_F)$. At higher doping levels (corresponding to higher E_F) the quadratic fit to the band structure becomes less accurate, leading to a deviation from the model at higher carrier concentrations.

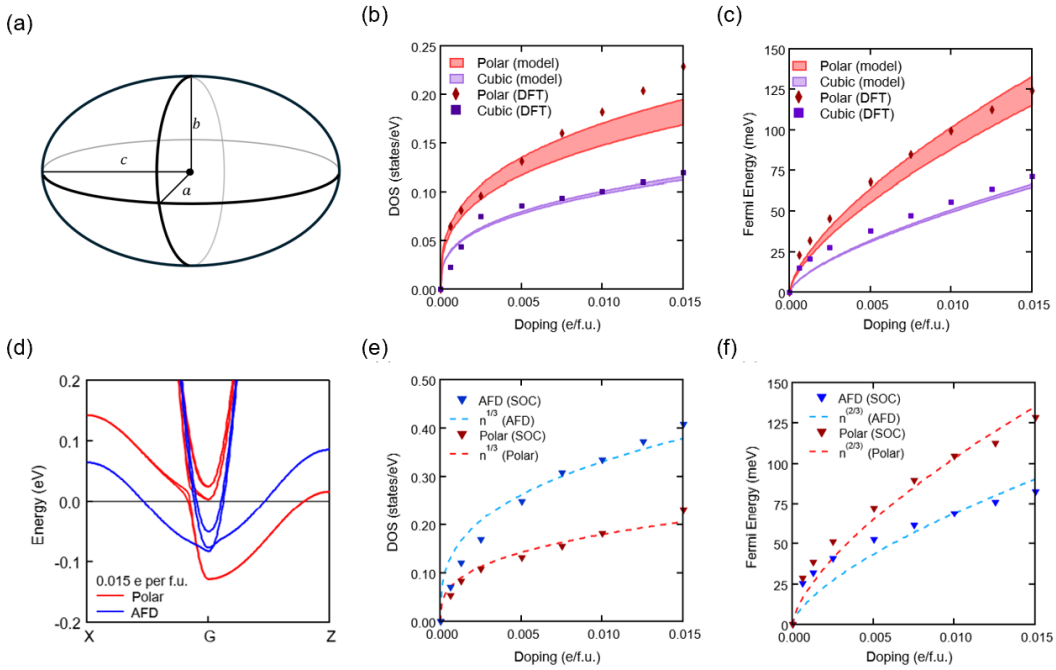

Figure 4.8: **Density of States at the Fermi level** (a) Schematic of an ellipsoid showing the parameters a, b, and c used in the ellipsoid model of the Fermi surface. (b) Density of states at the Fermi level versus doping for the strained polar and bulk cubic structures without spin orbit coupling. The DFT calculations (markers) are compared to the ellipsoid model (shaded region) where panels (b,c) the upper and lower bounds of the shaded region correspond to the model $N(E_F)$ calculated with curvature coefficients for the highest and lowest doping levels, respectively. (c) Fermi energy of the unstrained cubic and polar structures without spin-orbit coupling. The Fermi energy is calculated as energy difference between the Fermi energy output from the density of states DFT calculation relative to the lowest energy band. (d) Band structures for the unstrained tetragonal I4/mcm structure with octahedral rotations labeled as (AFD) and the strained polar structure and a doping level of 0.015 e per f.u., corresponding to the upper range of carrier concentration in panels (b,c) and (e,f). The polar structure is still within the single-band limit, while the AFD structure is in the three-band regime. (e) Density of states versus doping for the strained polar and unstrained AFD structures with spin orbit coupling. The dashed line fits the data with the idealized $n^{1/3}$ doping dependence predicted by the ellipsoid model, although here it serves primarily as a guide for the eye, as spin-orbit coupling limits the applicability of the idealized model. (f) Fermi energy versus doping for the AFD and polar structures. The dashed line fits the data with the idealized $n^{2/3}$ doping dependence predicted by the ellipsoid model, and serves primarily as a guide for the eye.

As expected, $N(E_F)$ is higher within a single band for the polar structure, since the energy splitting caused by the polar distortion pushes the lowest energy band below the Fermi level, and all the carrier density fills a single band instead of being spread evenly over three bands. These calculations explicitly demonstrate that a single band shifted below the Fermi level will yield a higher single-band density of states compared to a structure with three degenerate bands below the Fermi level, however, the tetragonal and antiferrodistortive phase transitions, in addition to spin-orbit coupling, cause band splitting that complicate the picture captured by this simple model.

Having used our ellipsoid model to ensure DFT yields the expected doping dependence for $N(E_F)$ and E_F, we now calculate these quantities for the relevant structures in the superconducting phase with spin orbit coupling (SOC): the polar structure and the low temperature tetragonal structure with antiferrodistortive rotations (AFD structure). The Fermi surface of the low temperature tetragonal structure cannot be approximated as three equivalent ellipsoids since the bands are no longer degenerate, so we do not attempt to develop an ellipsoid model for this structure. The total density of states per formula unit for the AFD structure is compared to the polar density of states in Fig.4.8(e). The dashed guidelines fit the data the $n^{1/3}$ doping dependence, and serve primarily as guides for the eye. The band dispersions for the polar (red) and AFD (blue) structures plotted in Fig.4.8(d) show that at the highest doping level of 0.015 electrons per formula unit, the polar structure is still within the single-band limit, while the unstrained AFD structure is in the three-band regime. At this doping level, $N(E_F)$ is approximately twice as high for the AFD structure as for the polar structure. Two of the AFD bands extend approximately the same distance below the Fermi surface, and the third uppermost band is also partially filled. If superconductivity occurs within a single band, which is a reasonable approximation, $N(E_F)$ within a single band is likely lower for the tetragonal structure. As shown in Fig.4.8(f), the Fermi energy, which is calculated as E_F extracted

from DFT relative to the energy of the lowest band, is higher for the polar structure. A higher density of states at the Fermi level within the single, lowest energy band for the polar structure could be one reason for enhanced superconductivity in the polar phase. Continuing work to quantify the single-band density of states in the AFD structure and to compare computational results to experiment will be discussed in Chapter 7.

4.3.3 Phonon Frequency

In Chapter 1, we introduced the Migdal ratio, the ratio of the characteristic phonon energy to the Fermi energy (ω_D/E_F). For conventional phonon mediated pairing described by BCS theory, the Midgal ratio must be much less than one in order to justify ignoring Coulomb repulsion and acheive a net attractive interaction between paired electrons. We calculate the Migdal ratio from first principles calculations for the two lowest energy polar phonon modes. The phonon frequencies were calculated using the density functional perturbation theory (DFPT) method implemented in VASP. For the phonon calculations, we include the small in-plane components of the polar distortion which are ignored in the calculations exploring the thermal phase space in Chapter 3 to avoid imaginary modes and to improve the accuracy of the calculated frequencies. The Fermi energies used to calculate the Migdal ratio are the same as those extracted from the density of states calculations described in the previous section.

In Chapter 3, our Langevin simulations calculated the frequency of the polar modes as a function of temperature. These results are shown in Fig.3.17. At low doping levels, the two lowest energy phonon modes have frequencies of approximately 2.1 THz and 6.2 THz. We identify these modes in our phonon frequency calculations. These modes are the only modes at low energy which show a significant dependence on doping. The mode around 2 THz (mode 1), and the mode around 6 THz (mode 2) are plotted versus

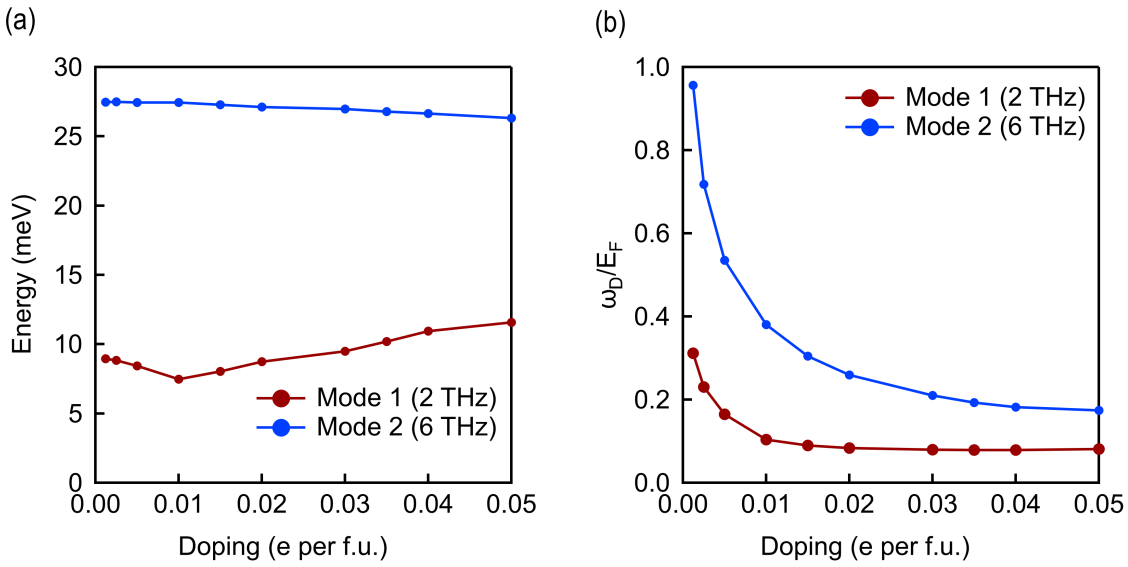

Figure 4.9: **Phonon Energies** (a) Energy of polar phonon modes plotted against carrier concentration (b) Migdal ratio versus doping.

doping in Fig.4.9(a). The lowest energy mode hardens slightly with increased doping, while the higher energy mode softens slightly. Given the doping dependence of the mode frequency, and the results from the Langevin simulations, the lowest energy polar mode is the relevant TO1 soft mode.

The Migdal ratio for the two modes is plotted in Fig.4.9(b). Both modes remain within the adiabatic regime (ω_D/E_F) << 1 throughout the doping range. The Midgal ratio decreases at higher doping levels as the increase in the Fermi energy outweighs the changes in the phonon frequency. The doping dependence of the soft mode [Fig.4.9(a)] and the fact the Migdal ratio calculated using the soft mode would place $SrTiO_3$ within the adiabatic regime [Fig.4.9(b)] could suggest that the TO1 mode plays a role in Cooper pairing. However, the specific mechanism through which electron density could pair to this mode has yet to be provided, since Rashba coupling, in addition to other phonon mediated mechanisms, do not appear to be strong enough to mediate Cooper pairing. Theories which posit that these phonon-mediated mechanisms may be strong enough

to mediate pairing near the quantum critical point do not explain the enhancement of superconductivity that we observe in strained films far on the ordered side of the quantum critical point. A theory for Cooper pairing in strontium titanate should explain superconductivity in all related systems, whether they be strained, isotope-exchanged, or Ca-substituted samples. So far, the proposed theories are not able to accomplish this.

4.4 Summary

We have calculated electronic band structures for the strained polar and unstrained tetragonal phases over a range of doping levels. We find that the polar distortion increases the energy splitting between the lowest energy band and the upper bands. Our density of states calculations indicate that in the limit of single-band superconductivity, an increased density of states within a single band could result in enhanced superconductivity within the polar phase. Experimental investigations of the Fermi energy, density of states, and the precise location of the Lifshitz transitions in the strained system could be useful in corroborating these results.

We also investigate the Rashba splitting in the polar structure and find that the Rashba splitting is lowest in the lowest energy band, which may be most relevant to superconductivity in the polar structure, where the single-band regime is relevant up to higher doping levels. Rashba coupling may not be sufficient to justify superconductivity in the polar phase.

The Migdal ratio is calculated from first principles over a range of doping levels for the two lower-energy polar modes, whose frequencies agree with the simulations of the phonon spectral function described in Chapter 3. We find the Migdal ratio to be within the adiabatic limit throughout the relevant doping regime. However, it should be noted that the eigenvectors and frequencies of the polar modes may differ from experiment.

Also, the level of carrier concentration required by DFT to suppress the polar distortion is much greater than experiment, which could influence the doping dependence of the phonon frequencies.

Chapter 5

Combinatorial Exploration of Herbersmithite-related Quantum Spin Liquid Candidates

5.1 Introduction

[1] In a quantum spin liquid (QSL), frustrated antiferromagnetic exchange interactions prevent localized spins from ordering at low temperatures, instead forming a fluid-like phase. The large degeneracy of this state can give rise to novel phenomena such as fractionalized quasiparticles, emergent gauge fields, and long-range entanglement [32, 161, 162, 163]. The kagome lattice of corner-sharing triangles is known to have high geometric frustration and is capable of hosting such a phase. A leading QSL material candidate possessing this structure is herbertsmithite [$ZnCu_3(OH)_6Cl_2$], which contains perfect kagome layers of spin-1/2 copper cations separated by non-magnetic Zn and Cl

[1]The contents of this chapter are adapted from [160]: "Combinatorial exploration of quantum spin liquids in the herbertsmithite material family," Alex Hallett, Catalina Avarvarei, and John Harter, *Physical Review Materials*, 7, (2023): 064403.

ions [164, 165], as shown in Fig. 5.1(a,c). Indeed, although herbertsmithite has strong antiferromagnetic exchange interactions, no magnetic phase transition is observed down to sub-kelvin temperatures [166, 167, 168, 169, 170], and an array of experimental and theoretical work favors a possible QSL scenario [171, 172, 173, 174, 175, 176, 177, 178, 179, 180, 181, 182, 178, 183].

Despite its many promising features, herbertsmithite is prone to cation substitutional disorder, where Cu may occupy interlayer sites and Zn may occupy intralayer kagome sites [166, 173, 184]. The precise amount of this disorder is debated. Several studies suggest that while there is minimal substitution of Zn on the kagome layers, the interlayer sites can be occupied by up to 15% Cu [185, 186, 171, 187], resulting in a decidedly off-stoichiometric compound. These interlayer "orphan" spin-1/2 Cu^{2+} defects are highly problematic for the QSL state, causing weak ferromagnetic interactions between kagome layers and distorting the surrounding matrix of magnetic ions [172]. Zn-substituted barlowite (Zn-barlowite), a structurally related compound and another potential QSL candidate [188, 189], is thought to have a much lower interlayer disorder concentration, largely due to the greater chemical distinction between the interlayer and intralayer sites, as shown in Fig. 5.1(b,d) [190, 191]. Experiments indicate that in Zn-barlowite, off-center interlayer C_{2v} sites can contain up to 5% Cu defects. Like herbertsmithite, however, Zn-barlowite does not order magnetically, even with these large concentrations of magnetic defects [192, 193]. While progress on this class of materials is encouraging, it is nevertheless desirable to further minimize orphan Cu spins to realize a clean QSL ground state.

Synthesizing compounds structurally similar to herbertsmithite and Zn-barlowite is a promising route to discover new QSL candidates. For example, Mg-substituted herbertsmithite, $Mg_xCu_{4-x}(OH)_6Cl_2$ (tondiite), has been successfully synthesized and shows no magnetic phase transition down to 1.8 K [194, 195, 196], and a Cd analog

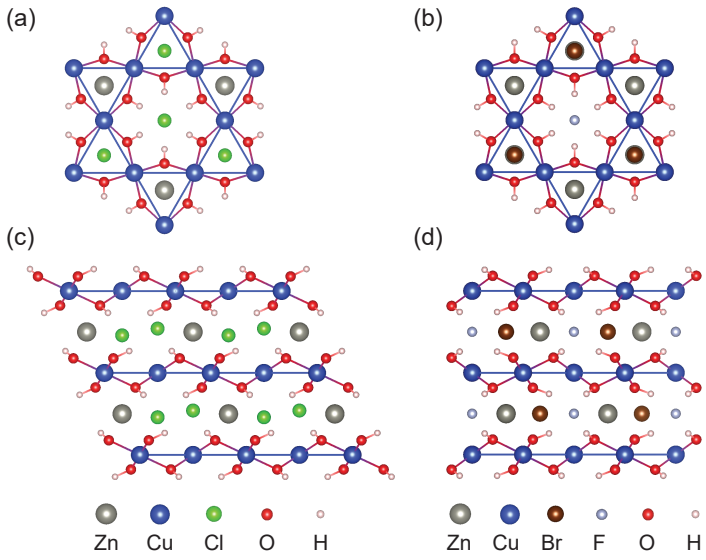

Figure 5.1: **Crystal structures of herbertsmithite and Zn-barlowite** (a) Herbertsmithite viewed along the c-axis, showing the kagome arrangement of Cu ions. (b) Zn-barlowite viewed along the c-axis. (c) Herbertsmithite viewed along the [110] direction, showing the shifted stacking arrangement of the kagome layers. (d) Zn-barlowite viewed along [110], showing the stacking of the kagome layers and the inequivalence of the Br and F sites.

$[CdCu_3(OH)_6Cl_2]$ shows no magnetic ordering down to 2 K, although it exhibits significant distortions of the kagome planes [197]. Synthesis of the bromide analog of herbertsmithite $[ZnCu_3(OH)_6Br_2]$ was attempted but unsuccessful [198]. A Zn-barlowite related structure, Zn-claringbullite $[ZnCu_3(OH)_6ClF]$, shows no obvious magnetic transition down to 2 K, but a perfectly stoichiometric compound was not achieved [199]. While the Mg analog of barlowite cannot be synthesized due to the insolubility of MgF_2 in water, the bromide analog was attempted $[MgCu_3(OH)_6Br_2]$, but did not have the Zn-barlowite structure and ordered antiferromagnetically at 5.4 K [200].

Clearly, more work is needed to search for and identify viable candidates in this material family. Only a few computational studies exist exploring cation substitution in barlowite [190, 191], and a complete exploration of the structural families of herbertsmithite and Zn-barlowite using computational methods has not been performed. Here, we use *ab*

initio calculations to systematically explore compounds within the herbertsmithite and Zn-barlowite families. We compare the thermodynamic stability, structural properties, and tendency towards disorder. After considering all these criteria together, we select promising QSL candidates that merit further experimental and theoretical examination.

5.2 Computational Methods

We carry out a systematic exploration of the structural relatives of herbertsmithite [$A\mathrm{Cu}_3(\mathrm{OH})_6B_2$] and Zn-barlowite [$A\mathrm{Cu}_3(\mathrm{OH})_6BC$] by substituting closed-shell (spinless) 2+ cations (A = Ba, Be, Ca, Cd, Ge, Hg, Mg, Pb, Sn, Sr, Zn) and halide anions (B, C = Br, Cl, F, I). We investigate all 44 possible herbertsmithite relatives. While there are 176 possible Zn-barlowite relatives, we eliminate compounds where $B = C$ because the herbertsmithite structure always has lower energy in these cases. We also do not consider compounds in which the less electronegative anion occupies the C site [the site occupied by F in Fig. 5.1(b,d)]. All hydrogen bonds are oriented towards the C site, so the more electronegative ion will always occupy this position to minimize energy. Thus, a total of 66 relatives in the Zn-barlowite family were selected for consideration.

We perform high-throughput calculations where the structural optimization of each candidate is followed by a static calculation to extract the ground-state energy and to compute phonon frequencies at the Γ point to confirm structural stability. In addition to confirming the stability of the relaxed structures, we perform convex hull calculations to determine if synthesis of the candidate compounds is thermodynamically feasible. For the most promising materials, we also calculate defect formation energies and full phonon dispersions throughout the first Brillouin zone to verify stability at k-points away from the zone center.

All structures were calculated by allowing the lattice parameters, cell volume, and

atomic positions to fully relax using density functional theory (DFT) as implemented in the Vienna *ab initio* simulation package (VASP) [98, 99, 100]. We used the supplied projector augmented wave potentials [101] within the generalized gradient approximation and Perdew-Burke-Ernzerhof scheme [102]. Electronic wave functions were expanded in a plane wave basis set with an energy cutoff of 800 eV, and reciprocal space was sampled using an $8 \times 8 \times 8$ k-point mesh for herbertsmithite-related structures and an $8 \times 8 \times 5$ k-point mesh for Zn-barlowite-related structures. A Γ-centered mesh is necessary due to the hexagonal symmetry of Zn-barlowite. The spacing between k-points was $\sim$0.15 Å^{-1} for both structural families, and this spacing was also used for calculating the energies of binary compounds used in the convex hull analysis. All structures were relaxed until forces on the atoms were less than 1 meV/Å. Calculations were non-spin-polarized.

5.3 Structural Stability

Phonon calculations at the Γ point for the fully-relaxed structures were performed in VASP within the finite differences approximation to confirm structural stability. As expected, many structures have unstable phonon modes. Fig. 5.2(a,b) shows the frequency of the lowest energy optical phonon mode, f_0, for all compounds. In all subsequent plots, the unstable compounds (with $f_0 < 0$) are marked with an 'X' to distinguish them from structurally stable and potentially viable candidates. Cations are shown on the vertical axis and anions on the horizontal axis, in order of increasing ionic radius from bottom to top and left to right, respectively. The reference compound, either herbertsmithite or Zn-barlowite, is shown in white and marked with an asterisk. Compounds with parameter values more favorable than the reference compound are shown with warm colors, and values less favorable are shown with cool colors. For example, a higher frequency of the lowest energy optical mode indicates higher dynamical stability, so higher frequencies are

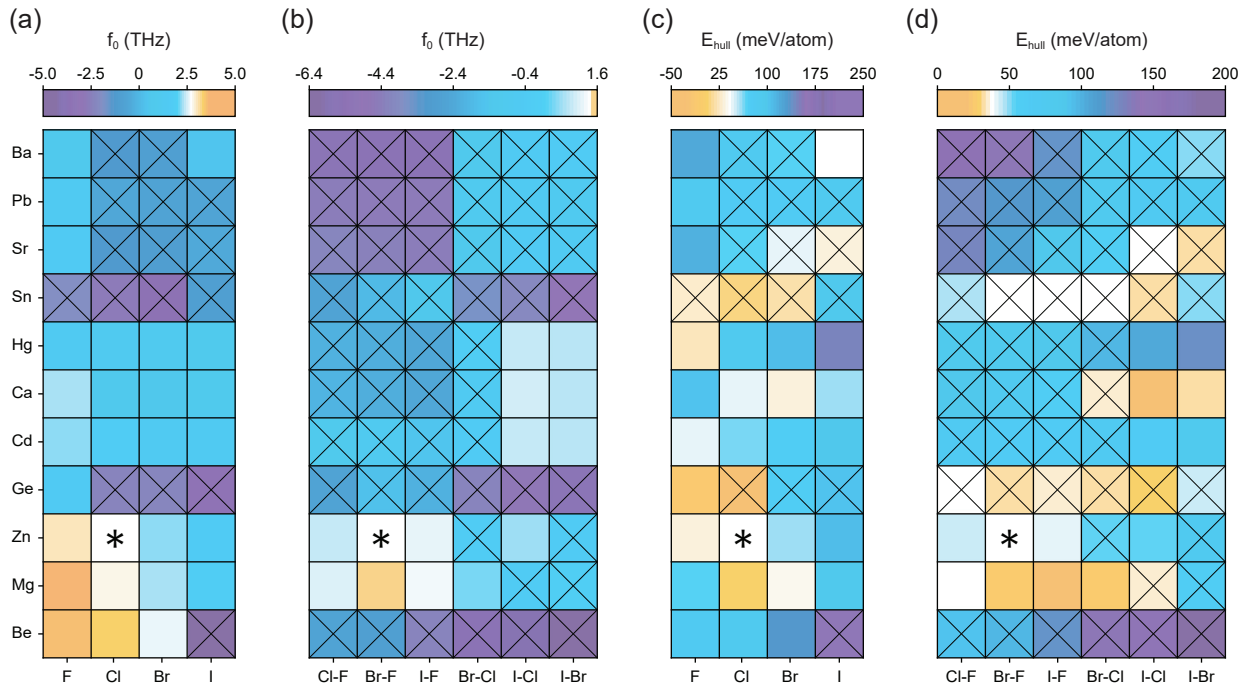

Figure 5.2: **Structural stability and thermodynamics of candidate compounds**. (a) Lowest optical phonon frequency for herbertsmithite-related candidates. (b) Lowest optical phonon frequency for Zn-barlowite-related candidates. (c) Convex hull energies for herbertsmithite-related candidates. (d) Convex hull energies for Zn-barlowite-related candidates. Structurally unstable compounds (identified by $f_0 < 0$) are denoted with an 'X'. Cations are shown on the vertical axis and anions on the horizontal axis, in order of increasing ionic radius from bottom to top and left to right, respectively. The reference compound (either herbertsmithite or Zn-barlowite) is shown in white and marked with an asterisk. Compounds with parameter values more favorable than the reference compounds are shown with warm colors, and values less favorable are shown with cool colors.

shown with warm colors.

Compounds containing larger cations are generally unstable, as well as Zn-barlowite relatives containing Be. Most compounds containing group IV elements (Ge, Sn, Pb) tend to be unstable, with the exception of $GeCu_3(OH)_6F_2$ and $PbCu_3(OH)_6F_2$. Group IV elements have two major oxidation states, 2+ and 4+. For Ge and Sn, the 4+ oxidation state is more stable. For heavier group IV elements such as Pb, the inert pair effect, where the force exerted on the outermost s electrons by the nucleus is stronger, the 2+ oxidation state is more stable since the s electrons are more difficult to ionize. Thus, while nearly all Pb containing compounds are unstable, they follow the expected trends based on cation size. Materials containing Ge and Sn, on the other hand, have more negative phonon frequencies than might be expected based on their size.

5.4 Pseudo Convex Hull Calculations

The convex hull of a compound is useful for determining if synthesis is thermodynamically feasible, usually through a comparison of the compound's formation energy to the sum of the energies of all other possible combinations of crystal structures that could be created from the same set of elements in the same ratios. Due to the prohibitive size of the phase space for our candidate materials, we perform a simplified procedure. Instead of considering all possible crystal structures, we consider only simple binary ionic compounds [e.g. $A(OH)_2$, AB_2], which are most likely to yield the lowest convex hull energies. Starting structures for these binary compounds were obtained from the Materials Project [201] and then re-relaxed with our settings.

For herbertsmithite-related compounds of the form $ACu_4(OH)_6B_2$ we considered two possible outcomes for the formation of simple binary compounds:

$$ACu_4(OH)_6B_2 \leftrightarrow AB_2 + [Cu(OH)_2]_3 \tag{5.1}$$

$$ACu_4(OH)_6B_2 \leftrightarrow A(OH)_2 + CuB_2 + [Cu(OH)_2]_2 \tag{5.2}$$

For Zn-barlowite-related compounds of the form $ACu_4(OH)_2BC$, we considered the following outcomes from the production of binary compounds:

$$ACu_4(OH)_6BC \leftrightarrow \frac{1}{2}AB_2 + \frac{1}{2}AC_2 + [Cu(OH)_2]_3 \tag{5.3}$$

$$ACu_4(OH)_6BC \leftrightarrow A(OH)_2 + \frac{1}{2}CuB_2 + \frac{1}{2}CuC_2\,[Cu(OH)_2]_2 \tag{5.4}$$

For each structural family, we sum the energies of the binary product compounds for the two scenarios above. Whichever reaction is lower in energy is subtracted from the energy of the compound itself and normalized by the number of atoms to calculation the energy above the hull (E_{hull}). While this method does not rule out the formation of stable polymorphs of the candidate compounds, it eliminates candidates for which the simple binary products are favored.

Insulators with energies less than ∼50 meV above the convex hull tend to be stable [202]. We therefore use an energy cutoff of 50 meV/atom as our criteria for thermodynamic stability when identifying candidate materials. The calculated energy above the hull for each compound is shown in Fig. 5.2(c,d). Energies higher than the reference compound are considered unfavorable and are represented with cool colors, while energies lower than the reference compound are favorable and represented with warm colors. Again, the reference compounds are shown in white and marked with an asterisk, and compounds with structural instabilities (as determined by phonon calculations) are

marked with an 'X'. There does not appear to be a clear connection between convex hull energy and structural stability or ion size.

Some compounds which show high thermodynamic stability may be structurally unstable, and some stable compounds may exhibit unfavorable thermodynamics. The convex hull energy depends not only on the candidate compound, but also on the energies of the binary and reference compounds. Certain materials maybe have highly unstable binary compounds, such that the relative stability of the final configuration is preferred, even though it is structurally unstable.

5.5 Structural Parameters

In addition to structural and thermodynamic stability, we use Cu-O-Cu bond angles and spacings between kagome layers as metrics to rank the candidate compounds. A Cu-O-Cu bond angle approaching 180° leads to a large antiferromagnetic superexchange interaction while minimizing undesirable Dzyaloshinskii–Moriya interactions. Larger bond angles are therefore highly desirable. A greater separation between the kagome layers isolates the two-dimensional magnetic subsystems and suppresses unwanted coupling between planes. In Fig. 5.3, these two structural properties are displayed for all candidate compounds. Squares corresponding to specific compounds are colored and marked according to the same system described for Fig. 5.2, where bond angles and interplane distances larger (smaller) than the reference compounds are favorable (unfavorable) and represented with warm (cool) colors, and structurally unstable compounds continue to be marked with an 'X'. Compounds with larger cation and anion radii generally lead to larger bond angles and interplane distances, but also tend to be structurally unstable. Ge and Sn substituted compounds tend to have smaller bond angles due to structural distortions of the hydroxyl groups surrounding the relatively unstable 2+ cation.

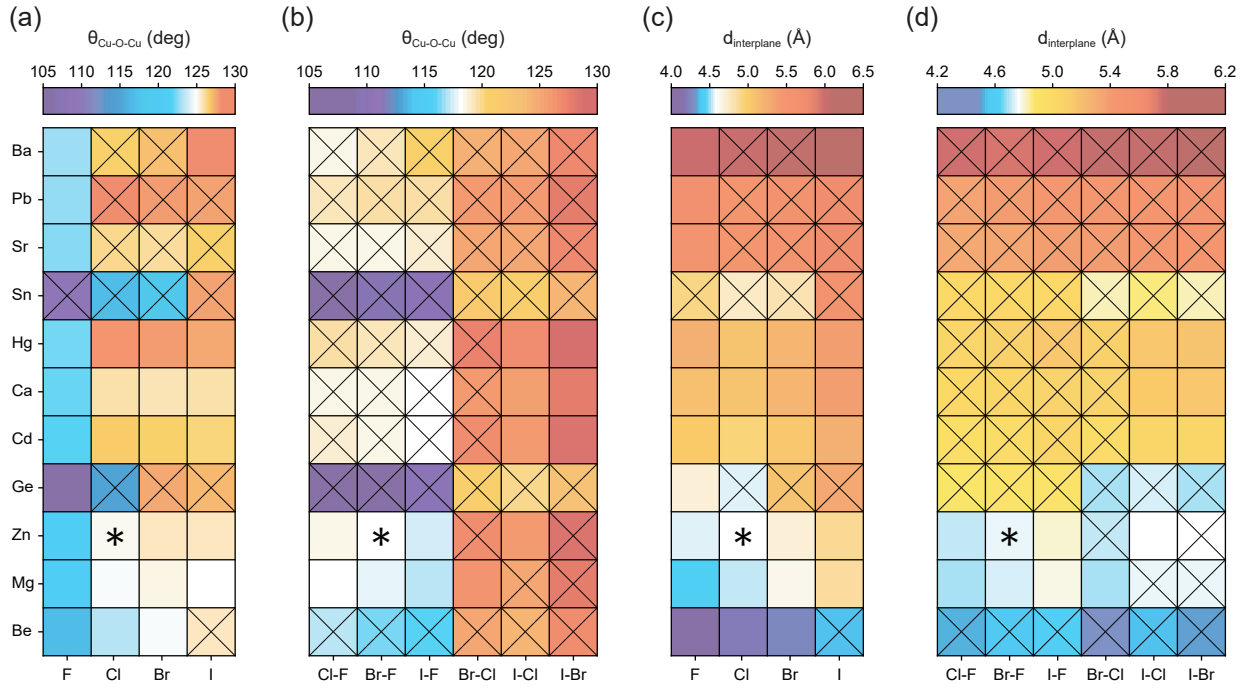

Figure 5.3: **Structural properties of candidate compounds.** (a) Cu-O-Cu bond angle for herbertsmithite-related candidates. (b) Cu-O-Cu bond angle for Zn-barlowite-related candidates. (c) Interplane kagome distance for herbertsmithite-related candidates. (d) Interplane kagome distance for Zn-barlowite-related candidates. Structurally unstable compounds are denoted with an 'X'. Cations are shown on the vertical axis and anions on the horizontal axis, in order of increasing ionic radius from bottom to top and left to right, respectively. The reference compound (either herbertsmithite or Zn-barlowite) is shown in white and marked with an asterisk. Compounds with parameter values more favorable than the reference compounds are shown with warm colors, and values less favorable are shown with cool colors.

5.6 Effects of Ion Size

We investigate the effects of ion size on the physical properties of the candidate compounds in more detail in Fig. 5.4. In Fig. 5.4(a), the Cu-O-Cu bond angle is plotted versus anion radius for the structurally stable materials. The anion size plotted on the horizontal axis for Zn-barlowite relatives refers to the *C*-site anion that occupies the same position as F in the reference compound $[ZnCu_3(OH)_6BrF]$ because it has the largest influence on bond angle. For all materials, bond angle increases with increasing anion size, and for a given anion, the bond angle also increases with increasing cation size.

Figure 5.4(b) shows the kagome plane spacing versus cation radius for stable compounds, with separate traces for each anion. As expected, a larger cation radius leads to greater distance between the kagome layers. For a given cation, interplane distance also increases with increasing anion size. In Fig. 5.4(c), we find that while the C-site anion has the greatest effect on the Cu-O-Cu bond angle, larger bond angles are obtained when the B-site anion is similar in size to the C-site anion.

We examine the effect of ion size on the lattice parameters of stable compounds in Fig. 5.4(d). The c-axis length primarily increases with cation size while the a-axis length primarily increases with anion size, although anion size has a much weaker affect on the a-axis than cation size does on the c-axis. The frequency of the lowest optical phonon mode (f_0) is plotted against c-axis length in Fig. 5.4(e) for both stable (filled markers) and unstable (empty markers) structures. Of all the structural parameters, the c-axis length has the highest correlation with f_0. For herbertsmithite relatives, as the c-axis increases, f_0 decreases, meaning compounds tend to be less dynamically stable. Of the compounds not containing Ge or Sn, c-axis lengths that are very small or very large lead to structural instabilities. Compounds containing group IV ions which are more stable in the 4+ oxidation state (Ge, Sn) are plotted in darker shades for both structural families because nearly all compounds containing these elements are unstable despite having intermediate c-axis lengths. Materials which contain cations from groups IIA and IIB which are close in size to Zn tend to be most stable. Fig. 5.4(f) shows Cu-O-Cu bond angle versus a-axis length. We find that a larger a-axis leads to a larger bond angle, which agrees with the results in Fig. 5.4(a), where bond angle is positively correlated with anion radius, and Fig. 5.4(d), which shows the positive correlation between anion size and the length of the a-axis. It should be noted that many unstable compounds containing Ge and Sn have much smaller bond angles than most other candidates due to the relative instability of the 2+ oxidation state as previously mentioned.

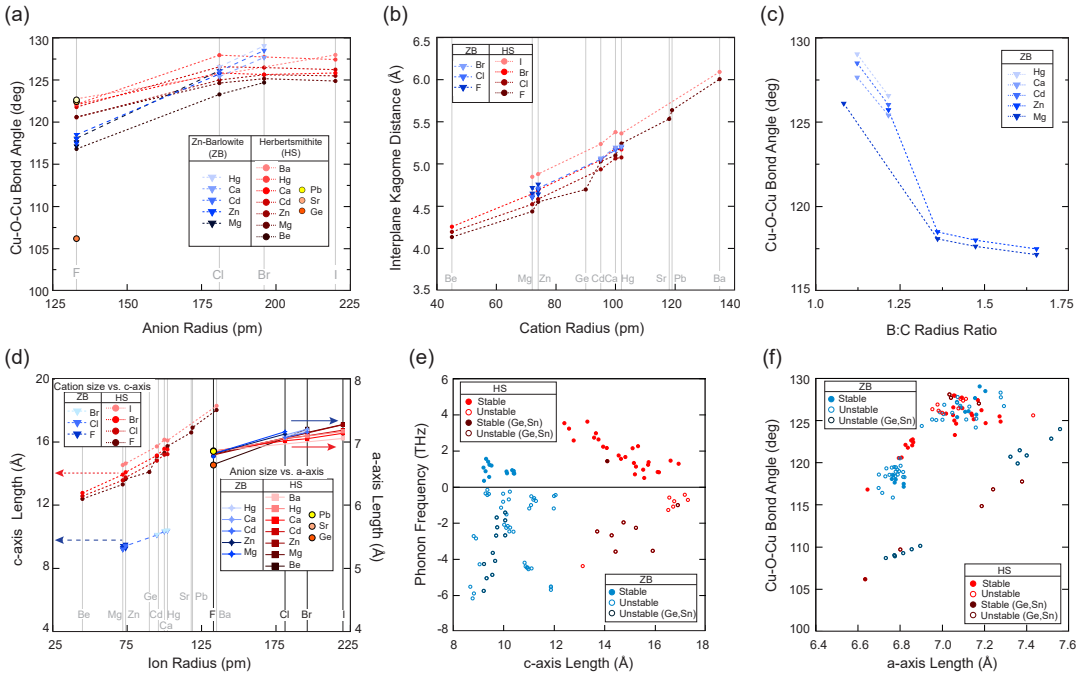

Figure 5.4: **Dependence of structural properties on ion size.** (a) Cu-O-Cu bond angle versus anion radius. For Zn-barlowite, the radius plotted is that of the most electronegative anion. Blue (red) traces correspond to Zn-barlowite (herbertsmithite) relatives. Different cations are plotted as separate traces where darker (lighter) traces correspond to smaller (larger) ion sizes. (b) Interplane kagome distance versus cation radius for herbertsmithite (red) and Zn-barlowite (blue) relatives. Separate traces are plotted for each anion, where small (large) anions are plotted in dark (light) shades. (c) Cu-O-Cu bond angle versus the anion B to anion C ratio for stable compounds. Separate traces are plotted for different cations. (d) c-axis length versus cation size (left, dashed line) and a-axis length versus anion size (right, solid lines). (e) Frequency of the lowest optical phonon mode versus c-axis length for Zn-barlowite (blue) and herbertsmithite (red) relatives. Stable (unstable) compounds are shown with filled (empty) markers. The group IV elements (Ge, Sn) which are less stable in the 2+ oxidation state are plotted with darker colors because they are almost always unstable, regardless of their c-axis length. (f) Cu-O-Cu bond angle versus a-axis length for Zn-barlowite (blue) and herbertsmithite (red) relatives. Stable (unstable) compounds are shown with filled (empty) markers. Compounds containing Ge and Sn cations (shown in darker colors) tend to have much smaller bond angles.

We also explored correlations between Cu-O-Cu bond angle, interplane distance, and in-plane Cu-Cu bond length. These correlations are plotted in Fig.5.5 The Cu-O-Cu bond angle has a weak positive correlation with interplane distance. There is also a positive correlation between in-plane Cu-Cu distance and Cu-O-Cu bond angle, as both are influenced by the length of the a-axis, which increases with increasing anion size. There is no obvious correlation between the interplane kagome distance and the in-plane Cu-Cu bond length, as the interplane distance depends mostly on cation size, and in-plane bond length depends on anion size.

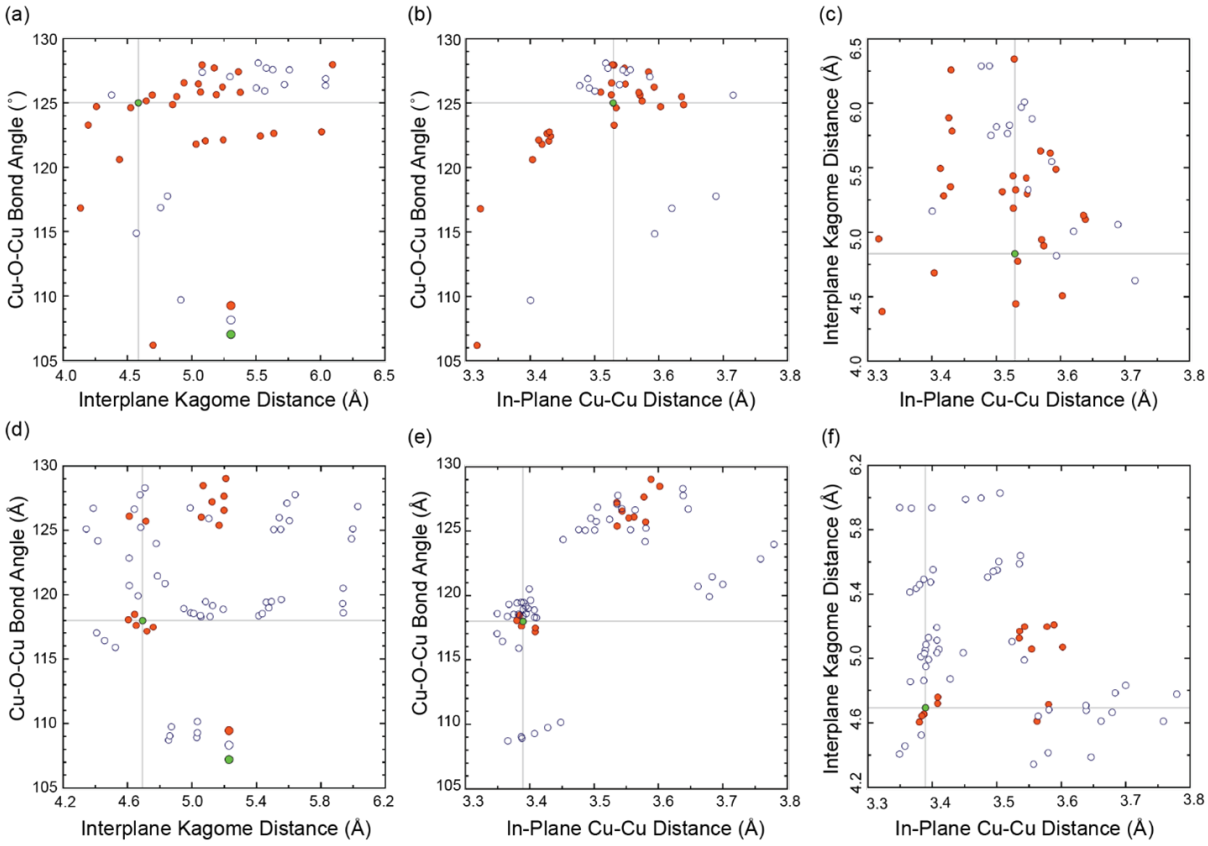

Figure 5.5: **Correlations between structural parameters.** (a) Cu-O-Cu bond angle vs. interplane kagome distance for herbertsmithite. (b) Cu-O-Cu bond angle vs. in-plane Cu-Cu distance for herbertsmithite. (c) Interplane kagome distance vs. in-plane Cu-Cu distance for herbertsmithite. (d) Cu-O-Cu bond angle vs. interplane kagome distance for Zn-barlowite. (e) Cu-O-Cu bond angle vs. in-plane Cu-Cu distance for Zn-barlowite. (f) Interplane kagome distance vs. in-plane Cu-Cu distance for Zn-barlowite.

Overall, for both structural families, compounds with cations of intermediate size (Mg, Zn, Cd, and Hg) are most stable. Compounds containing the group IV elements (Ge, Sn) are mostly unstable and have significantly smaller bond angles. Larger anions and cations lead to favorable structural properties, such as larger bond angles and interplane distances, but may also lead to distortions of the kagome layers or other structural instabilities. While the same general trends are present for both herbertsmithite and Zn-barlowite, some clusters of data for the Zn-barlowite have linear correlations of various properties since compounds with certain cations having linear dependencies with increasing anion size, as is explicitly shown in Fig.5.4.

5.7 Defect Formation

Herbertsmithite and Zn-barlowite are both susceptible to cation disorder. In herbertsmithite, the Jahn-Teller active d^9 Cu^{2+} ion occupies the tetragonally elongated site in the center of the CuO_4Cl_2 octahedra. The d^{10} Zn^{2+} ions are not Jahn-Teller active, and occupy the higher-symmetry trigonally compressed octahedral sites between the kagome layers. Due to the electronic configurations of the ions and distinct coordination environments, it is not favorable for Zn to occupy the in-plane sites within the kagome layer. However, herbertsmithite is the $x = 1$ end member of the Zn-paratacamite family $[Zn_xCu_{4-x}(OH)_6Cl_2]$, and there is a preference for some Cu to exist on the interlayer site instead of full occupation with Zn alone [166]. The equilibrium occupation of the interlayer site by Cu has been estimated to be as large as 15% in herbertsmithite [185, 186].

In Zn-barlowite, the interlayer site has a trigonal prismatic geometry, making it even less favorable for the Jahn-Teller active Cu^{2+} ion. As a result, the interlayer Cu occupation is only $\sim$5% in Zn-barlowite [192], confirming early computational predictions [190, 191]. Site-specific x-ray diffraction measurements have shown that there are

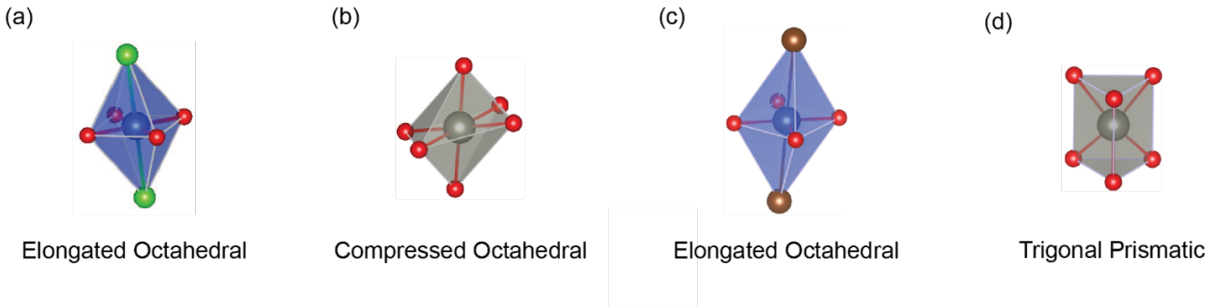

Figure 5.6: **Coordination geometry for cations in herbertsmithite and Zn-barlowite.** (a) The elongated $CuClO_2$ octahedral geometry for in-plane Cu ions in herbertsmithite. The Jahn-teller active cooper ion prefers this octahedral coordination geometry. (b) The compressed octahedral coordination geometry of interlayer Zn in herbertsmithite, which is unfavorable for the d^9 Cu ion. (c) The elongated $CuBrO_2$ octahedral coordination geometry of in-plane Cu in Zn-barlowite. (d) Trigonal prismatic geometry of interlayer Zn sites in Zn-barlowite, which are highly unfavorable for the Cu ions.

two distinct interlayer sites in Zn-barlowite: an off-center C_{2v} site and a central D_{3h} site. The interlayer Cu defects occupy the C_{2v} sites. In barlowite $[Cu_4(OH)_6Cl_2]$ a magnetic transition is observed at $T_N = 15$ K, where the bulk magnetic moment comes from the interlayer Cu spins. It should be noted that even for large concentrations of Cu ions on the interlayer site, Zn-barlowite does not show signs of magnetic ordering, indicating that the possible QSL phase is somewhat robust against interlayer magnetic impurities [192].

In order to determine the tendency towards disorder for our best candidate compounds, we calculated the formation energy for interlayer defects. We did not consider defects within the kagome layer as these are known to be much higher in energy (and are therefore not observed experimentally) due to the difference of coordination geometry of in-plane and interlayer sites. The coordination geometries are shown in Fig.5.6 for herbertsmithite and Zn-barlowite.

The defect formation energy consists of the total energy difference between the perfectly ordered bulk structure, and the structure with a defect, as well as the chemical potential difference from replacing a metal ion with a Cu ion.

$$M_8Cu_{24}(OH)_{48}(BC)_8 + Cu^{2+} \leftrightarrow M_7Cu_{25}(OH)_{48}(BC)_8 + M^{2+} \tag{5.5}$$

$$\Delta E_d^f = (E_{inter} + \mu_M) - (E_{bulk} + \mu_{Cu}) \tag{5.6}$$

$$\Delta E_d^f = (E_{inter} - (E_{bulk})(\mu_M^{2+} - \mu_{Cu}) \tag{5.7}$$

$$\Delta E_d^f = \Delta E_s + \Delta\mu \tag{5.8}$$

The individual components of ΔE_d^f are shown in Tab.5.1 for herbertsmithite-related compounds and Tab.5.2 for Zn-barlowite-related compounds.

Table 5.1: Components of ΔE_d^f for herbertsmithite-related compounds.

Compound	ΔE_s (eV)	$\Delta\mu$ (eV)	Δ_d^f (eV)
$BaCu_3(OH)_6I_2$	5.40	-2.98	2.42
$CaCu_3(OH)_6I_2$	4.34	-3.48	0.87
$CaCu_3(OH)_6Cl_2$	4.12	-3.55	0.57
$MgCu_3(OH)_6Br_2$	2.77	-2.40	0.36
$ZnCu_3(OH)_6Cl_2$	-0.57	0.70	0.13

Table 5.2: Components of ΔE_d^f for Zn-Barlowite-related compounds.

Compound	ΔE_s (eV)	$\Delta\mu$ (eV)	Δ_d^f (eV)
$CaCu_3(OH)_6IBr$	4.31	-3.57	0.74
$CaCu_3(OH)_6ICl$	4.25	-3.52	0.72
$MgCu_3(OH)_6BrCl$	2.62	-2.32	0.30
$MgCu_3(OH)_6ClF$	2.79	-2.40	0.39
$ZnCu_3(OH)_6BrF$	-0.60	0.70	0.10
$ZnCu_3(OH)_6ClF$	-0.62	0.69	0.70

An ideal QSL candidate will have only non-magnetic ions on the interlayer sites, and therefore must have a high energy cost for interlayer Cu substitution. We calculated the formation energy of such defects in a select number of our most promising candidates (those structurally stable, with $E_{\text{hull}} < 50$ meV/atom, and with bond angles and inter-plane distances larger than the reference compounds). Since nearly all experimental and

computational studies indicate that there is negligible substitution of non-magnetic ions within the kagome layers, we consider only interlayer defects. The general expression for the formation energy of a charge-neutral substitutional defect is

$$E_d^f = E[\text{defect}] - E[\text{bulk}] + (\mu_A - \mu_{\text{Cu}}) = \Delta E_s + \Delta\mu,$$

where ΔE_s is the difference in energy between a structure with a single defect and the pristine bulk structure and $\Delta\mu$ is the chemical potential difference of A and Cu. To calculate E[defect], we construct defect structures from $2 \times 2 \times 2$ supercells of herbertsmithite relatives and $2 \times 2 \times 1$ supercells of Zn-barlowite relatives, with a single Cu substitution. We relax the atomic positions of the defect structures shown in Fig.5.7 and subtract the energy of the original defect-free structure to obtain ΔE_s.

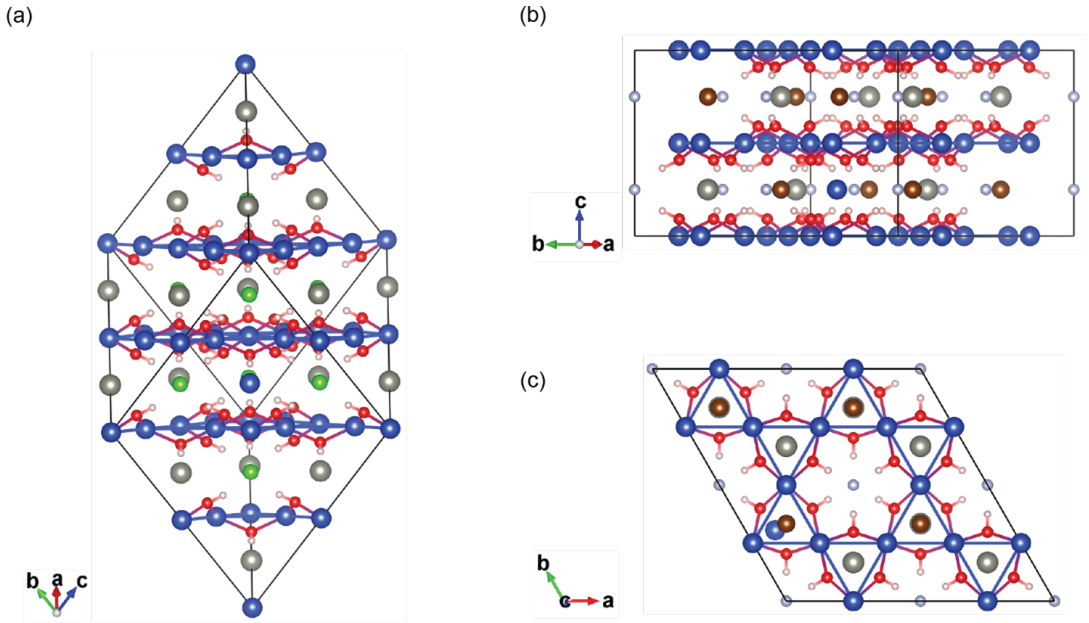

Figure 5.7: **Defect supercell structures.** (a) A single copper defect occupies an interlayer Zn site in a $2 \times 2 \times 2$ herbertsmithite supercell. (b) Side-view of a $2 \times 2 \times 1$ Zn-barlowite supercell where a Cu defect occupies an interlayer off-center C_{2v} site. (c) Top-view of a $2 \times 2 \times 1$ Zn-barlowite supercell where a Cu defect occupies an interlayer off-center C_{2v} site.

The chemical formulas for the defect-containing and defect-free configurations are not equivalent, so the chemical potential difference $\Delta\mu = \mu_A - \mu_{\mathrm{Cu}}$ must be considered. Interlayer defects are primarily created during the initial growth of the material. During synthesis of $A\mathrm{Cu_3(OH)_6}B_2$, the chemical potentials of the constituent elements must satisfy the inequality

$$\mu_A + 3\mu_{\mathrm{Cu}} + 6\mu_{\mathrm{OH}} + 2\mu_B > E[A\mathrm{Cu_3(OH)_6}B_2].$$

Individual chemical potentials must all be less than zero ($\mu_A < 0$, $\mu_B < 0$, $\mu_{\mathrm{OH}} < 0$, and $\mu_{\mathrm{Cu}} < 0$). Additionally, the formation of unwanted side products must be avoided, imposing the additional inequalities

$$\mu_A + 2\mu_B < E[AB_2],$$

$$\mu_{\mathrm{Cu}} + 2\mu_B < E[\mathrm{Cu}B_2],$$

$$\mu_A + 2\mu_{\mathrm{OH}} < E[A(\mathrm{OH})_2].$$

Similar inequality constraints exist for $A\mathrm{Cu_3(OH)_6}BC$. A higher defect formation energy is preferable to minimize disorder. To maximize E_d^f, we must maximize the chemical potential difference $\Delta\mu$ subject to the above inequality constraints. The defect formation energies calculated with these optimal values of $\Delta\mu$ are given in Table 5.3. All candidate compounds investigated had a higher energy cost for interlayer defects than herbertsmithite and Zn-barlowite except $\mathrm{ZnCu_3(OH)_6ClF}$ (Zn-substituted claringbullite).

Two previous computational studies investigated doping selectivity in barlowite [190, 191]. In both cases, the authors investigated the likelihood of substituting various nonmagnetic ions into the interlayer and intralayer sites of barlowite, in contrast to the

present work where we examine the energy cost of a Cu defect on an interlayer site in fully-substituted A-barlowite (A = Zn, Mg, Ca). Despite differences in the methodology used to construct defect structures and calculate the chemical potential differences, our findings are generally consistent with those studies, which suggested Zn and Mg to be the most favorable ions for synthesizing barlowite-related compounds.

5.8 Phonon Dispersions

After eliminating all compounds with structural instabilities at the Γ point, formation energies greater than 50 meV/atom above the convex hull, and Cu-O-Cu bond angles smaller than the reference compounds, 9 candidate materials remained. For these candidates, we calculated the defect formation energy E_d^f. To determine a final ranking, we used the following criteria:

1. Structural stability ($f_0 > 0$)
2. Convex hull energy ($\mathrm{E_{hull}} < 50$ meV/atom)
3. Defect energy cost ($E_d^f[\text{candidate}] > E_d^f[\text{ref}]$)
4. Cu-O-Cu bond angle ($\theta > \theta^{\text{ref}}$)

All compounds satisfying these criteria are listed with their associated properties in Table 5.3. For these final candidates, we verified structural stability by calculating the full phonon dispersion throughout the entire Brillouin zone using the finite displacement method within the PHONOPY code [103]. Such calculations can identify structural instabilities associated with an enlargement of the unit cell. Dispersion curves were calculated for all candidates in Table 5.3. However, only one compound in the herbertsmithite family and two compounds in the Zn-barlowite family were found to be stable throughout the entire Brillouin zone. The dispersion curves of these compounds are shown in Fig. 5.8.

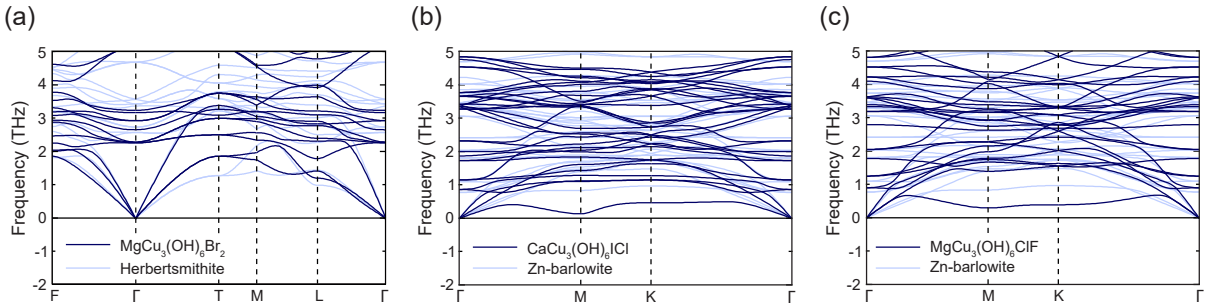

Figure 5.8: **Phonon dispersions of final candidates.** (a) The phonon dispersion for $MgCu_3(OH)_6Br_2$ (blue) overlaid with the reference dispersion for herbertsmithite (gray). (b) The phonon dispersion for $CaCu_3(OH)_6ICl$ (blue) overlaid with the reference dispersion for Zn-barlowite (gray). (c) The phonon dispersion for $MgCu_3(OH)_6ClF$ (blue) overlaid with the reference dispersion for Zn-barlowite (gray). The absence of imaginary phonon frequencies in all three cases confirms the structural stability of these candidate compounds.

The dispersions with imaginary modes for herbertsmithite-related compounds in Tab.5.3 are shown in Fig.5.9, the eigenvectors for the imaginary modes are shown in Fig.5.10. Dispersions with imaginary modes and the eigenvectors of the structural instabilities for Zn-barlowite-related compounds are shown in Fig.5.11 and Fig.5.12, respectively.

Surprisingly, while Zn-claringbullite [$ZnCu_3(OH)_6ClF$] is known to have perfect kagome layers at room temperature [199], our ground state dispersion shows instabilities at the M and K points (see Fig.5.11). The instabilities we observe in DFT may be avoided by thermal fluctuations at room temperature, which could explain the discrepancy between our calculations and the experimental results. Two other Zn-barlowite-related candidate compounds listed in Table 5.3, $CaCu_3(OH)_6IBr$ and $MgCu_3(OH)_6BrF$, showed similar instabilities (see Fig.5.12, and therefore may also be stable at room temperature.

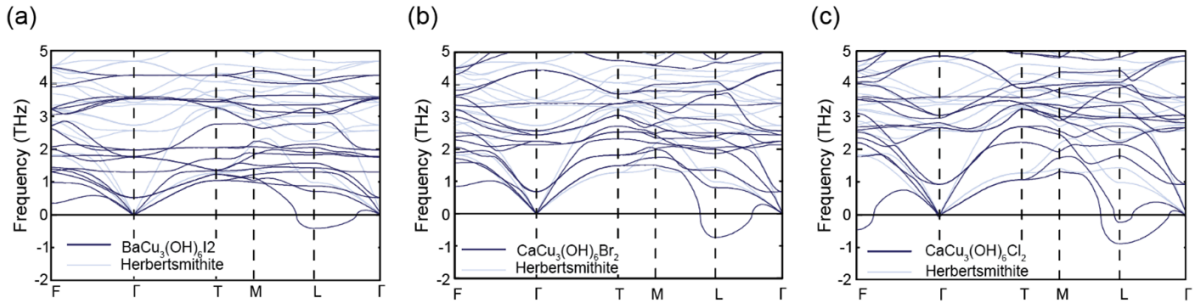

Figure 5.9: **Herbertsmithite imaginary phonon frequencies.** (a) Phonon dispersion for $BaCu_3(OH)_6I_2$ (blue) overlaid with the dispersion for herbertsmithite (gray) An instability is observed at the L point. (b) Phonon dispersion for $CaCu_3(OH)_6Br_2$ (blue) overlaid with the dispersion for herbertsmithite (gray). Instabilities are observed at the L point. (c) Phonon dispersion for $CaCu_3(OH)_6Cl_2$ (blue) overlaid with the dispersion for Zn-Barlowite (gray). Instabilities are observed at the F and L points.

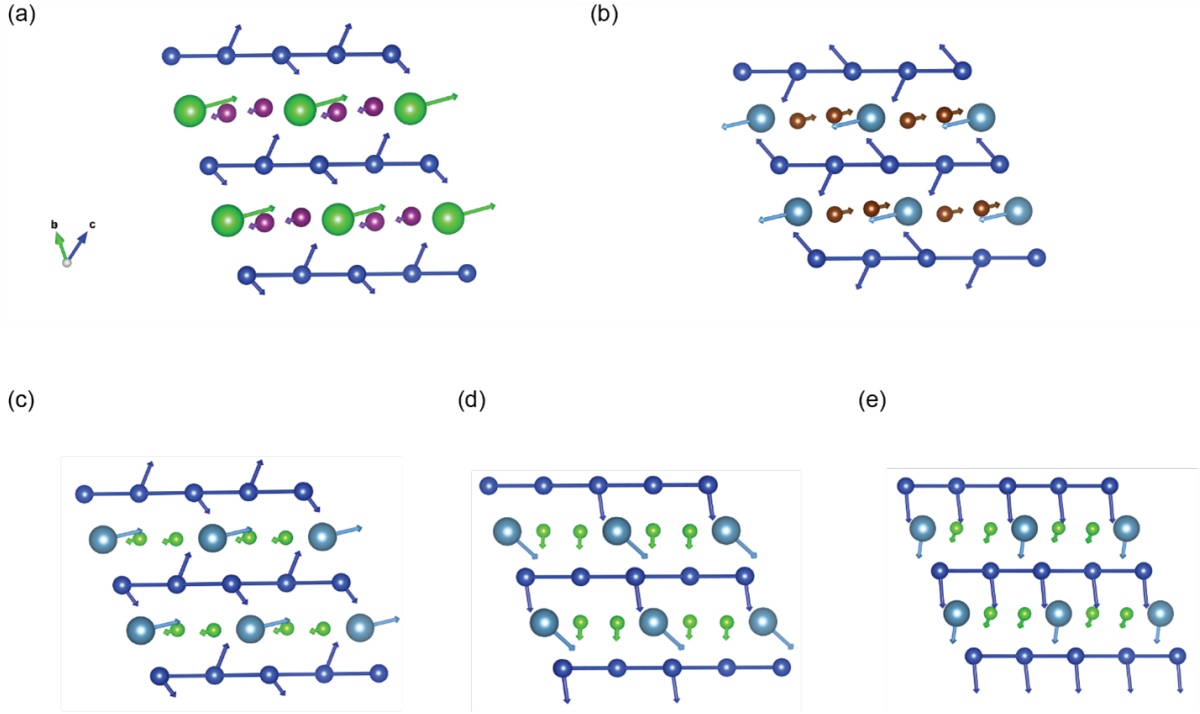

Figure 5.10: **Eigenvectors for imaginary frequencies herbertsmithite.** (a) Eigenvector for the instability at the L-point for $BaCu_3(OH)_6I2$. The coordinate compass in the lower left of panel (a) is the same for all eigenvectors (a-e). (b) Eigenvector for the instability at the L-point for $CaCu_3(OH)_6Br_2$. (c) Eigenvector for lowest frequency instability at the L-point for $CaCu_3(OH)_6Cl_2$. (d) Eigenvector for higher frequency instability at the L-point for $CaCu_3(OH)_6Cl_2$. (e) Eigenvector for the instability at the F-point for $CaCu_3(OH)_6Br_2$.

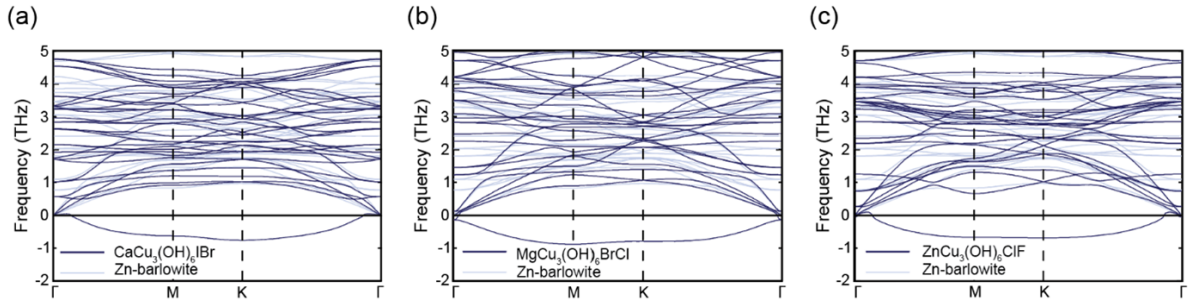

Figure 5.11: **Imaginary frequencies for Zn Barlowite Candidates.** (a) Phonon dispersion for $CaCu_3(OH)_6IBr$ (blue) overlaid with the dispersion for Zn-barlowite (gray). Instabilities are observed at the M and K points. (b) Phonon dispersion for $MgCu_3(OH)_6BrCl$ (blue) overlaid with the dispersion for Zn-barlowite (gray). Instabilities are observed at the M, K, and Γ points. (c) Phonon dispersion for $ZnCu_3(OH)_6ClF$ (blue) overlaid with the dispersion for Zn-barlowite (gray). Instabilities are observed at the M and K points.

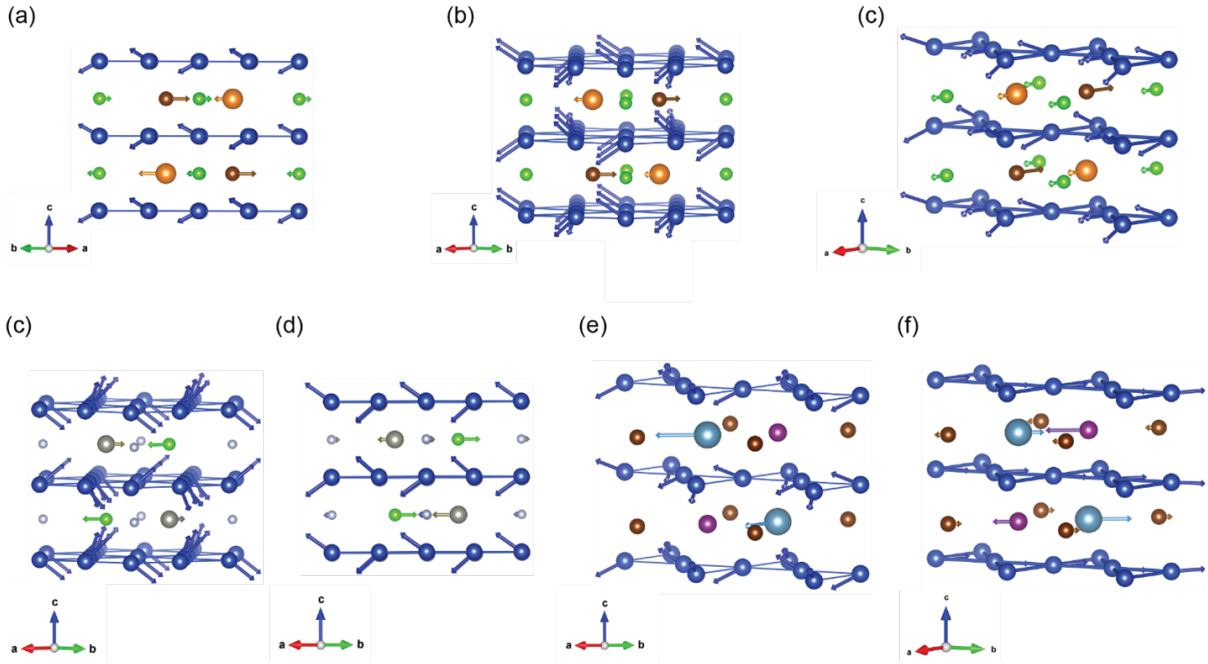

Figure 5.12: **Eigenvectors for imaginary frequencies Zn-barlowite.** (a) Eigenvector for the instability at the K-point for $MgCu_3(OH)_6BrCl$. (b) Eigenvector for the instability at the M-point for $MgCu_3(OH)_6BrCl$. (c) Eigenvector for instability at the Γ-point for $MgCu_3(OH)_6BrCl$. (d) Eigenvector for higher frequency instability at the M-point for $ZnCu_3(OH)_6ClF$. (e) Eigenvector for higher frequency instability at the K-point for $ZnCu_3(OH)_6ClF$. (f) Eigenvector for the instability at the M-point for $CaCu_3(OH)_6IBr$. (g) Eigenvector for the instability at the K-point for $CaCu_3(OH)_6IBr$.

5.9 Determining Final Candidates

Our calculations identify $MgCu_3(OH)_6Br_2$ as a potential candidate within the herbertsmithite family, as well as $CaCu_3(OH)_6ICl$ and $MgCu_3(OH)_6ClF$ in the Zn-barlowite family. However, some practical considerations related to synthesis may require further investigation.

Table 5.3: Properties of the most promising QSL candidate materials as compared to the reference materials. The references (herbertsmithite and Zn-barlowite) are highlighted in gray, and the final candidates (with no instabilities throughout the Brillouin zone) are marked with asterisks.

Compound	f_0 (THz)	E_{hull} (meV/atom)	E_d^f (eV)	θ (deg)	d_{inter} (Å)	d_{in} (Å)
$BaCu_3(OH)_6I_2$	0.41	42.6	2.42	128.0	6.09	3.53
$CaCu_3(OH)_6Br_2$	0.50	30.7	0.87	125.7	5.19	3.53
$CaCu_3(OH)_6Cl_2$	0.70	44.8	0.57	125.8	5.06	3.51
$MgCu_3(OH)_6Br_2$ *	2.23	36.0	0.36	125.2	4.65	3.57
$ZnCu_3(OH)_6Cl_2$	2.63	41.2	0.13	125.0	4.58	3.53
$CaCu_3(OH)_6IBr$	0.77	31.6	0.74	127.7	5.20	3.58
$CaCu_3(OH)_6ICl$ *	0.94	19.2	0.72	125.4	5.17	3.54
$MgCu_3(OH)_6ClF$ *	1.09	39.6	0.39	118.1	4.60	3.38
$MgCu_3(OH)_6BrCl$	0.35	26.9	0.30	126.1	4.61	3.56
$ZnCu_3(OH)_6BrF$	1.41	38.6	0.10	118.0	4.69	3.39
$ZnCu_3(OH)_6ClF$	0.89	43.1	0.07	118.5	4.64	3.38

For instance, the Mg analog of Zn-barlowite [$MgCu_3(OH)_6BrF$] has not been synthesized due to the insolubility of MgF_2 in water. While synthesis of Zn-barlowite using NH_4F yields a structurally equivalent compound, crystals obtained using this method show a similar magnetic transition to barlowite, suggesting possible differences in defect structures between the two synthesis methods [203]. The insolubility of MgF_2 may therefore present difficulty in synthesizing our candidate $MgCu_3(OH)_6ClF$ [199]. Synthesis of $MgCu_3(OH)_6Br_2$ has been attempted, but the desired product was a Zn-barlowite analog [200]. The synthesis method, which followed the typical hydrothermal procedure, resulted in a compound with $P\bar{3}m1$ symmetry, which may mean that the herbertsmithite

$R\bar{3}m$ structure is not favored in this reaction. It is possible that other synthesis methods could yield different results. To our knowledge, no experimental studies have been performed on the Ca analog of either herbertsmithite or Zn-barlowite, nor any related compounds containing I.

In summary, we performed a systematic combinatorial exploration of herbertsmithite and Zn-barlowite material relatives and identified those with properties that may enhance the likelihood of an ideal QSL ground state. We found several promising candidates—$MgCu_3(OH)_6Br_2$, $CaCu_3(OH)_6ICl$, and $MgCu_3(OH)_6ClF$—that are structurally stable, thermodynamically feasible to synthesize, have high energy costs for interlayer defects, and whose structural properties may result in antiferromagnetic superexchange interactions stronger than herbertsmithite or Zn-barlowite. These compounds, if they can be synthesized, may prove to be better QSL candidates than their well-studied counterparts.

Chapter 6

Characterizing the Nature of Charge Density Wave order in CsV_3Sb_5

[1]Kagome metals are intriguing due to their ability to host topologically nontrivial electronic states. Single orbital tight-binding models yield Dirac points and a flat band which can give rise to nontrivial band topology and strong electron correlations [205, 206, 207, 208, 209, 210, 211, 212]. These unique electronic structures enable the possibility for charge density waves, superconductivity, and charge fractionalization. The recently discovered family of AV_3Sb_5 (A = K, Cs, Rb) kagome metals provides a platform to study a unique combination of interconnected material properties, where an unusual charge density wave (CDW) transition is measured at $T_{CDW} = 78, 102, 94$ K [213, 214, 215] followed by a superconducting transition at $T_C = 0.93, 0.92, 2.5$ K [216] for A = K, Rb, Cs respectively.

The high-temperature crystal structure of CsV_3Sb_5 viewed along the c-axis is shown

[1]The contents of this chapter are adapted from [204]: "Coherent phonon spectroscopy and interlayer modulation of charge density wave order in the kagome metal CsV_3Sb_5," Noah Ratcliff, Lily Hallett, Brenden R. Ortiz, Stephen D. Wilson, and John W. Harter, *Physical Review Materials*, 5, (2021): L111801.

in Fig.6.1(a). Vanadium atoms form a kagome lattice with a bond length 2.75 Å, with antimony atoms positioned above and below the 2D kagome plane. The layered nature of the structure means the material can be easily cleaved, making experimental measurements convenient. Diffraction measurements have observed charge order with a $q = (0.5, 0.5)$ wave vector in KV_3Sb_5 and CsV_3Sb_5 corresponding to 3Q CDW order. Candidate distortions leading to such order are the Star of David or inverse Star of David distortions are shown in Fig.6.1(b,c). At lower temperatures, unidirectional charge stripe order appears to coexist with the 3Q CDW state, connecting the underlying interactions to stripe/nematic instabilities within a kagome network [216].

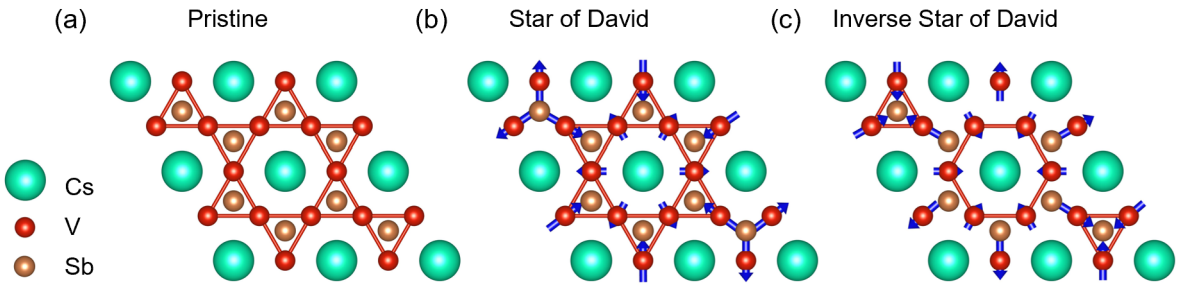

Figure 6.1: **Distortions of the kagome Lattice**. (a) Pristine kagome lattice viewed along the c-axis (b) Star of David (SoD) distortion (breathing out) (c) Inverse Start of David distortion (breathing in). Figure adpated from [216].

Experiments have revealed many interesting properties, including the giant anomalous Hall effect [217, 218], chiral charge order [219], and proximity to a time-reversal symmetry-breaking instability in the absence of magnetic moments [213, 220], thermodynamic signatures of nodal quasiparticles [221], multiple superconducting domes [222, 223, 224], spin-triplet supercurrents [223], and zero-bias conductance peaks inside superconducting vortex cores [225] have all been observed. This combination of properties, in addition to the fact that the charge density wave instability seemingly competes with superconductivity, suggests the formation of an unconventional and potentially topological superconducting state. However, the microscopic origin of the charge

density wave is still an open question.

We address two important questions in our work. The first is whether or not the CDW modulates along the c-axis [225, 216, 226], and the second involves reports of uniaxial CDW order which onsets lower than the initial CDW transition [225, 227, 222, 228]. We use a combination of ultrafast coherent phonon spectroscopy and first-principles density functional theory calculations to investigate the charge density wave order in CsV_3Sb_5. We demonstrate that there is modulation of the CDW along the c-axis which we attribute to the simultaneous condensation of one M and two L point modes. We refer to this as the "MLL" distortion, which breaks C_6 rotational symmetry and therefore could provide an explanation for the uniaxial order observed at low temperatures.

6.1 Coherent Phonon Spectroscopy

Single crystals of CsV_3Sb_5 were synthesized according to the methodology outlined in [213]. Samples were mounted in an optical cryostat and time-resolved optical reflectivity measurements were performed on freshly cleaved surfaces. A non-collinear optical parametric amplifier was used to generate $\sim$ 50 fs signal (800 nm) and idler (1515 nm) pulses at a repetition rate of 500 kHz, which were used as probe and pump beams, respectively. Both pulses had a low fluence of $\sim 100\ \mu J/cm^2$ to avoid sample heating and were linearly polarized in-plane. A lock-in amplifier and optical chopper were used to measure the small pump-induced transient change in reflectivity. Raw transient reflectivity data measured at several temperatures is shown in Fig.6.2. Above T_{CDW}, the reflectivity increases after the pump pulse and shows oscillations at a single phonon frequency. Below T_{CDW}, the reflectivity decreases and shows a complex beat pattern, indicating that multiple oscillation frequencies are present. The clear difference in the transient optical response across the CDW phase transition ($\Delta R/R > 0$ above T_{CDW}, $\Delta R/R < 0$ below

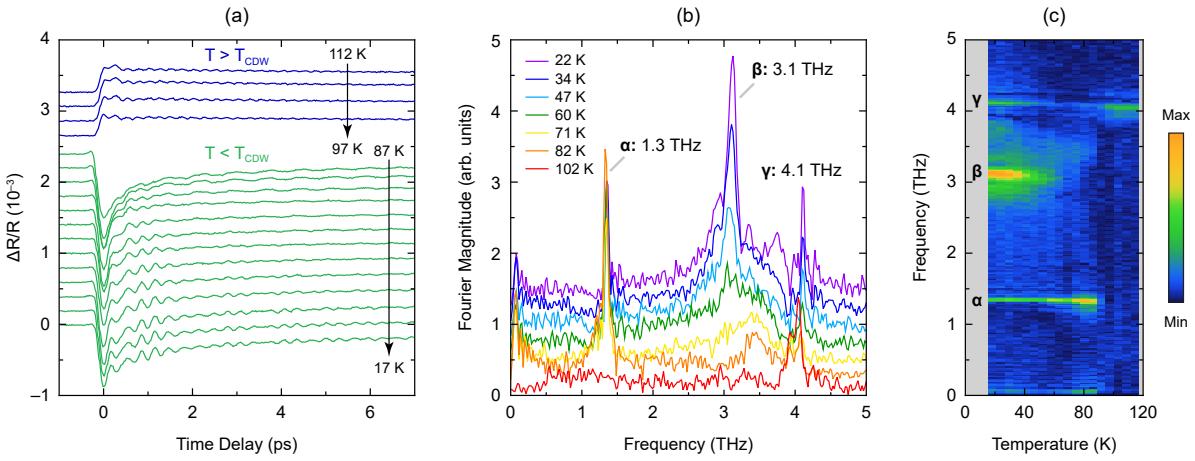

Figure 6.2: Coherent phonon spectroscopy data for CsV_3Sb_5. (a) Transient reflectivity curves for a series of temperatures above and below the CDW phase transition. Temperatures are approximately evenly spaced and scans are offset for clarity. Above T_{CDW}, the reflectivity increases after the pump pulse and a single oscillation frequency is apparent. Below T_{CDW}, in contrast, the reflectivity decreases after the pump pulse and the presence of multiple oscillation frequencies results in a complex beat pattern. (b) Magnitude of the Fourier transform of the reflectivity oscillations after subtraction of a double exponential background. Curves are offset for clarity. Three resonances are identified and labeled α (1.3 THz), β (3.1 THz), and γ (4.1 THz). (c) Two-dimensional temperature-frequency map of the Fourier magnitude of the coherent phonon oscillations. While γ is present at all temperatures, α only becomes active below T_{CDW}. Below $T^* \approx 60$ K, the broad β resonance appears and gradually grows in amplitude. A weak softening of all three frequencies is apparent with increasing temperature.

T_{CDW}) is likely due to the opening of a partial energy gap near the Fermi level at the CDW phase transition [229] and related changes in the density of states. The sign of $\Delta R/R$ is sensitive to electronic parameters influencing carrier dynamics, such as band filling and band gap renormalization [230]; therefore, qualitative changes in the transient optical response are expected at T_{CDW}.

To gain a better understanding of the coherent phonon oscillations, a double exponential background ($A_0 + A_1 e^{-t/\tau_1} + A_2 e^{-t/\tau_2}$) is fitted and then subtracted from the reflectivity curves after $t = 100$ fs. The remaining oscillations are Fourier transformed and plotted in Fig. 6.2(b). There are three resonance modes present in the material: α at 1.3 THz, β at 3.1 THz, and γ at 4.1 THz. No other frequencies are detected up to 10 THz. The two dimensional temperature-frequency map of the oscillation spectrum is shown in Fig.6.2c, where the temperature dependence of the phonon oscillations can be seen more clearly.

The γ mode (4.1 THz) is present at all temperatures, but the α mode (1.3 THz) shows a sudden, intense appearance at $T \approx 92$ K, close to $T_{CDW} = 94$ K determined through independent heat capacity measurements [213]. Therefore, we identify this mode with the CDW transition temperature. The slightly lower detection temperature is likely due to the modest local heating of the sample by the laser. Below $T^* \approx 60$ K, the broad β mode (3.1 THz) appears. All three resonances show a weak frequency softening as temperature is increased, but none of the modes show evidence of complete softening ($\omega \to 0$).

6.2 Phonon Dispersions

DFT calculations were performed to explain the experimental observations. Phonon frequencies were calculated using DFT within the Perdew-Burke-Ernzerhof generalized

gradient approximation, as implemented in the Vienna ab initio Simulation Package (VASP) [99]. The projector augmented wave potentials considered 9 valence electrons for the cesium atoms, the plane wave basis cutoff energy was 300 eV, and the zero damping DFT-D3 van der Waals correction was employed. The unit cell structure was relaxed using a Γ-centered 18 × 18 × 12 k-point mesh. The relaxed lattice parameters were $a = b = 5.450$ Å and $c = 9.297$ Å and the out-of-plane antimony atoms were located at fractional height $z = 0.7435$. Phonon dispersion relations were calculated with the PHONOPY software package [103] via the finite displacement method using a $3 \times 3 \times 2$ supercell. A $2 \times 2 \times 2$ supercell was used to calculate the energies of modes simultaneously condensing at the M and L points.

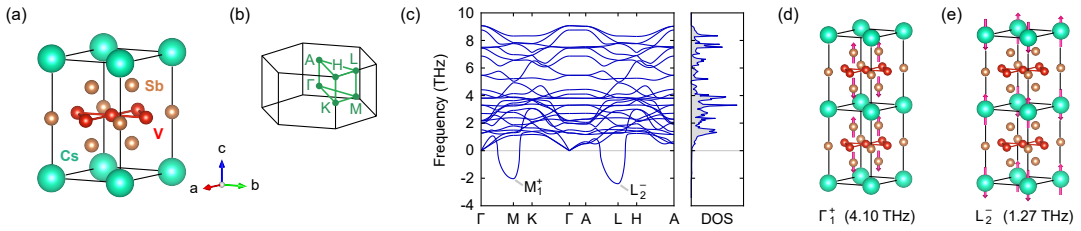

Figure 6.3: **First-principles phonon calculations.** (a) Unit cell for CsV_3Sb_5.The vanadium atoms (red) form a perfect kagome net and are coordinated with in-plane and out-of-plane antimony atoms. (b) First Brillouin zone of the hexagonal lattice, with high-symmetry points labeled. (c) Calculated phonon dispersion relations. There are two unstable modes with imaginary frequencies: one at the M point with irreducible representation M_1^+, and the other at the L point with irreducible representation L_2^-. Right panel shows the phonon density of states. (d) Illustration of the fully symmetric Γ_1^+ phonon at 4.10 THz experimentally detected at all temperatures. (e) Illustration of the L_2^- phonon at 1.27 THz experimentally detected below T_{CDW}.

Phonon frequencies were calculated for the CsV_3Sb_5 in the $P6/mmm$ crystal structure shown in Figure 6.3(a). The first Brillouin zone is depicted in 6.3(b), showing the M-point at $k_z = 0$, which connects the saddle points in the band structure and is associated with the nesting-driven Peirels-like instability [213], as well as the L point with $k_z = \pi/c$. Tab.6.1, lists all the calculated phonon frequencies up to 5 THz. The full phonon dispersion is shown in Fig.6.3c where there are two instabilities, one at the M point

Table 6.1: Calculated phonon frequencies up to 5 THz.

Γ point		M point		L point	
Irrep	f (THz)	Irrep	f (THz)	Irrep	f (THz)
Γ_6^-	1.28	M_1^+	−2.03	L_2^-	−2.40
Γ_2^-	1.51	M_2^-	1.11	L_2^-	1.27
Γ_6^-	1.99	M_3^-	1.30	L_3^-	1.30
Γ_4^-	2.16	M_3^+	1.33	L_4^-	1.43
Γ_6^+	2.19	M_4^-	1.49	L_4^-	1.52
Γ_2^-	2.70	M_2^+	1.79	L_1^-	1.78
Γ_5^-	3.30	M_2^-	1.88	L_1^+	1.84
Γ_5^+	3.81	M_1^-	2.39	L_2^+	2.39
Γ_1^+	4.10	M_2^-	2.78	L_1^+	2.76
Γ_3^+	4.42	M_4^-	2.92	L_3^+	2.90
		M_4^+	3.24	L_3^-	3.27
		M_3^-	3.32	L_4^+	3.29
		M_3^+	3.46	L_4^-	3.52
		M_1^+	3.63	L_2^-	3.67
		M_2^-	3.85	L_1^+	3.84
		M_4^-	3.89	L_3^+	3.87
		M_3^-	4.14	L_4^+	4.12
		M_4^-	4.93	L_3^+	4.92
				L_2^-	4.98

and one at the L point, with irreducible representations M_1^+ and L_2^-, respectively, in the notation of Miller and Love. The L point instability has a slightly larger imaginary frequency.

6.3 Frozen Phonon Calculations

As discussed in the introduction, condensation of three equivalent M-point modes leads to a fully symmetric breathing mode, the two possible configurations being the "Star-of-David" (breathing out), or "inverse star-of-David" (breathing in) [216]. There are also other types of $3Q$ order, including MML, MLL, and LLL. We performed frozen-phonon calculations to determine which ground state is most favorable, relaxing

the unit cell volume and shape but not further relaxing the atomic coordinates. In other words, nonlinear phonon couplings are omitted.

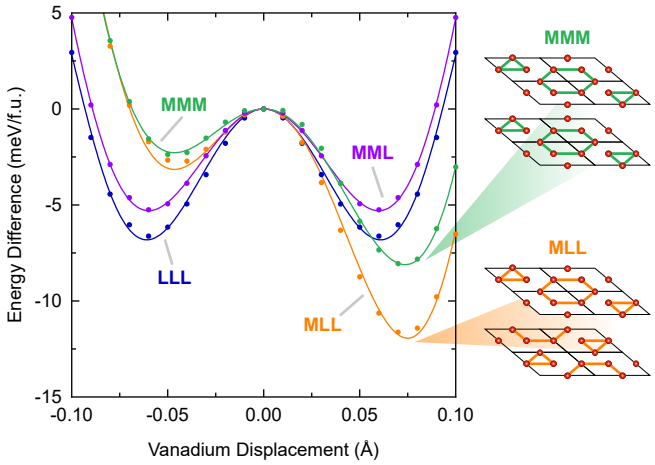

Figure 6.4: **Energy lowering by $3Q$ distortions.** For MMM and MLL configurations, positive displacements correspond to tri-hexagonal distortions and negative displacements correspond to "Star of David" distortions. The lowest energy occurs for the MLL configuration consisting of in-plane tri-hexagonal distortions that are laterally shifted in neighboring planes. Curves are least squares fits to sixth-degree polynomials.

As Fig.6.4 shows, the lowest energy state corresponds to the tri-hexagonal MLL distortion and not the previously assumed MMM distortion. This ground state distortion, consisting of one M- and two L-point modes, can be described as in-plane tri-hexagonal distortions with a lateral shift of one lattice vector between neighboring kagome planes. This conclusion is supported by the earlier experimental observation that the CDW phase transition is first-order, which eliminates the odd-parity MML and LLL distortions.

6.4 Discussion and Outlook

The three modes observed experimentally in Fig.6.2 can be assigned to modes calculated by density functional theory. The fully symmetric γ mode is predicted by DFT to have $f = 4.2$ THz, Γ_1^+. The distortion associated with this mode is depicted in

Fig.6.3(d), and corresponds to the coherent motion of the out-of-plane antimony atoms towards and away from the kagome plane. The α mode is detected at 1.3 THz. Its appearance directly at T_{CDW} indicates that the mode should be associated with the charge density wave transition and therefore must have an irreducible representation of either M_1^+ or L_2^- symmetry. There is indeed a calculated phonon mode with $f = 1.27$ THz having L_2^- symmetry. This distortion involves cesium motion along the c-axis, depicted in Fig.6.3(e). The observation of this mode supports the conclusion that the CDW is of MLL order. Predicted phonon modes also appear at 3.63 THz (M_1^+) and 3.67 THz (L_2^-). Weak spectral intensity can be observed in the Fourier map below T_{CDW} around these frequencies, implying that these modes are present in the data, with a weaker amplitude.

The β resonance extends over a broad spectral range centered at 3.1 THz. Since this mode appears below T_{CDW} at $T^* \approx 60$ K, we believe this resonance may be associated with the $1Q$ uniaxial order observed below this temperature by scanning tunneling microscopy experiments [227, 225, 231]. The uniaxial ordering enlarges the in-plane unit cell beyond the 2×2 $3Q$ reconstruction, and would therefore result in newly active phonon modes through the DECP mechanism, several with frequencies near 3.1 THz. The onset of $3Q$ MML order breaks C_6 rotational symmetry, whereas MMM order does not. This could play a role in the emergence of $1Q$ order at lower temperatures since 1Q order behaves more like a crossover than a sharp phase transition, the fact the C_6 symmetry has already been broken might facilitate the crossover.

Additionally, we suggest the lower onset temperature of the 1Q order could be associated with and order-disorder transition corresponding to c-axis coherence since there are three equivalent MLL configurations distinguished by the direction of the lateral shift of the tri-hexagonal CDW pattern. Long-range ordering of the CDW along the c axis relies on weak next-nearest-neighbor kagome plane interactions and therefore involves smaller energy (and temperature) scales. Further experimental and theoretical studies will be

needed to elucidate the nature of the uniaxial order.

In summary, our experimental coherent phonon spectroscopy results combined with first-principles DFT calculations have uncovered a first-order $3Q$ phase transition which is characterized by the condensation of one M- and two L-point phonons, which we call MLL CDW order. This ordering involves the interlayer modulation of the CDW along the c axis and offers a potential explanation for the uniaxial order observed below T_{CDW}. Our results represent a large step forward in understanding the CDW order in CsV_3Sb_5. Since the completion of this work, further studies have been performed that show longer wavelength modulation than the $k_z = \pi/c$ (L point) wave vectors in this work. These studies will be discussed in Chapter 7 along with suggested avenues for future research.

Chapter 7

Future Directions

7.1 Strontium Titanate

In Chapter 3, we developed a simplified free energy model considering only the necessary degrees of freedom to simulate the temperature dependent polar order in strontium titanate at different doping levels. We found the phase transition to exhibit characteristics of both displacive and order disorder transitions. A similar model could be used to simulate the existence of polar nanodomains in bulk $SrTiO_3$, which have also been observed experimentally. It may also be of interest to add in-plane strain to the model, and see how the formation of polar nanodomains is influenced for various magnitudes and directions of strain. The effects of next-nearest neighbor interactions could also be included for increased accuracy. Local strain around dopant atoms is shown to influence the structure surrounding the dopant [95], so DFT calculations investigating the effects of local strain could be useful. When formulating more complex versions of the model, it may be necessary to employ more advanced machine learning techniques, rather than simple linear regression, to find the values of coefficients for terms which would require large supercells to compute using the linear regression technique.

A similar model could be formulated for the pervoskite oxide $KTaO_3$ which also exhibits enhanced superconductivity at an interface with Rashba splitting of the bands. There no antiferrodistortive rotations in $KTaO_3$, so simulations are significantly simpler. A comparison of the lattice dyanmics and electronic structures of $SrTiO_3$ and $KTaO_3$ may offer insights into how the mechanisms of their superconducting phases may be similar or different.

In Chapter 4, we investigated the evolution of the electronic structure of $SrTiO_3$ with doping, and the effects of spin orbit coupling. We compared the density of states and Fermi energies for the polar and tetragonal structures, and explored the Rashba splitting in the polar phase. Determining the single-band density of states for the unstrained AFD structure and comparing this value to the density of states at the Fermi level in the polar phase may determine if the ferroelectric enhancement of superconductivity could be due to an increased density of states within a single band. Quantifying the Rashba coupling and comparing our results with previous theory papers will be useful in determining whether the Rashba is capable of explaining the observed enhancement of superconductivity deep within the polar phase in the compressively strained system. Calculations of the electron-phonon coupling integrated across the entire Brillouin zone using the EPW code for the polar and tetragonal phases could be performed to compare the electron-phonon coupling constant throughout the relevant range of doping for both structures.

Experimental measurements of the phonon frequency and Fermi energy in the strained system at low temperatures as a function of doping would be extremely valuable to determine if coupling to the polar mode in the ordered ground state would be within the adiabatic regime.

7.2 Quantum Spin Liquids

In Chapter 5, we identified three promising quantum spin liquid candidates through a combinatorial exploration of the chemical phase space of herbertsmithite and Zn-barlowite related compounds: $MgCu_3(OH)_6Br_2$, $CaCu_3(OH)_6ICl$, and $MgCu_3(OH)_6ClF$. In our work, we explored structural and thermodynamic instabilities, as well as the values of desirable structural parameters. A similar high-throughput technique could be applied to other material families in order to find related materials with desirable properties.

Density functional theory cannot accurately calculate the magnetic ground state of a geometrically frustrated material, and thus, we did not directly consider magnetism in our calculations. However, Hubbard models and calculation of the exchange coefficients could be performed to more directly investigate the magnetic ground state of our candidate materials.

The next step after identifying promising candidate materials is to attempt to synthesize these compounds. In addition to synthesizing the three final candidates, two other candidates that showed instabilities in their phonon dispersions ($CaCu_3(OH)_6IBr$ and $MgCu_3(OH)_6BrF$) may in fact be stable at room temperature since $ZnCu_3(OH)_6ClF$ had the same calculated imaginary eigenvectors but is stable at room temperature [199]. We encourage experimental groups with experience in hydrothermal synthesis to try synthesizing these compounds.

7.3 Kagome Metals

In Chapter 6, we demonstrated that there is interlayer modulation of charge density wave order along the c-axis in CsV_3Sb_5. Since the publication of the work discussed in Chapter 6 [204], additional experiments have been performed revealing a $2 \times 2 \times 4$ lattice

structure with both TrH- and SoD-like distortions of the kagome layers [214].

There seems to be some degree of randomness to the particular layer distortions. A model incorporating statistical mechanics, similar to that discussed in Chapter 3, could be used to simulate the equilibrium charge order and account for any stochastic contributions to the CDW. Additionally, in order to confirm the existence of the CDW, calculations of the charge density may be useful in determining whether the structural modulation of the atoms is causing the expected changes in charge density, and to what degree the charge density is localized on the atoms.

Appendix A

Strontium Titanate Model

A.1 Polynomial Terms: Version 1

The full polynomial expression for the model described in Section 3.6 is given below. Coupling to the additional elongation of the c axis in the polar phase is considered.

Constant

$$a_0$$

Strain

$$a_1 C + a_2 C^2$$

Quadratic Coupling

$$a_{3-8} R^2 + a_{9-14} Ti^2 + a_{15-20} O_{in}^2 + a_{21-26} O_{out}^2$$

Bilinear Coupling

$$a_{27-32}(Ti * O_{in}) + a_{33-38}(Ti * O_{out}) + a_{39-44}(O_{in} * O_{out})$$

Strain and Bilinear Coupling

$$a_{45-50} C(Ti * O_{in}) + a_{51-56} C(Ti * O_{out}) + a_{57-62} C(O_{in} * O_{out})$$

Strain and Quadratic Coupling

$$a_{63-68} C(R^2) + a_{69-74} C(Ti^2) + a_{75-80} C(O_{in}^2) + a_{81-86} C(O_{out}^2)$$

Quartic Terms

Coupling to nearest neighbors is no longer considered for higher order terms, though averaging the amplitudes for the displacement of the oxygen ions is accounted for.

Quadratic Rotation and Polarization Components

$$a_{87}R^2Ti^2 + a_{88}R^2O_{in}2 + a_{89}R^2O_{out}^2$$

Two Quadratic Polarization Components

$$a_{90}Ti^2O_{in}^2 + a_{91}Ti^2O_{out}^2 + a_{92}O_{in}^2O_{out}^2$$

Single Component Quartic Terms

$$a_{93}R^4 + a_{94}Ti^4 + a_{95}O_{in}^4 + a_{96}O_{out}^4$$

One Cubic and One Linear Polarization Component

$$a_{97}(Ti^3 * O_{in}) + a_{98}(Ti^3 * O_{out}) + a_{99}(Ti * O_{in}^3) + a_{100}(O_{in}^3 * O_{out}) + a_{101}(Ti * O_{out}^3) + a_{102}(O_{in} * O_{out}^3)$$

One Quadratic, Two Linear Polarization Components

$$a_{103}(Ti^2 * O_{in} * O_{out}) + a_{104}(Ti * O_{in}^2 * O_{out}) + a_{105}(Ti * O_{in} * O_{out}^2)$$

Two Linear Polarization Components and Quadratic Rotation

$$a_{106}(R^2 * Ti * O_{in}) + a_{107}(R^2 * Ti * O_{in}) + a_{108}(R^2 * Ti * O_{in})$$

A.2 Constraints: Version 1

In-Plane Oxygen (M,A)

M: $a_{15} - 4a_{16} + 2a_{17} + 4a_{18} - 8a_{19} + 8a_{20} = 0$

A: $a_{15} - 4a_{16} - 2a_{17} + 4a_{18} + 8a_{19} - 8a_{20} = 0$

Titanium and In-Plane oxygen at (M,A)

M: $a_{27} - 4a_{28} + 2a_{29} + 4a_{30} - 8a_{31} + 8a_{32} = 0$

A: $a_{27} - 4a_{28} - 2a_{29} + 4a_{30} + 8a_{31} - 8a_{32} = 0$

In-Plane Oxygen and Strain (M,A)

A: $a_{75} - 4a_{76} - 2a_{77} + 4a_{78} + 8a_{79} - 8a_{80} = 0$

M: $a_{75} - 4a_{76} + 2a_{77} + 4a_{78} - 8a_{79} + 8a_{80} = 0$

Titanium, In-Plane, and Strain (M,A)

M: $a_{45} - 4a_{46} + 2a_{47} + 4a_{48} - 8a_{49} + 8a_{50} = 0$

A: $a_{45} - 4a_{46} - 2a_{47} + 4a_{48} + 8a_{49} - 8a_{50} = 0$

Constraints for Out-of-Plane Oxygen at (Z,A,R)

Z: $a_{21} + 4a_{22} - 2a_{23} + 4a_{24} - 8a_{25} - 8a_{26} = 0$

R: $a_{21} - 2a_{23} - 4a_{24} + 8a_{26} = 0$

A: $a_{21} - 4a_{22} - 2a_{23} + 4a_{24} + 8a_{25} - 8a_{26} = 0$

Titanium and Out-of-Plane Oxygen at (Z,A,R)

Z: $a_{33} + 4a_{34} - 2a_{35} + 4a_{36} - 8a_{37} - 8a_{38} = 0$

R: $a_{33} - 2a_{34} - 4a_{35} + 8a_{36} = 0$

A: $a_{33} - 4a_{34} - 2a_{35} + 4a_{36} + 8a_{37} - 8a_{38} = 0$

Out-of-Plane Oxygen and Strain (Z,A,R)

Z: $a_{81} + 4a_{82} - 2a_{83} + 4a_{84} - 8a_{85} - 8a_{86} = 0$

R: $a_{81} - 2a_{83} - 4a_{84} + 8a_{85} = 0$

A: $a_{81} - 4a_{82} - 2a_{83} + 4a_{84} + 8a_{85} - 8a_{86} = 0$

Titanium, Out-of-Plane Oxygen, and Strain (Z,A,R)

Z: $a_{51} + 4a_{52} - 2a_{53} + 4a_{54} - 8a_{55} - 8a_{56} = 0$

R: $a_{51} - 2a_{53} - 4a_{54} + 8a_{56} = 0$

A: $a_{51} - 4a_{53} - 2a_{54} + 4a_{55} + 8a_{56} - 8a_{57} = 0$

In- and Out-of-Plane Oxygen at (M,Z,A,R)

M: $a_{39} - 4a_40 + 2a_{41} + 4a_{42} - 8a_{43} + 8a_{44} = 0$

Z: $a_{39} + 4a_40 - 2a_{41} + 4a_{42} - 8a_{43} - 8a_{44} = 0$

R: $a_{39} - 2a_{41} - 4a_{42} + 8a_{44} = 0$

A: $a_{39} - 4a_{40} - 2a_{41} + 4a_{42} + 8a_{43} - 8a_{44} = 0$

In- and Out-of-Plane Oxygen and Strain (M,Z,A,R)

M: $a_{57} - 4a_{58} + 2a_{59} + 4a_{60} - 8a_{61} + 8a_{62} = 0$

Z: $a_{57} + 4a_{58} - 2a_{59} + 4a_{60} - 8a_61 - 8a_{62} = 0$

R: $a_{57} - 2a_{59} - 4a_{60} + 8a_{62} = 0$

A: $a_{57} - 4a_{58} - 2a_{59} + 4a_{60} + 8a_{61} - 8a_{62} = 0$

Rotation (Γ,Z)

Γ: $a_3 + 4a_4 + 2a_5 + 4a_6 + 8a_7 + 8a_8 = 0$

Z: $a_3 + 4a_4 - 2a_5 + 4a_6 - 8a_7 - 8a_8 = 0$

Rotation and Strain (Γ,Z)

Γ: $a_{63} + 4a_{64} + 2a_{65} + 4a_{66} + 8a_{67} + 8a_{68} = 0$

Z: $a_{63} + 4a_{64} - 2a_{65} + 4a_{66} - 8a_{67} - 8a_{68} = 0$

A.3 Polynomial Terms: Version 2

The full polynomial expression for the model described in Section 3.5.1 is given below. Here, no elongation of the c axis is considered as the out-of-plane strain was set to the experimental value. Sixth-order on-site terms were included to avoid divergences.

Constant

$$a_0$$

Quadratic Coupling

$$a_{1-6}R^2 + a_{7-12}Ti^2 + a_{13-18}O_{in}^2 + a_{19-24}O_{out}^2$$

Bilinear Coupling

$$a_{25-30}(Ti * O_{in}) + a_{31-36}(Ti * O_{out}) + a_{37-42}(O_{in} * O_{out})$$

Quartic Terms

Coupling to nearest neighbors is no longer considered for higher order terms, though

averaging the amplitudes for the displacement of the oxygen ions is accounted for.

Quadratic Rotation and Polarization Components

$$a_{43}R^2Ti^2 + a_{44}R^2O_in2 + a_{45}R^2O_{out}^2$$

Two Quadratic Polarization Components

$$a_{46}Ti^2O_{in}^2 + a_{47}Ti^2O_{out}^2 + a_{48}O_{in}^2O_{out}^2$$

Single Component Quartic Terms

$$a_{49}R^4 + a_{50}Ti^4 + a_{51}O_{in}^4 + a_{52}O_{out}^4$$

One Cubic and One Linear Polarization Component

$$a_{53}(Ti^3{*}O_{in})+a_{54}(Ti^3{*}O_{out})+a_{55}(Ti{*}O_{in}^3)+a_{56}(O_{in}^3{*}O_{out})+a_{57}(Ti{*}O_{out}^3)+a_{58}(O_{in}{*}O_{out}^3)$$

One Quadratic, Two Linear Polarization Components

$$a_{59}(Ti^2 * O_{in} * O_{out}) + a_{60}(Ti * O_{in}^2 * O_{out}) + a_{61}(Ti * O_{in} * O_{out}^2)$$

Two Linear Polarization Components and Quadratic Rotation

$$a_{62}(R^2 * Ti * O_{in}) + a_{63}(R^2 * Ti * O_{in}) + a_{64}(R^2 * Ti * O_{in})$$

Two Linear Polarization Components and Quadratic Rotation

$$a_{65}(R^6) + a_{66}(Ti^6) + a_{67}(O_{in}^6) + a_{68}(O_{out}^6)$$

A.4 Constraints: Version 2

In-Plane Oxygen (M,A)

M: $a_{15} - 4a_{16} + 2a_{17} + 4a_{18} - 8a_{19} + 8a_{20} = 0$

A: $a_{15} - 4a_{16} - 2a_{17} + 4a_{18} + 8a_{19} - 8a_{20} = 0$

Titanium and In-Plane oxygen at (M,A)

M: $a_{27} - 4a_{28} + 2a_{29} + 4a_{30} - 8a_{31} + 8a_{32} = 0$

A: $a_{27} - 4a_{28} - 2a_{29} + 4a_{30} + 8a_{31} - 8a_{32} = 0$

Constraints for Out-of-Plane Oxygen at (Z,A,R)

Z: $a_{21} + 4a_{22} - 2a_{23} + 4a_{24} - 8a_{25} - 8a_{26} = 0$

R: $a_{21} - 2a_{23} - 4a_{24} + 8a_{26} = 0$

A: $a_{21} - 4a_{22} - 2a_{23} + 4a_{24} + 8a_{25} - 8a_{26} = 0$

Titanium and Out-of-Plane Oxygen at (Z,A,R)

Z: $a_{33} + 4a_{34} - 2a_{35} + 4a_{36} - 8a_{37} - 8a_{38} = 0$

R: $a_{33} - 2a_{34} - 4a_{35} + 8a_{36} = 0$

A: $a_{33} - 4a_{34} - 2a_{35} + 4a_{36} + 8a_{37} - 8a_{38} = 0$

In- and Out-of-Plane Oxygen at (M,Z,A,R)

M: $a_{39} - 4a_{40} + 2a_{41} + 4a_{42} - 8a_{43} + 8a_{44} = 0$

Z: $a_{39} + 4a_{40} - 2a_{41} + 4a_{42} - 8a_{43} - 8a_{44} = 0$

R: $a_{39} - 2a_{41} - 4a_{42} + 8a_{44} = 0$

A: $a_{39} - 4a_{40} - 2a_{41} + 4a_{42} + 8a_{43} - 8a_{44} = 0$

Rotation (Γ,Z)

Γ: $a_3 + 4a_4 + 2a_5 + 4a_6 + 8a_7 + 8a_8 = 0$

Z: $a_3 + 4a_4 - 2a_5 + 4a_6 - 8a_7 - 8a_8 = 0$

A.5 Phonon Model

We begin with the Euler-Lagrange equation, where ϕ_n is the value of a degree of freedom in unit cell n:

$$\frac{\partial L}{\partial \phi_n} - \frac{d}{dt}\frac{\partial L}{\partial \dot{\phi}_n} = 0 \tag{A.1}$$

$$\frac{\partial L}{\partial \phi_n} = -\frac{\partial V}{\partial \phi_n} \text{ since } \frac{\partial T}{\partial \dot{\phi}_n} = 0 \text{ contains only } \dot{\phi} \tag{A.2}$$

$$\frac{\partial L}{\partial \dot{\phi}_n} = -\frac{\partial T}{\partial \dot{\phi}_n} \text{ since } \frac{\partial V}{\partial \phi_n} = 0 \text{ contains only } \phi \tag{A.3}$$

We now solve for the left- and right-hand sides of the following simplified equation:

$$-\frac{\partial V}{\partial \phi_n} = \frac{d}{dt}\frac{\partial T}{\partial \dot{\phi}_n} \tag{A.4}$$

The ansatz for the order parameter and its derivatives are given by:

$$\begin{aligned} \phi_n &= Ae^{i(\omega t - q\cdot n)} \\ \dot{\phi}_n &= i\omega\phi_n \\ \ddot{\phi}_n &= -\omega^2\phi_n \\ \phi_{n+\delta} &= \phi_n e^{iq\cdot\delta} \end{aligned} \tag{A.5}$$

The polarization order parameter is a vector with three components corresponding to the vector below, where x,y,z should not be confused with Cartesian directions:

$$\phi_n = \begin{pmatrix} x_n \\ y_n \\ z_n \end{pmatrix} \tag{A.6}$$

The left-hand side of Eq.A.4 can be expressed as a 3×3 matrix, whose components are found by plugging the ansatz given in Eq.A.5 into the quadratic terms of the free energy expression, taking the derivative, and simplifying:

$$-\frac{\partial V(\phi)}{\partial \phi} = \begin{bmatrix} xx & xy & xz \\ yx & yy & yz \\ zx & zy & zz \end{bmatrix} = \begin{bmatrix} \frac{\partial V(x)}{\partial x} & \frac{\partial V(x)}{\partial y} & \frac{\partial V(x)}{\partial z} \\ \frac{\partial V(y)}{\partial x} & \frac{\partial V(y)}{\partial y} & \frac{\partial V(y)}{\partial z} \\ \frac{\partial V(z)}{\partial x} & \frac{\partial V(z)}{\partial y} & \frac{\partial V(z)}{\partial z} \end{bmatrix} \tag{A.7}$$

We now solve for the right-hand side of Eq.A.4 where the kinetic energy has the general form $T = \frac{1}{2}m\dot{\phi}^2$:

$$T = \frac{1}{2}mv^2 \tag{A.8}$$

$$T = \sum_n \frac{1}{2} m_x x_{GSD}^2 \dot{x}_n^2 + m_y D_y^2 \left(\frac{\dot{y} + \dot{y}_{n+\delta=010}}{4} \right) ... \\ ... + m_y D_y^2 \left(\frac{\dot{y} + \dot{y}_{n+\delta=100}}{4} \right) + m_z D_z^2 \left(\frac{\dot{z} + \dot{z}_{n+\delta=001}}{4} \right) \tag{A.9}$$

Here, D_ϕ is the ground state displacement in meters and m_ϕ is the mass of the ion species in kilograms. For the x order parameter, we plug in our ansatz and simplify to obtain:

$$\frac{T}{\dot{x}_n} = 4 \sum_r [m_x D_x^2 \dot{x}_n] \tag{A.10}$$

$$L_x = \frac{d}{dt} \frac{\partial T}{\partial \dot{x}_n} \tag{A.11}$$

We follow the same process for the other components of the polarization order parameter. Note that here $\hat{x}, \hat{y}$, and $\hat{z}$ do correspond to vectors along the Cartesian directions:

$$L_y = \frac{d}{dt} \frac{\partial T}{\partial \dot{x}_n} = -\omega^2 m_y D_y^2 y \left(cos^2 \left(\frac{q \cdot \hat{y}}{2} \right) + cos^2 \left(\frac{q \cdot \hat{x}}{2} \right) \right) \tag{A.12}$$

$$L_z = \frac{d}{dt} \frac{\partial T}{\partial \dot{z}_n} = -\omega^2 m_z D_z^2 z cos^2 \left(\frac{q \cdot \hat{z}}{2} \right) \tag{A.13}$$

Our final eigenvalue equation is:

$$\omega_p^2 \begin{bmatrix} x \\ y \\ z \end{bmatrix} = \begin{bmatrix} \frac{xx}{L_x} & \frac{xy}{L_x} & \frac{xy}{L_x} \\ \frac{yx}{L_y} & \frac{yy}{L_y} & \frac{yz}{L_y} \\ \frac{zx}{L_z} & \frac{zy}{L_z} & \frac{zz}{L_z} \end{bmatrix} \begin{bmatrix} x \\ y \\ z \end{bmatrix} \tag{A.14}$$

Eq.A.14 is solved numerically to obtain the wavevector-dependent frequencies of the three polarization bands. We follow a similar procedure for the rotation, although here, we have only a single order parameter.

$$-\frac{\partial V}{\phi_n} = \frac{d}{dt} \frac{\partial T}{\partial \dot{\phi}_n} \tag{A.15}$$

$$\partial \frac{V}{\phi_n} = \phi \left[2a_3 + \sum_{\delta} a_{4-8} e^{-iq\cdot\delta} \right] \tag{A.16}$$

$$\frac{d}{dt}\frac{\partial T}{\partial \dot{\phi}_n} = -\omega^2 m_o R_{GSD}^2 \phi \left[sin^2\left(\frac{q\cdot\hat{y}}{2}\right) + sin^2\left(\frac{q\cdot\hat{x}}{2}\right) \right] \tag{A.17}$$

$$\omega_R = \sqrt{\frac{1}{m_o R_{GSD}^2}} \left(\frac{[2a_3 + \sum_{\delta} a_{4-8} e^{-iq\cdot\delta}]}{[sin^2(\frac{q\cdot\hat{y}}{2}) + sin^2(\frac{q\cdot\hat{x}}{2})]} \right) \tag{A.18}$$

Appendix B

Quantum Spin Liquid Data

Table B.1: Parameters for all herbertsmithite-related compounds: the lowest optical phonon frequency (f_o), energy above the hull (E_{hull}), the copper-oxygen-copper bond angle ($\theta_{Cu-O-Cu}$), interplane distance between kagome layers (d_{inter}), and distance between in-plane copper ions (d_{in}).

Compound	f_0 (THz)	E_{hull} (meV/atom)	$\theta_{\text{cu-O-Cu}}$	d_{inter}	d_{in}
$BaCu_3(OH)_6Br_2$	-0.96	65.7	126.9	6.04	3.49
$BaCu_3(OH)_6Cl_2$	-1.26	86.0	126.4	6.04	3.48
$BaCu_3(OH)_6F_2$	0.73	119.9	122.8	6.01	3.43
$BaCu_3(OH)_6I_2$	0.41	42.6	128.0	6.09	3.53
$BeCu_3(OH)_6Br_2$	2.58	132.2	124.7	4.26	3.60
$BeCu_3(OH)_6Cl_2$	3.24	89.2	123.3	4.20	3.53
$BeCu_3(OH)_6F_2$	3.53	82.8	116.8	4.14	3.32
$BeCu_3(OH)_6I_2$	-4.37	210.5	125.6	4.38	3.72
$CaCu_3(OH)_6Br_2$	0.50	30.7	125.7	5.19	3.53
$CaCu_3(OH)_6Cl_2$	0.70	44.8	125.8	5.06	3.51
$CaCu_3(OH)_6F_2$	2.27	103.8	122.1	5.10	3.43
$CaCu_3(OH)_6I_2$	0.83	56.8	125.8	5.38	3.57
$CdCu_3(OH)_6Br_2$	1.34	71.9	126.5	5.05	3.55
$CdCu_3(OH)_6Cl_2$	1.67	62.5	126.6	4.94	3.53
$CdCu_3(OH)_6F_2$	2.16	47.4	121.8	5.03	3.42
$CdCu_3(OH)_6I_2$	1.24	99.1	126.2	5.24	3.59
$CuCu_3(OH)_6Br_2$	2.12	72.6	124.5	4.74	3.55
$CuCu_3(OH)_6Cl_2$	2.68	45.7	123.7	4.63	3.50
$CuCu_3(OH)_6F_2$	3.13	8.5	119.3	4.62	3.37
$CuCu_3(OH)_6I_2$	-2.09	130.8	125.2	4.95	3.60

Table B.2: Herbertsmithite data (continued)

Compound	f_0 (THz)	E_{hull} (meV/atom)	$\theta_{\text{cu-O-Cu}}$	d_{inter}	d_{in}
$GeCu_3(OH)_6Br_2$	-2.25	70.4	127.4	5.08	3.55
$GeCu_3(OH)_6Cl_2$	-2.44	-31.6	114.9	4.57	3.59
$GeCu_3(OH)_6F_2$	1.44	-11.7	106.2	4.70	3.32
$GeCu_3(OH)_6I_2$	-3.52	101.1	127.0	5.30	3.59
$HgCu_3(OH)_6Br_2$	0.97	107.7	127.7	5.17	3.55
$HgCu_3(OH)_6Cl_2$	1.13	89.9	128.0	5.08	3.53
$HgCu_3(OH)_6F_2$	1.38	24.0	122.1	5.24	3.41
$HgCu_3(OH)_6I_2$	0.84	146.6	127.4	5.36	3.58
$MgCu_3(OH)_6Br_2$	2.23	36.0	125.2	4.65	3.57
$MgCu_3(OH)_6Cl_2$	2.74	7.1	124.6	4.52	3.53
$MgCu_3(OH)_6F_2$	3.63	67.3	120.6	4.44	3.40
$MgCu_3(OH)_6I_2$	1.75	94.0	124.9	4.85	3.64
$PbCu_3(OH)_6Br_2$	-0.77	76.3	127.7	5.58	3.52
$PbCu_3(OH)_6Cl_2$	-0.57	77.2	128.1	5.52	3.52
$PbCu_3(OH)_6F_2$	1.29	86.0	122.6	5.64	3.43
$PbCu_3(OH)_6I_2$	-0.71	84.9	127.6	5.76	3.54
$SnCu_3(OH)_6Br_2$	-3.57	18.5	117.8	4.81	3.69
$SnCu_3(OH)_6Cl_2$	-2.67	11.7	116.8	4.76	3.62
$SnCu_3(OH)_6F_2$	-1.95	28.5	109.7	4.91	3.40
$SnCu_3(OH)_6I_2$	-0.99	94.8	127.6	5.63	3.56
$SrCu_3(OH)_6Br_2$	-1.07	46.4	125.9	5.57	3.50
$SrCu_3(OH)_6Cl_2$	-1.27	68.1	126.2	5.50	3.49
$SrCu_3(OH)_6F_2$	1.46	117.9	122.4	5.53	3.43
$SrCu_3(OH)_6I_2$	-0.42	33.8	126.4	5.72	3.54
$ZnCu_3(OH)_6Br_2$	2.17	58.2	125.6	4.69	3.57
$ZnCu_3(OH)_6Cl_2$	2.63	41.2	125.0	4.58	3.53
$ZnCu_3(OH)_6F_2$	2.98	30.1	120.6	4.55	3.40
$ZnCu_3(OH)_6I_2$	1.56	108.8	125.5	4.88	3.64

Table B.3: Parameters for all Zn-barlowite-related compounds: the lowest optical phonon frequency (f_0), energy above the hull (E_{hull}), the copper-oxygen-copper bond angle ($\theta_{\text{Cu-O-Cu}}$), interplane distance between kagome layers (d_{inter}), and distance between in-plane copper ions (d_{in}).

Compound	f_0 (THz)	E_{hull} (meV/atom)	$\theta_{\text{cu-O-Cu}}$	d_{inter}	d_{in}
$BaCu_3(OH)_6BrCl$	-1.18	80.6	124.4	5.99	3.45
$BaCu_3(OH)_6BrF$	-5.54	137.7	119.3	5.93	3.37
$BaCu_3(OH)_6ClF$	-5.69	157.2	118.6	5.94	3.35
$BaCu_3(OH)_6IBr$	-0.44	50.7	126.9	6.03	3.50
$BaCu_3(OH)_6ICl$	-0.49	60.0	125.1	6.00	3.48
$BaCu_3(OH)_6IF$	5.49	117.8	120.5	5.94	3.40
$BeCu_3(OH)_6BrCl$	-5.52	140.5	125.1	4.34	3.56
$BeCu_3(OH)_6BrF$	-2.84	97.0	116.4	4.46	3.36
$BeCu_3(OH)_6ClF$	-2.71	91.4	117.0	4.41	3.35
$BeCu_3(OH)_6IBr$	-6.15	182.1	126.7	4.39	3.65
$BeCu_3(OH)_6ICl$	-5.89	154.5	124.2	4.42	3.58
$BeCu_3(OH)_6IF$	-4.27	117.4	115.9	4.52	3.38
$CaCu_3(OH)_6BrCl$	-0.68	34.6	125.9	5.10	3.52
$CaCu_3(OH)_6BrF$	-2.25	72.7	118.4	5.05	3.39
$CaCu_3(OH)_6ClF$	-2.08	89.3	118.6	5.01	3.38
$CaCu_3(OH)_6IBr$	0.77	31.6	127.7	5.20	3.58
$CaCu_3(OH)_6ICl$	0.94	19.2	125.4	5.17	3.54
$CaCu_3(OH)_6IF$	-1.06	60.3	118.3	5.11	3.41
$CdCu_3(OH)_6BrCl$	-0.36	67.0	126.7	4.99	3.54
$CdCu_3(OH)_6BrF$	-0.81	65.2	118.6	4.99	3.39
$CdCu_3(OH)_6ClF$	-1.14	71.4	118.9	4.95	3.39
$CdCu_3(OH)_6IBr$	0.77	78.9	128.5	5.07	3.60
$CdCu_3(OH)_6ICl$	0.86	65.0	126.0	5.06	3.55
$CdCu_3(OH)_6IF$	-1.51	65.7	118.3	5.06	3.41
$CuCu_3(OH)_6BrCl$	-1.81	67.1	126.1	4.70	3.54
$CuCu_3(OH)_6BrF$	-1.24	38.5	117.5	4.73	3.37
$CuCu_3(OH)_6ClF$	-1.37	38.2	118.0	4.68	3.36
$CuCu_3(OH)_6IBr$	-2.23	99.6	127.8	4.79	3.60
$CuCu_3(OH)_6ICl$	-1.82	76.4	125.2	4.79	3.55
$CuCu_3(OH)_6IF$	-1.10	51.1	116.8	4.81	3.38
$GeCu_3(OH)_6BrCl$	-4.26	32.1	120.7	4.61	3.66
$GeCu_3(OH)_6BrF$	-1.68	32.5	109.0	4.86	3.39
$GeCu_3(OH)_6ClF$	-2.69	38.8	108.7	4.85	3.37
$GeCu_3(OH)_6IBr$	-5.73	44.8	122.9	4.61	3.76
$GeCu_3(OH)_6ICl$	-5.03	29.5	119.9	4.67	3.68
$GeCu_3(OH)_6IF$	-2.22	36.1	109.8	4.87	3.43

Table B.4: Parameters for all Zn-barlowite-related compounds (continued): the lowest optical phonon frequency (f_0), energy above the hull (E_{hull}), the copper-oxygen-copper bond angle ($\theta_{\text{Cu-O-Cu}}$), interplane distance between kagome layers (d_{inter}), and distance between in-plane copper ions (d_{in}).

Compound	f_0 (THz)	E_{hull} (meV/atom)	$\theta_{\text{cu-O-Cu}}$	d_{inter}	d_{in}
$HgCu_3(OH)_6BrCl$	-0.25	98.8	127.2	5.13	3.53
$HgCu_3(OH)_6BrF$	-2.24	80.4	119.2	5.13	3.39
$HgCu_3(OH)_6ClF$	-2.15	82.3	119.5	5.08	3.39
$HgCu_3(OH)_6IBr$	0.75	120.3	129.0	5.21	3.59
$HgCu_3(OH)_6ICl$	0.89	103.6	126.6	5.20	3.54
$HgCu_3(OH)_6IF$	-2.47	87.2	118.9	5.19	3.41
$MgCu_3(OH)_6BrCl$	0.35	26.9	126.1	4.61	3.56
$MgCu_3(OH)_6BrF$	1.57	26.1	117.6	4.65	3.39
$MgCu_3(OH)_6ClF$	1.09	39.6	118.1	4.60	3.38
$MgCu_3(OH)_6IBr$	-0.15	59.8	127.8	4.68	3.64
$MgCu_3(OH)_6ICl$	-0.43	35.9	125.2	4.68	3.58
$MgCu_3(OH)_6IF$	1.24	18.9	117.2	4.72	3.41
$PbCu_3(OH)_6BrCl$	-1.00	77.9	126.0	5.54	3.49
$PbCu_3(OH)_6BrF$	-4.54	114.4	119.5	5.49	3.39
$PbCu_3(OH)_6ClF$	-4.46	124.9	119.4	5.46	3.38
$PbCu_3(OH)_6IBr$	-0.76	74.9	127.8	5.64	3.54
$PbCu_3(OH)_6ICl$	-0.60	70.7	125.8	5.60	3.50
$PbCu_3(OH)_6IF$	-4.50	108.8	119.6	5.55	3.40
$SnCu_3(OH)_6BrCl$	-3.64	38.5	121.5	4.79	3.68
$SnCu_3(OH)_6BrF$	-1.84	38.5	109.3	5.03	3.41
$SnCu_3(OH)_6ClF$	-2.67	47.4	108.9	5.03	3.39
$SnCu_3(OH)_6IBr$	-4.85	48.9	124.0	4.78	3.78
$SnCu_3(OH)_6ICl$	-4.07	32.0	120.9	4.83	3.70
$SnCu_3(OH)_6IF$	-1.41	37.3	110.2	5.03	3.45
$SrCu_3(OH)_6BrCl$	-1.17	55.9	125.1	5.51	3.49
$SrCu_3(OH)_6BrF$	-4.38	106.2	118.6	5.44	3.37
$SrCu_3(OH)_6ClF$	-4.18	125.9	118.4	5.41	3.36
$SrCu_3(OH)_6IBr$	-0.69	33.1	127.1	5.59	3.53
$SrCu_3(OH)_6ICl$	-0.50	37.6	125.1	5.55	3.50
$SrCu_3(OH)_6IF$	-4.45	89.8	119.0	5.48	3.40
$ZnCu_3(OH)_6BrCl$	-0.34	54.5	126.6	4.64	3.56
$ZnCu_3(OH)_6BrF$	1.41	38.6	118.0	4.69	3.39
$ZnCu_3(OH)_6ClF$	0.89	43.1	118.5	4.64	3.38
$ZnCu_3(OH)_6IBr$	-0.38	74.8	128.3	4.71	3.64
$ZnCu_3(OH)_6ICl$	0.57	54.3	125.7	4.71	3.58
$ZnCu_3(OH)_6IF$	1.19	42.5	117.5	4.76	3.41

Bibliography

[1] Karin M. Rabe, Charles H. Ahn, and Jean-Marc Triscone, editors. *Physics of Ferroelectrics: A Modern Perspective*. Number v. 105 in Topics in Applied Physics. Springer, Berlin ; New York, 2007.

[2] J. Valasek. Piezoelectric and allied phenomena in rochelle salt. *Phys. Rev.*, 17:475–481, April 1921.

[3] Walter J. Merz. The electric and optical behavior of $BaTiO_3$ single-domain crystals. *Phys. Rev.*, 76:1221–1225, October 1949.

[4] Toyoto Sato, Shigeyuki Takagi, Stefano Deledda, Bjørn C. Hauback, and Shinichi Orimo. Extending the applicability of the Goldschmidt tolerance factor to arbitrary ionic compounds. *Scientific Reports*, 6(1):23592, April 2016.

[5] Victor Moritz Goldschmidt. Die gesetze der krystallochemie. *Naturwissenschaften*, 14(21):477–485, 1926.

[6] R. A. Cowley. Lattice Dynamics and Phase Transitions of Strontium Titanate. *Physical Review*, 134(4A):A981–A997, May 1964.

[7] Sayantika Bhowal and Nicola A. Spaldin. Polar Metals: Principles and Prospects. *Annual Review of Materials Research*, 53(1):53–79, 2023.

[8] P. W. Anderson and E. I. Blount. Symmetry considerations on martensitic transformations: "ferroelectric" metals? *Phys. Rev. Lett.*, 14:217–219, February 1965.

[9] Clément Collignon, Xiao Lin, Carl Willem Rischau, Benoît Fauqué, and Kamran Behnia. Metallicity and Superconductivity in Doped Strontium Titanate. *Annual Review of Condensed Matter Physics*, 10(1):25–44, March 2019.

[10] Piers Coleman and Andrew J. Schofield. Quantum criticality. *Nature*, 433(7023):226–229, January 2005.

[11] Jonathan M. Edge, Yaron Kedem, Ulrich Aschauer, Nicola A. Spaldin, and Alexander V. Balatsky. Quantum Critical Origin of the Superconducting Dome in $SrTiO_3$. *Physical Review Letters*, 115(24):247002, December 2015.

[12] J. Bardeen, L. N. Cooper, and J. R. Schrieffer. Theory of superconductivity. *Phys. Rev.*, 108:1175–1204, Dec 1957.

[13] Michael Tinkham. *Introduction to Superconductivity*. Dover Publications, 2 edition, June 2004.

[14] Yaron Kedem. Novel pairing mechanism for superconductivity at a vanishing level of doping driven by critical ferroelectric modes. *Physical Review B*, 98(22):220505, December 2018.

[15] Leon N. Cooper. Bound electron pairs in a degenerate Fermi gas. *Phys. Rev.*, 104:1189–1190, November 1956.

[16] Manfred Sigrist, Adolfo Avella, and Ferdinando Mancini. Introduction to unconventional superconductivity in non-centrosymmetric metals. In *AIP Conference Proceedings*, pages 55–96, Salerno (Italy), 2009. AIP.

[17] H. Tou, Y. Kitaoka, K. Asayama, N. Kimura, Y. Ōnuki, E. Yamamoto, and K. Maezawa. Odd-parity superconductivity with parallel spin pairing in upt_3: Evidence from ^{195}Pt knight shift study. *Phys. Rev. Lett.*, 77:1374–1377, Aug 1996.

[18] G.E. Volovik. An analog of the quantum Hall effect in a superfluid ^{3}He film. *Soviet Physics - JETP (English Translation)*, 67(9):1804–1811, 1988.

[19] E. F. Talantsev, K. Iida, T. Ohmura, T. Matsumoto, W. P. Crump, N. M. Strickland, S. C. Wimbush, and H. Ikuta. P-wave superconductivity in iron-based superconductors. *Scientific Reports*, 9(1):14245, October 2019.

[20] Kyle M. Shen and J.C. Seamus Davis. Cuprate high-T_c superconductors. *Materials Today*, 11(9):14–21, 2008.

[21] G. R. Stewart. Unconventional superconductivity. *Advances in Physics*, 66(2):75–196, 2017.

[22] Yuji Matsuda and Hiroshi Shimahara. Fulde–ferrell–larkin–ovchinnikov state in heavy fermion superconductors. *Journal of the Physical Society of Japan*, 76(5):051005, 2007.

[23] Masatoshi Sato and Yoichi Ando. Topological superconductors: A review. *Reports on Progress in Physics*, 80(7):076501, July 2017.

[24] Ettore Majorana and Luciano Maiani. *A symmetric theory of electrons and positrons*, pages 201–233. Springer Berlin Heidelberg, Berlin, Heidelberg, 2006.

[25] Bernard van Heck Sebastian Rubbert Rafał Skolasiński Bas Nijholt Irfan Muhammad Tómas Örn Rosdahl Anton Akhmerov, Jay Sau. Online course on topology in condensed matter. 2021.

[26] M Smidman, M B Salamon, H Q Yuan, and D F Agterberg. Superconductivity and spin–orbit coupling in non-centrosymmetric materials: A review. *Reports on Progress in Physics*, 80(3):036501, March 2017.

[27] Xiaoming Zhang, Jiale Liu, and Feng Liu. Topological Superconductivity Based on Antisymmetric Spin–Orbit Coupling. *Nano Letters*, 22(22):9000–9005, November 2022.

[28] Vladyslav Kozii and Liang Fu. Odd-Parity Superconductivity in the Vicinity of Inversion Symmetry Breaking in Spin-Orbit-Coupled Systems. *Physical Review Letters*, 115(20):207002, November 2015.

[29] Yuxuan Wang, Gil Young Cho, Taylor L. Hughes, and Eduardo Fradkin. Topological superconducting phases from inversion symmetry breaking order in spin-orbit-coupled systems. *Physical Review B*, 93(13):134512, April 2016.

[30] Timo Schumann, Luca Galletti, Hanbyeol Jeong, Kaveh Ahadi, William M. Strickland, Salva Salmani-Rezaie, and Susanne Stemmer. Possible signatures of mixed-parity superconductivity in doped polar $SrTiO_3$ films. *Physical Review B*, 101(10):100503, March 2020.

[31] M. D. Johannes and I. I. Mazin. Fermi surface nesting and the origin of charge density waves in metals. *Phys. Rev. B*, 77:165135, Apr 2008.

[32] Leon Balents. Spin liquids in frustrated magnets. *Nature*, 464(7286):199–208, March 2010.

[33] Jinsheng Wen, Shun-Li Yu, Shiyan Li, Weiqiang Yu, and Jian-Xin Li. Experimental identification of quantum spin liquids. *npj Quantum Materials*, 4(1):1–9, April 2019.

[34] David S. Sholl and Janice A. Steckel. *Density Functional Theory: A Practical Introduction*. Wiley, 1 edition, March 2009.

[35] P. Hohenberg and W. Kohn. Inhomogeneous Electron Gas. *Physical Review*, 136(3B):B864–B871, November 1964.

[36] R. LeSar. *Introduction to Computational Materials Science: Fundamentals to Applications*. Cambridge University Press, Cambridge ; New York, 2013.

[37] Nicholas Metropolis, Arianna W. Rosenbluth, Marshall N. Rosenbluth, Augusta H. Teller, and Edward Teller. Equation of State Calculations by Fast Computing Machines. *The Journal of Chemical Physics*, 21(6):1087–1092, June 1953.

[38] V. Goian, S. Kamba, J. Hlinka, P. Vaněk, A. A. Belik, T. Kolodiazhnyi, and J. Petzelt. Polar phonon mixing in magnetoelectric $EuTiO_3$. *The European Physical Journal B*, 71(3):429–433, October 2009.

[39] Maria N. Gastiasoro, Jonathan Ruhman, and Rafael M. Fernandes. Superconductivity in dilute $SrTiO_3$: A review. *Annals of Physics*, 417:168107, June 2020.

[40] J. Appel. Soft-Mode Superconductivity in $SrTiO_{3-x}$. *Physical Review*, 180(2):508–516, April 1969.

[41] J H Haeni, P Irvin, W Chang, R Uecker, P Reiche, Y L Li, S Choudhury, W Tian, M E Hawley, B Craigo, A K Tagantsev, X Q Pan, S K Streiffer, L Q Chen, S W Kirchoefer, J Levy, and D G Schlom. Room-temperature ferroelectricity in strained $SrTiO_3$. *Nature*, 430:4, 2004.

[42] Ryan Russell, Noah Ratcliff, Kaveh Ahadi, Lianyang Dong, Susanne Stemmer, and John W. Harter. Ferroelectric enhancement of superconductivity in compressively strained $SrTiO_3$ films. *Physical Review Materials*, 3(9):091401, September 2019.

[43] Ruijuan Xu, Jiawei Huang, Edward S. Barnard, Seung Sae Hong, Prastuti Singh, Ed K. Wong, Thies Jansen, Varun Harbola, Jun Xiao, Bai Yang Wang, Sam Crossley, Di Lu, Shi Liu, and Harold Y. Hwang. Strain-induced room-temperature ferroelectricity in $SrTiO_3$ membranes. *Nature Communications*, 11(1):3141, December 2020.

[44] S. Hameed, D. Pelc, Z. W. Anderson, A. Klein, R. J. Spieker, L. Yue, B. Das, J. Ramberger, M. Lukas, Y. Liu, M. J. Krogstad, R. Osborn, Y. Li, C. Leighton, R. M. Fernandes, and M. Greven. Enhanced superconductivity and ferroelectric quantum criticality in plastically deformed strontium titanate. *Nature Materials*, 21(1):54–61, January 2022.

[45] M. Itoh, R. Wang, Y. Inaguma, T. Yamaguchi, Y-J. Shan, and T. Nakamura. Ferroelectricity Induced by Oxygen Isotope Exchange in Strontium Titanate Perovskite. *Physical Review Letters*, 82(17):3540–3543, April 1999.

[46] Carl Willem Rischau, Xiao Lin, Christoph P. Grams, Dennis Finck, Steffen Harms, Johannes Engelmayer, Thomas Lorenz, Yann Gallais, Benoît Fauqué, Joachim Hemberger, and Kamran Behnia. A ferroelectric quantum phase transition inside the superconducting dome of $Sr_{1-x}Ca_xTiO_{3-\delta}$. *Nature Physics*, 13(7):643–648, July 2017.

[47] Johannes Engelmayer, Xiao Lin, Fulya Koç, Christoph P. Grams, Joachim Hemberger, Kamran Behnia, and Thomas Lorenz. Ferroelectric order versus metallicity in $Sr_{1-x}Ca_xTiO_{3-\delta}$ (x = 0.009). *Physical Review B*, 100(19):195121, November 2019.

[48] Xian Li, Tian Qiu, Jiahao Zhang, Edoardo Baldini, Jian Lu, Andrew M. Rappe, and Keith A. Nelson. Terahertz field–induced ferroelectricity in quantum paraelectric $SrTiO_3$. *Science*, 364(6445):1079–1082, June 2019.

[49] T. F. Nova, A. S. Disa, M. Fechner, and A. Cavalleri. Metastable ferroelectricity in optically strained $SrTiO_3$. *Science*, 364(6445):1075–1079, June 2019.

[50] D. Lee, H. Lu, Y. Gu, S.-Y. Choi, S.-D. Li, S. Ryu, T. R. Paudel, K. Song, E. Mikheev, S. Lee, S. Stemmer, D. A. Tenne, S. H. Oh, E. Y. Tsymbal, X. Wu, L.-Q. Chen, A. Gruverman, and C. B. Eom. Emergence of room-temperature ferroelectricity at reduced dimensions. *Science*, 349(6254):1314–1317, September 2015.

[51] Dilpuneet S. Aidhy and Kanishk Rawat. Coupling between interfacial strain and oxygen vacancies at complex-oxides interfaces. *Journal of Applied Physics*, 129(17):171102, May 2021.

[52] A. Stucky, G. W. Scheerer, Z. Ren, D. Jaccard, J.-M. Poumirol, C. Barreteau, E. Giannini, and D. van der Marel. Isotope effect in superconducting n-doped $SrTiO_3$. *Scientific Reports*, 6(1):37582, December 2016.

[53] C. W. Rischau, D. Pulmannová, G. W. Scheerer, A. Stucky, E. Giannini, and D. van der Marel. Isotope tuning of the superconducting dome of strontium titanate. *Physical Review Research*, 4(1):013019, January 2022.

[54] F.C. Sa Barreto. Ferroelectric Phase Transitions and the Ising Model. *Brazilian Journal of Physics*, 30(4):778–781, December 2000.

[55] Stamenkovic, S. The Unified Model Description of Order-Disorder and Displacive Structural Phase Transitions. *Condensed Matter Physics*, 1(2):257, 1998.

[56] M. Takesada, M. Itoh, and T. Yagi. Perfect Softening of the Ferroelectric Mode in the Isotope-Exchanged Strontium Titanate of $SrTi^{18}O_3$ Studied by Light Scattering. *Physical Review Letters*, 96(22):227602, June 2006.

[57] Takeshi Shigenari, Kohji Abe, Keiji Yamashita, Tomohiko Takemoto, Ruiping Wang, and Mitsuru Itoh. Raman Spectra of Ferroelectric Soft Mode in $SrTiO_3$: Effect of Electric Field. *Ferroelectrics*, 285(1):41–48, January 2003.

[58] Hiromoto Uwe and Tunetaro Sakudo. Stress-induced ferroelectricity and soft phonon modes in $SrTiO_3$. *Physical Review B*, 13(1):271–286, January 1976.

[59] R. A. Cowley. Temperature Dependence of a Transverse Optic Mode in Strontium Titanate. *Physical Review Letters*, 9(4):159–161, August 1962.

[60] Yasusada Yamada and Gen Shirane. Neutron Scattering and Nature of the Soft Optical Phonon in $SrTiO_3$. *Journal of the Physical Society of Japan*, 26(2):396–403, February 1969.

[61] G. Shirane and Y. Yamada. Lattice-Dynamical Study of the 110°K Phase Transition in $SrTiO_3$. *Physical Review*, 177(2):858–863, January 1969.

[62] A. S. Barker. Temperature Dependence of the Transverse and Longitudinal Optic Mode Frequencies and Charges in $SrTiO_3$ and $BaTiO_3$. *Physical Review*, 145(2):391–399, May 1966.

[63] Kuon Inoue. Study of structural phase transitions by the hyper-Raman scattering. *Ferroelectrics*, 52(1):253–262, December 1983.

[64] H. Vogt. Refined treatment of the model of linearly coupled anharmonic oscillators and its application to the temperature dependence of the zone-center soft-mode frequencies of $KTaO_3$ and $SrTiO_3$. *Physical Review B*, 51(13):8046–8059, April 1995.

[65] A Yamanaka, M Kataoka, Y Inaba, K Inoue, B Hehlen, and E Courtens. Evidence for competing orderings in strontium titanate from hyper-Raman scattering spectroscopy. *Europhysics Letters (EPL)*, 50(5):688–694, June 2000.

[66] R. Migoni, H. Bilz, and D. Bäuerle. Origin of Raman Scattering and Ferroelectricity in Oxidic Perovskites. *Physical Review Letters*, 37(17):1155–1158, October 1976.

[67] Dongbin Shin, Simone Latini, Christian Schäfer, Shunsuke A. Sato, Umberto De Giovannini, Hannes Hübener, and Angel Rubio. Quantum paraelectric phase of $SrTiO_3$ from first principles. *Physical Review B*, 104(6):L060103, August 2021.

[68] T. Ostapchuk, J. Petzelt, V. Železný, A. Pashkin, J. Pokorný, I. Drbohlav, R. Kužel, D. Rafaja, B. P. Gorshunov, M. Dressel, Ch. Ohly, S. Hoffmann-Eifert, and R. Waser. Origin of soft-mode stiffening and reduced dielectric response in $SrTiO_3$ thin films. *Physical Review B*, 66(23):235406, December 2002.

[69] I. A. Akimov, A. A. Sirenko, A. M. Clark, J.-H. Hao, and X. X. Xi. Electric-Field-Induced Soft-Mode Hardening in $SrTiO_3$ Films. *Physical Review Letters*, 84(20):4625–4628, May 2000.

[70] A Sirenko, C Bernhard, A Golnik, Anna M Clark, Jianhua Hao, Weidong Si, and X Xi. Soft-mode hardening in $SrTiO_3$ thin films. *Nature*, 404:4, 2000.

[71] Ikufumi Katayama, Hiroshi Shimosato, Dhanvir Singh Rana, Iwao Kawayama, Masayoshi Tonouchi, and Masaaki Ashida. Hardening of the ferroelectric soft mode in $SrTiO_3$ thin films. *Applied Physics Letters*, 93(13):132903, September 2008.

[72] D. Bäuerle, D. Wagner, M. Wöhlecke, B. Dorner, and H. Kraxenberger. Soft modes in semiconducting $SrTiO_3$: II. The ferroelectric mode. *Zeitschrift für Physik B Condensed Matter*, 38(4):335–339, December 1980.

[73] A. Bussmann-Holder, H. Bilz, D. Buerle, and D. Wagner. A polarizability model for the ferroelectric mode in semiconducting $SrTiO_3$. *Zeitschrift fr Physik B Condensed Matter*, 41(4):353–355, December 1981.

[74] Annette Bussmann-Holder, Hugo Keller, Arndt Simon, Gustav Bihlmayer, Krystian Roleder, and Krzysztof Szot. Unconventional Co-Existence of Insulating Nano-Regions and Conducting Filaments in Reduced $SrTiO_3$: Mode Softening, Local Piezoelectricity, and Metallicity. *Crystals*, 10(6):437, May 2020.

[75] J. R. Arce-Gamboa and G. G. Guzmán-Verri. Quantum ferroelectric instabilities in superconducting $SrTiO_3$. *Physical Review Materials*, 2(10):104804, October 2018.

[76] D Nuzhnyy, J Petzelt, S Kamba, X Martí, T Čechal, C M Brooks, and D G Schlom. Infrared phonon spectroscopy of a compressively strained (001) $SrTiO_3$ film grown on a (110) $NdGaO_3$ substrate. *Journal of Physics: Condensed Matter*, 23(4):045901, February 2011.

[77] S E Rowley, C Enderlein, J Ferreira de Oliveira, D A Tompsett, Baggio Saitovitch, S S Saxena, and G G Lonzarich. Superconductivity in the vicinity of a ferroelectric quantum phase transition. *arXiv:1801.08121*, January 2018.

[78] C. Enderlein, J. Ferreira de Oliveira, D. A. Tompsett, E. Baggio Saitovitch, S. S. Saxena, G. G. Lonzarich, and S. E. Rowley. Superconductivity mediated by polar modes in ferroelectric metals. *Nature Communications*, 11(1):4852, December 2020.

[79] E Courtens, G Coddens, B Hennion, B Hehlen, J Pelous, and R Vacher. Phonon anomalies in $SrTiO_3$ in the quantum paraelectric regime. *Physica Scripta*, T49B:430–435, January 1993.

[80] Leejun Kim, Juho Kim, Jaichan Lee, and Donggeun Jung. Optical phonon softening in strained $SrTiO_3$ thin film: First-principles study. *Applied Physics Letters*, 85(23):5649–5651, December 2004.

[81] Sebastian E. Reyes-Lillo, Karin M. Rabe, and Jeffrey B. Neaton. Ferroelectricity in [111]-oriented epitaxially strained $SrTiO_3$ from first principles. *Physical Review Materials*, 3(3):030601, March 2019.

[82] Woon Ih Choi, Jae Sik An, Inkook Jang, and Dae Sin Kim. Strain and temperature-dependent dielectric permittivity of cubic $SrTiO_3$: Self-consistent phonon theory calculations. *Current Applied Physics*, 29:78–82, September 2021.

[83] Seiji Kojima. Correlation between Soft Mode Frequency and Carrier Concentration in Doped Strontium Titanate Crystals. In *2021 IEEE International Symposium on Applications of Ferroelectrics (ISAF)*, pages 1–4, Sydney, Australia, May 2021. IEEE.

[84] W. Kleemann and H. Schremmer. Cluster and domain-wall dynamics of ferroelectric $Sr_{1-x}Ca_xTiO_3$. *Physical Review B*, 40(10):7428–7431, October 1989.

[85] W. Kleemann, A. Albertini, M. Kuss, and R. Lindner. Optical detection of symmetry breaking on a nanoscale in $SrTiO_3$:Ca. *Ferroelectrics*, 203(1):57–74, November 1997.

[86] E. L. Venturini. Pressure As A Probe Of The Physics Of Compositionally-Substituted Quantum Paraelectrics: $SrTiO_3$. In *AIP Conference Proceedings*, volume 677, pages 1–9, Williamsburg, Virginia (USA), 2003. AIP.

[87] U. Bianchi, J. Dec, W. Kleemann, and J. G. Bednorz. Cluster and domain-state dynamics of ferroelectric $Sr_{1-x}Ca_x$ TiO_3 (x=0.007). *Physical Review B*, 51(14):8737–8746, April 1995.

[88] W Kleemann, A Albertini, R. V Chamberlin, and J. G Bednorz. Relaxational dynamics of polar nanodomains in $Sr_{1-x}Ca_xTiO_3$ $x = 0.002$. *Europhysics Letters (EPL)*, 37(2):145–150, January 1997.

[89] Robert Blinc. Disorder in BaTiO3 and $SrTiO_3$ and the "Ferroelectric" Transition in SrTi18O3. In *AIP Conference Proceedings*, volume 677, pages 20–25, Williamsburg, Virginia (USA), 2003. AIP.

[90] R Blinc, V V Laguta, B Zalar, M Itoh, and H Krakauer. ^{17}O quadrupole coupling and the origin of ferroelectricity in isotopically enriched $BaTiO_3$ and $SrTiO_3$. *Journal of Physics: Condensed Matter*, 20(8):085204, February 2008.

[91] Alexander K. Tagantsev, Eric Courtens, and Ludovic Arzel. Prediction of a low-temperature ferroelectric instability in antiphase domain boundaries of strontium titanate. *Physical Review B*, 64(22):224107, November 2001.

[92] A. Vasudevarao, A. Kumar, L. Tian, J. H. Haeni, Y. L. Li, C.-J. Eklund, Q. X. Jia, R. Uecker, P. Reiche, K. M. Rabe, L. Q. Chen, D. G. Schlom, and Venkatraman Gopalan. Multiferroic Domain Dynamics in Strained Strontium Titanate. *Physical Review Letters*, 97(25):257602, December 2006.

[93] Salva Salmani-Rezaie, Kaveh Ahadi, and Susanne Stemmer. Polar Nanodomains in a Ferroelectric Superconductor. *Nano Letters*, 20(9):6542–6547, September 2020.

[94] Salva Salmani-Rezaie, Honggyu Kim, Kaveh Ahadi, and Susanne Stemmer. Lattice relaxations around individual dopant atoms in $SrTiO_3$. *Physical Review Materials*, 3(11):114404, November 2019.

[95] Salva Salmani-Rezaie, Hanbyeol Jeong, Ryan Russell, John W. Harter, and Susanne Stemmer. Role of locally polar regions in the superconductivity of $SrTiO_3$. *Physical Review Materials*, 5(10):104801, October 2021.

[96] G. Sheng, Y. L. Li, J. X. Zhang, S. Choudhury, Q. X. Jia, V. Gopalan, D. G. Schlom, Z. K. Liu, and L. Q. Chen. A modified Landau–Devonshire thermodynamic potential for strontium titanate. *Applied Physics Letters*, 96(23):232902, June 2010.

[97] Alex Hallett and John W Harter. Modeling polar order in compressively strained $SrTiO_3$. *PHYSICAL REVIEW B*, 2022.

[98] G. Kresse and J. Hafner. *Ab Initio* molecular dynamics for liquid metals. *Physical Review B*, 47(1):558–561, January 1993.

[99] G. Kresse and J. Furthmüller. Efficient iterative schemes for *ab initio* total-energy calculations using a plane-wave basis set. *Physical Review B*, 54(16):11169–11186, October 1996.

[100] G. Kresse and J. Furthmüller. Efficiency of ab-initio total energy calculations for metals and semiconductors using a plane-wave basis set. *Computational Materials Science*, 6(1):15–50, July 1996.

[101] G. Kresse and D. Joubert. From ultrasoft pseudopotentials to the projector augmented-wave method. *Physical Review B*, 59(3):1758–1775, January 1999.

[102] John P. Perdew, Kieron Burke, and Matthias Ernzerhof. Generalized Gradient Approximation Made Simple. *Physical Review Letters*, 77(18):3865–3868, October 1996.

[103] Atsushi Togo and Isao Tanaka. First principles phonon calculations in materials science. *Scripta Materialia*, 108:1–5, November 2015.

[104] Harold T Stokes, D.M. Hatch, and B.J. Campbell. ISOTROPY Software Suite.

[105] Dorian M Hatch and Harold T Stokes. INVARIANTS: Program for obtaining a list of invariant polynomials of the order parameter components associated with irreducible representations of a space group. page 2.

[106] Fabien Tran, Julia Stelzl, and Peter Blaha. Rungs 1 to 4 of DFT Jacob's ladder: Extensive test on the lattice constant, bulk modulus, and cohesive energy of solids. *The Journal of Chemical Physics*, 144(20):204120, May 2016.

[107] Tomoaki Yamada, Benjamin Wylie-van Eerd, Osami Sakata, Alexander K. Tagantsev, Hitoshi Morioka, Yoshitaka Ehara, Shintaro Yasui, Hiroshi Funakubo, Takanori Nagasaki, and H. J. Trodahl. Phase transitions associated with competing order parameters in compressively strained $SrTiO_3$ thin films. *Physical Review B*, 91(21):214101, June 2015.

[108] Ri He, Hongyu Wu, Linfeng Zhang, Xiaoxu Wang, Fangjia Fu, Shi Liu, and Zhicheng Zhong. Structural phase transitions in $SrTiO_3$ from deep potential molecular dynamics. *Physical Review B*, 105(6):064104, February 2022.

[109] T. Yamada, T. Kiguchi, A. K. Tagantsev, H. Morioka, T. Iijima, H. Ohsumi, S. Kimura, M. Osada, N. Setter, and H. Funakubo. Antiferrodistortive Structural Phase Transition in Compressively-Strained Epitaxial $SrTiO_3$ Film Grown on (La, Sr)(Al, Ta)O_3 Substrate. *Integrated Ferroelectrics*, 115(1):57–62, November 2010.

[110] Arpita Paul, Jianwei Sun, John P. Perdew, and Umesh V. Waghmare. Accuracy of first-principles interatomic interactions and predictions of ferroelectric phase transitions in perovskite oxides: Energy functional and effective Hamiltonian. *Physical Review B*, 95(5):054111, February 2017.

[111] W. Zhong, David Vanderbilt, and K. M. Rabe. First-principles theory of ferroelectric phase transitions for perovskites: The case of $BaTiO_3$. *Physical Review B*, 52(9):6301–6312, September 1995.

[112] Stamenkovic. THE UNIFIED MODEL DESCRIPTION OF ORDER-DISORDER AND DISPLACIVE STRUCTURAL PHASE TRANSITIONS. *Condensed Matter Physics*, 1(2):257, 1998.

[113] Salva Salmani-Rezaie, Kaveh Ahadi, William M. Strickland, and Susanne Stemmer. Order-Disorder Ferroelectric Transition of Strained $SrTiO_3$. *Physical Review Letters*, 125(8):087601, August 2020.

[114] Guomin Zhu, Alex Hallett, Nicholas G. Combs, Hanbyeol Jeong, Arda Genc, John W. Harter, and Susanne Stemmer. Coexistence of antiferrodistortive and polar order in a superconducting $SrTiO_3$ film. *Phys. Rev. Mater.*, 8:L051801, May 2024.

[115] Hanbyeol Jeong, Ryan Russell, Nicholas G. Combs, Tyler N. Pardue, John W. Harter, and Susanne Stemmer. Similarity in the critical thicknesses for superconductivity and ferroelectricity in strained $SrTiO_3$ films. *Applied Physics Letters*, 121(1):012601, July 2022.

[116] Feizhou He, B. O. Wells, and S. M. Shapiro. Strain phase diagram and domain orientation in $SrTiO_3$ thin films. *Phys. Rev. Lett.*, 94:176101, May 2005.

[117] Kaveh Ahadi, Luca Galletti, Yuntian Li, Salva Salmani-Rezaie, Wangzhou Wu, and Susanne Stemmer. Enhancing superconductivity in $SrTiO_3$ films with strain. *Science Advances*, 5(4):eaaw0120, April 2019.

[118] Yasuhide Tomioka, Naoki Shirakawa, Keisuke Shibuya, and Isao H. Inoue. Enhanced superconductivity close to a non-magnetic quantum critical point in electron-doped strontium titanate. *Nature Communications*, 10(1):738, February 2019.

[119] Qian Tao, Bastien Loret, Bin Xu, Xiaojun Yang, Willem Rischau, Xiao Lin, Benoît Fauqué, Matthieu J. Verstraete, and Kamran Behnia. Non-monotonic anisotropy in charge conduction induced by antiferrodistortive transition in metallic $SrTiO_3$. *Physical Review B*, 94(3):035111, July 2016.

[120] Julien Varignon. Unexpected competition between ferroelectricity and rashba effects in epitaxially strained $SrTiO_3$. *Phys. Rev. Lett.*, 132:106401, Mar 2024.

[121] Xiao Lin, Zengwei Zhu, Benoît Fauqué, and Kamran Behnia. Fermi surface of the most dilute superconductor. *Phys. Rev. X*, 3:021002, Apr 2013.

[122] S. James Allen, Bharat Jalan, SungBin Lee, Daniel G. Ouellette, Guru Khalsa, Jan Jaroszynski, Susanne Stemmer, and Allan H. MacDonald. Conduction-band edge and shubnikov–de haas effect in low-electron-density $SrTiO_3$. *Phys. Rev. B*, 88:045114, Jul 2013.

[123] A. Spinelli, M. A. Torija, C. Liu, C. Jan, and C. Leighton. Electronic transport in doped $SrTiO_3$: Conduction mechanisms and potential applications. *Phys. Rev. B*, 81:155110, Apr 2010.

[124] Xiao Lin, Adrien Gourgout, German Bridoux, François Jomard, Alexandre Pourret, Benoît Fauqué, Dai Aoki, and Kamran Behnia. Multiple nodeless superconducting gaps in optimally doped $SrTi_{1-x}$ Nb_xO_3. *Physical Review B*, 90(14):140508, October 2014.

[125] Xiao Lin, Carl Willem Rischau, Lisa Buchauer, Alexandre Jaoui, Benoît Fauqué, and Kamran Behnia. Metallicity without quasi-particles in room-temperature strontium titanate. *npj Quantum Materials*, 2(1):41, December 2017.

[126] Searle A. Jain A. Griffin S. M. Ganose, A. M. Ifermi: A python library for fermi surface generation and analysis. *Journal of Open Source Software*, 6(59):3089, 2021.

[127] V.L. Gurevich, A.I. Larkin, and Yu. A. Firsov. On the possibility of superconductivity in semiconductors. 4(1):185–190, July 1962.

[128] K. L. Ngai. Two-Phonon Deformation Potential and Superconductivity in Degenerate Semiconductors. *Physical Review Letters*, 32(5):215–218, February 1974.

[129] Isaaki Yokota. On the Coupling between Optical Lattice Vibrations and Carrier Plasma Oscillations in Polar Semiconductors. *Journal of the Physical Society of Japan*, 16(10):2075–2075, October 1961.

[130] Yasutami Takada. Plasmon Mechanism of Superconductivity in Two- and Three-Dimensional Electron Systems. *Journal of the Physical Society of Japan*, 45(3):786–794, September 1978.

[131] Maria N. Gastiasoro, Andrey V. Chubukov, and Rafael M. Fernandes. Phonon-mediated superconductivity in low carrier-density systems. *Physical Review B*, 99(9):094524, March 2019.

[132] Jonathan Ruhman and Patrick A. Lee. Superconductivity at very low density: The case of strontium titanate. *Physical Review B*, 94(22):224515, December 2016.

[133] S. N. Klimin, J. Tempere, J. T. Devreese, J. He, C. Franchini, and G. Kresse. Superconductivity in $SrTiO_3$: Dielectric Function Method for Non-Parabolic Bands. *Journal of Superconductivity and Novel Magnetism*, 32(9):2739–2744, September 2019.

[134] J. T. Devreese, S. N. Klimin, J. L. M. van Mechelen, and D. van der Marel. Many-body large polaron optical conductivity in $SrTi_{1-x}Nb_xO_3$. *Phys. Rev. B*, 81:125119, Mar 2010.

[135] Marvin L. Cohen. Superconductivity in Many-Valley Semiconductors and in Semimetals. *Physical Review*, 134(2A):A511–A521, April 1964.

[136] C. S. Koonce, Marvin L. Cohen, J. F. Schooley, W. R. Hosler, and E. R. Pfeiffer. Superconducting Transition Temperatures of Semiconducting $SrTiO_3$. *Physical Review*, 163(2):380–390, November 1967.

[137] L. F. Mattheiss. Energy Bands for $KNiF_3$, $SrTiO_3$, $KMoO_3$, and $KTaO_3$. *Physical Review B*, 6(12):4718–4740, December 1972.

[138] Dmitry Kiseliov and Mikhail Feigelman. Theory of superconductivity due to Ngai's mechanism in lightly doped $SrTiO_3$, July 2021.

[139] Vladimir A. Zyuzin and Alexander A. Zyuzin. Anisotropic resistivity and superconducting instability in ferroelectric-like metals, January 2022.

[140] Lev P. Gor'kov. Phonon mechanism in the most dilute superconductor n-type $SrTiO_3$. *Proceedings of the National Academy of Sciences*, 113(17):4646–4651, April 2016.

[141] Peter Wölfle and Alexander V. Balatsky. Superconductivity at low density near a ferroelectric quantum critical point: Doped $SrTiO_3$. *Physical Review B*, 98(10):104505, September 2018.

[142] Pavel A. Volkov and Premala Chandra. Multiband Quantum Criticality of Polar Metals. *Physical Review Letters*, 124(23):237601, June 2020.

[143] Pavel A. Volkov, Premala Chandra, and Piers Coleman. Superconductivity from energy fluctuations in dilute quantum critical polar metals, June 2021.

[144] Maria N. Gastiasoro, Maria Eleonora Temperini, Paolo Barone, and Jose Lorenzana. Theory of superconductivity mediated by Rashba coupling in incipient ferroelectrics. *Physical Review B*, 105(22):224503, June 2022.

[145] Jin Yue, Yilikal Ayino, Tristan K. Truttmann, Maria N. Gastiasoro, Eylon Persky, Alex Khanukov, Dooyong Lee, Laxman R. Thoutam, Beena Kalisky, Rafael M. Fernandes, Vlad S. Pribiag, and Bharat Jalan. Anomalous Transport in High-Mobility Superconducting $SrTiO_3$ Thin Films. (arXiv:2107.10904), July 2021.

[146] Hyeok Yoon, Adrian G. Swartz, Shannon P. Harvey, Hisashi Inoue, Yasuyuki Hikita, Yue Yu, Suk Bum Chung, Srinivas Raghu, and Harold Y. Hwang. Low-density superconductivity in $SrTiO_3$ bounded by the adiabatic criterion, June 2021.

[147] D. van der Marel, J. L. M. van Mechelen, and I. Mazin. Common Fermi-liquid origin of T^2 resistivity and superconductivity in n-type $SrTiO_3$. *Physical Review B*, 84(20):205111, November 2011.

[148] S. N. Klimin, J. Tempere, D. van der Marel, and J. T. Devreese. Microscopic mechanisms for the Fermi-liquid behavior of Nb-doped strontium titanate. *Phys. Rev. B*, 86:045113, Jul 2012.

[149] Shota Kanasugi and Youichi Yanase. Spin-orbit-coupled ferroelectric superconductivity. *Physical Review B*, 98(2):024521, July 2018.

[150] Shota Kanasugi and Youichi Yanase. Multiorbital ferroelectric superconductivity in doped $SrTiO_3$. *Physical Review B*, 100(9):094504, September 2019.

[151] Sergei Urazhdin, Ekram Towsif, and Alexander Mitrofanov. Effects of spin-orbit interaction and electron correlations in strontium titanate. *arXiv:2201.04184*, March 2022.

[152] Terence M. Bretz-Sullivan, Alexander Edelman, J. S. Jiang, Alexey Suslov, David Graf, Jianjie Zhang, Gensheng Wang, Clarence Chang, John E. Pearson, Alex B. Martinson, Peter B. Littlewood, and Anand Bhattacharya. Superconductivity in the dilute single band limit in reduced Strontium Titanate. (arXiv:1904.03121), September 2019.

[153] K. Rogacki G. Bihlmayer W. Speier K. Roleder F. Krok H. Keller A. Simon A. Bussmann-Holder K. Szot, C. Rodenbücher. Filamentary superconductivity of resistively-switched strontium titanate, October 2021.

[154] S. E. Rowley, L. J. Spalek, R. P. Smith, M. P. M. Dean, M. Itoh, J. F. Scott, G. G. Lonzarich, and S. S. Saxena. Ferroelectric quantum criticality. *Nature Physics*, 10(5):367–372, May 2014.

[155] Pavel A. Volkov, Premala Chandra, and Piers Coleman. Superconductivity from energy fluctuations in dilute quantum critical polar metals. *Nature Communications*, 13(1):4599, August 2022.

[156] Sungkit Yip. Noncentrosymmetric Superconductors. *Annual Review of Condensed Matter Physics*, 5(1):15–33, March 2014.

[157] Salva Salmani-Rezaie, Luca Galletti, Timo Schumann, Ryan Russell, Hanbyeol Jeong, Yuntian Li, John W. Harter, and Susanne Stemmer. Superconductivity in magnetically doped $SrTiO_3$. *Applied Physics Letters*, 118(20):202602, May 2021.

[158] Yue Yu, Harold Y. Hwang, S. Raghu, and Suk Bum Chung. Theory of superconductivity in doped quantum paraelectrics. *npj Quantum Materials*, 7(1):63, December 2022.

[159] Maria N. Gastiasoro, Maria Eleonora Temperini, Paolo Barone, and José Lorenzana. Generalized Rashba electron-phonon coupling and superconductivity in strontium titanate. *Physical Review Research*, 5(2):023177, June 2023.

[160] Alex Hallett, Catalina Avarvarei, and John W. Harter. Combinatorial exploration of quantum spin liquid candidates in the herbertsmithite material family. *Physical Review Materials*, 7(6):064403, June 2023.

[161] Lucile Savary and Leon Balents. Quantum spin liquids: A review. *Reports on Progress in Physics*, 80(1):016502, November 2016.

[162] C. Broholm, R. J. Cava, S. A. Kivelson, D. G. Nocera, M. R. Norman, and T. Senthil. Quantum spin liquids. *Science*, 367(6475):eaay0668, January 2020.

[163] G. Semeghini, H. Levine, A. Keesling, S. Ebadi, T. T. Wang, D. Bluvstein, R. Verresen, H. Pichler, M. Kalinowski, R. Samajdar, A. Omran, S. Sachdev, A. Vishwanath, M. Greiner, V. Vuletić, and M. D. Lukin. Probing topological spin liquids on a programmable quantum simulator. *Science*, 374(6572):1242–1247, December 2021.

[164] Philippe Mendels and Fabrice Bert. Quantum Kagome Antiferromagnet $ZnCu_3(OH)_6Cl_2$. *Journal of the Physical Society of Japan*, 79(1):011001, January 2010.

[165] M. R. Norman. Colloquium: Herbertsmithite and the search for the quantum spin liquid. *Reviews of Modern Physics*, 88(4):041002, December 2016.

[166] Matthew P. Shores, Emily A. Nytko, Bart M. Bartlett, and Daniel G. Nocera. A Structurally Perfect S = 1/2 Kagomé Antiferromagnet. *Journal of the American Chemical Society*, 127(39):13462–13463, October 2005.

[167] M. A. de Vries, J. R. Stewart, P. P. Deen, J. O. Piatek, G. J. Nilsen, H. M. Rønnow, and A. Harrison. Scale-Free Antiferromagnetic Fluctuations in the s = 1 / 2 Kagome Antiferromagnet Herbertsmithite. *Physical Review Letters*, 103(23):237201, December 2009.

[168] T. H. Han, J. S. Helton, S. Chu, A. Prodi, D. K. Singh, C. Mazzoli, P. Müller, D. G. Nocera, and Y. S. Lee. Synthesis and characterization of single crystals of the spin-1/2 kagome-lattice antiferromagnets $Zn_xCu_{4-x}(OH)_6Cl_2$. *Physical Review B*, 83(10):100402, March 2011.

[169] J. S. Helton, K. Matan, M. P. Shores, E. A. Nytko, B. M. Bartlett, Y. Yoshida, Y. Takano, A. Suslov, Y. Qiu, J.-H. Chung, D. G. Nocera, and Y. S. Lee. Spin Dynamics of the Spin-1/2 Kagome Lattice Antiferromagnet $ZnCu_3(OH)_6Cl_2$. *Physical Review Letters*, 98(10):107204, March 2007.

[170] P. Mendels, F. Bert, M. A. de Vries, A. Olariu, A. Harrison, F. Duc, J. C. Trombe, J. S. Lord, A. Amato, and C. Baines. Quantum Magnetism in the Paratacamite Family: Towards an Ideal KagomeLattice. *Physical Review Letters*, 98(7):077204, February 2007.

[171] Mingxuan Fu, Takashi Imai, Tian-Heng Han, and Young S. Lee. Evidence for a gapped spin-liquid ground state in a kagome Heisenberg antiferromagnet. *Science*, 350(6261):655–658, November 2015.

[172] Tian-Heng Han, M. R. Norman, J.-J. Wen, Jose A. Rodriguez-Rivera, Joel S. Helton, Collin Broholm, and Young S. Lee. Correlated impurities and intrinsic spin-liquid physics in the kagome material herbertsmithite. *Physical Review B*, 94(6):060409, August 2016.

[173] A. Olariu, P. Mendels, F. Bert, F. Duc, J. C. Trombe, M. A. de Vries, and A. Harrison. ^{17}O NMR Study of the Intrinsic Magnetic Susceptibility and Spin Dynamics of the Quantum Kagome Antiferromagnet $ZnCu_3(OH)_6Cl_2$. *Physical Review Letters*, 100(8):087202, February 2008.

[174] Tian-Heng Han, Joel S. Helton, Shaoyan Chu, Daniel G. Nocera, Jose A. Rodriguez-Rivera, Collin Broholm, and Young S. Lee. Fractionalized excitations in the spin-liquid state of a kagome-lattice antiferromagnet. *Nature*, 492(7429):406–410, December 2012.

[175] Dirk Wulferding, Peter Lemmens, Patric Scheib, Jens Röder, Philippe Mendels, Shaoyan Chu, Tianheng Han, and Young S. Lee. Interplay of thermal and quantum spin fluctuations in the kagome lattice compound herbertsmithite. *Physical Review B*, 82(14):144412, October 2010.

[176] M. A. de Vries, K. V. Kamenev, W. A. Kockelmann, J. Sanchez-Benitez, and A. Harrison. Magnetic Ground State of an Experimental S=1/2 Kagome Antiferromagnet. *Physical Review Letters*, 100(15):157205, April 2008.

[177] P. Khuntia, M. Velazquez, Q. Barthélemy, F. Bert, E. Kermarrec, A. Legros, B. Bernu, L. Messio, A. Zorko, and P. Mendels. Gapless ground state in the archetypal quantum kagome antiferromagnet $ZnCu_3(OH)_6Cl_2$. *Nature Physics*, 16(4):469–474, April 2020.

[178] Oren Ofer, Amit Keren, Jess H. Brewer, Tianheng H. Han, and Young S. Lee. The Herbertsmithite Hamiltonian: μSR measurements on single crystals. *Journal of Physics: Condensed Matter*, 23(16):164207, April 2011.

[179] Harald O. Jeschke, Francesc Salvat-Pujol, and Roser Valenti. First-principles determination of Heisenberg Hamiltonian parameters for the spin-1/2 kagome antiferromagnet $ZnCu_3(OH)_6Cl_2$. *Physical Review B*, 88(7):075106, August 2013.

[180] Raik Suttner, Christian Platt, Johannes Reuther, and Ronny Thomale. Renormalization group analysis of competing quantum phases in the J_1-J_2 Heisenberg model on the kagome lattice. *Physical Review B*, 89(2):020408, January 2014.

[181] Oleg Janson. DFT-based microscopic magnetic modeling for low-dimensional spin systems. page 223.

[182] Marcos Rigol and Rajiv R. P. Singh. Magnetic Susceptibility of the Kagome Antiferromagnet$ZnCu_3(OH)_6Cl_2$. *Physical Review Letters*, 98(20):207204, May 2007.

[183] Oliver Götze and Johannes Richter. The route to magnetic order in the spin-1/2 kagome Heisenberg antiferromagnet: The role of interlayer coupling. *EPL (Europhysics Letters)*, 114(6):67004, June 2016.

[184] Ying Li, A. Pustogow, M. Bories, P. Puphal, C. Krellner, M. Dressel, and Roser Valentí. Lattice dynamics in the spin-1/2 frustrated kagome compound herbertsmithite. *Physical Review B*, 101(16):161115, April 2020.

[185] Danna E. Freedman, Tianheng H. Han, Andrea Prodi, Peter Müller, Qing-Zhen Huang, Yu-Sheng Chen, Samuel M. Webb, Young S. Lee, Tyrel M. McQueen, and Daniel G. Nocera. Site Specific X-ray Anomalous Dispersion of the Geometrically Frustrated Kagomé Magnet, Herbertsmithite, $ZnCu_3(OH)_6Cl_2$. *Journal of the American Chemical Society*, 132(45):16185–16190, November 2010.

[186] T. Imai, M. Fu, T. H. Han, and Y. S. Lee. Local spin susceptibility of the S=1/2 kagome lattice in $ZnCu_3(OD)_6Cl_2$. *Physical Review B*, 84(2):020411, July 2011.

[187] M. A. de Vries, D. Wulferding, P. Lemmens, J. S. Lord, A. Harrison, P. Bonville, F. Bert, and P. Mendels. Extension of the zinc paratacamite phase diagram: Probing the effect of spin vacancies in an S = 1/2 kagome antiferromagnet. *Physical Review B*, 85(1):014422, January 2012.

[188] Zili Feng, Zheng Li, Xin Meng, Wei Yi, Yuan Wei, Jun Zhang, Yan-Cheng Wang, Wei Jiang, Zheng Liu, Shiyan Li, Feng Liu, Jianlin Luo, Shiliang Li, Guo-qing Zheng, Zi Yang Meng, Jia-Wei Mei, and Youguo Shi. Gapped Spin-1/2 Spinon Excitations in a New Kagome Quantum Spin Liquid Compound $Cu_3Zn(OH)_6FBr$. *Chinese Physics Letters*, 34(7):077502, June 2017.

[189] Katherine Tustain, Brendan Ward-O'Brien, Fabrice Bert, Tianheng Han, Hubertus Luetkens, Tom Lancaster, Benjamin M. Huddart, Peter J. Baker, and Lucy Clark. From magnetic order to quantum disorder in the Zn-barlowite series of S = 1/2 kagomé antiferromagnets. *npj Quantum Materials*, 5(1):1–9, October 2020.

[190] Zheng Liu, Xiaolong Zou, Jia-Wei Mei, and Feng Liu. Selectively doping barlowite for quantum spin liquid: A first-principles study. *Physical Review B*, 92(22):220102, December 2015.

[191] Daniel Guterding, Roser Valentí, and Harald O. Jeschke. Reduction of magnetic interlayer coupling in barlowite through isoelectronic substitution. *Physical Review B*, 94(12):125136, September 2016.

[192] Rebecca W. Smaha, Idris Boukahil, Charles J. Titus, Jack Mingde Jiang, John P. Sheckelton, Wei He, Jiajia Wen, John Vinson, Suyin Grass Wang, Yu-Sheng Chen, Simon J. Teat, Thomas P. Devereaux, C. Das Pemmaraju, and Young S. Lee. Site-specific structure at multiple length scales in kagome quantum spin liquid candidates. *Physical Review Materials*, 4(12):124406, December 2020.

[193] Rebecca W. Smaha, Wei He, Jack Mingde Jiang, Jiajia Wen, Yi-Fan Jiang, John P. Sheckelton, Charles J. Titus, Suyin Grass Wang, Yu-Sheng Chen, Simon J. Teat, Adam A. Aczel, Yang Zhao, Guangyong Xu, Jeffrey W. Lynn, Hong-Chen Jiang, and Young S. Lee. Materializing rival ground states in the barlowite family of kagome magnets: quantum spin liquid, spin ordered, and valence bond crystal states. *npj Quantum Materials*, 5(1):1–11, April 2020.

[194] Shaoyan Chu, Tyrel M. McQueen, Robin Chisnell, Danna E. Freedman, Peter Müller, Young S. Lee, and Daniel G. Nocera. A Cu^{2+}(S = 1/2) Kagomé Antiferromagnet: $Mg_xCu_{4-x}(OH)_6Cl_2$. *Journal of the American Chemical Society*, 132(16):5570–5571, April 2010.

[195] R.H. Colman, A. Sinclair, and A.S. Wills. Comparisons between Haydeeite, α-$Cu_3Mg(OD)_6Cl_2$, and Kapellasite, α-$Cu_3Zn(OD)_6Cl_2$, Isostructural S=1/2 Kagome Magnets. *Chemistry of Materials*, 22(20):5774–5779, October 2010.

[196] T. Malcherek, L. Bindi, M. Dini, M. R. Ghiara, A. Molina Donoso, F. Nestola, M. Rossi, and J. Schlüter. Tondiite, $Cu_3Mg(OH)_6Cl_2$, the Mg-analogue of herbertsmithite. *Mineralogical Magazine*, 78(3):583–590, June 2014.

[197] T. M. McQueen, T. H. Han, D. E. Freedman, P. W. Stephens, Y. S. Lee, and D. G. Nocera. $CdCu_3(OH)_6Cl_2$: A new layered hydroxide chloride. *Journal of Solid State Chemistry*, 184(12):3319–3323, December 2011.

[198] R. S. W. Braithwaite, K. Mereiter, W. H. Paar, and A. M. Clark. Herbertsmithite, $Cu_3Zn(OH)_6Cl_2$, a new species, and the definition of paratacamite. *Mineralogical Magazine*, 68(3):527–539, June 2004.

[199] Zili Feng, Wei Yi, Kejia Zhu, Yuan Wei, Shanshan Miao, Jie Ma, Jianlin Luo, Shiliang Li, Zi Yang Meng, and Youguo Shi. From Claringbullite to a New Spin Liquid Candidate $Cu_3Zn(OH)_6FCl$. *Chinese Physics Letters*, 36(1):017502, December 2018.

[200] Yuan Wei, Zili Feng, Clarina dela Cruz, Wei Yi, Zi Yang Meng, Jia-Wei Mei, Youguo Shi, and Shiliang Li. Antiferromagnetism in the kagome-lattice compound $Cu_3MgOH_6Br_2$. *Physical Review B*, 100(15):155129, October 2019.

[201] Anubhav Jain, Shyue Ping Ong, Geoffroy Hautier, Wei Chen, William Davidson Richards, Stephen Dacek, Shreyas Cholia, Dan Gunter, David Skinner, Gerbrand Ceder, and Kristin A. Persson. Commentary: The Materials Project: A materials genome approach to accelerating materials innovation. *APL Materials*, 1(1):011002, July 2013.

[202] Yutao Jiang, Ze Yu, Yuxin Wang, Tenglong Lu, Sheng Meng, Kun Jiang, and Miao Liu. Screening Promising CsV_3Sb_5-Like Kagome Materials from Systematic First-Principles Evaluation. *Chinese Physics Letters*, 39(4):047402, April 2022.

[203] Rebecca W. Smaha, Wei He, John P. Sheckelton, Jiajia Wen, and Young S. Lee. Synthesis-dependent properties of barlowite and Zn-substituted barlowite. *Journal of Solid State Chemistry*, 268:123–129, December 2018.

[204] Noah Ratcliff, Lily Hallett, Brenden R. Ortiz, Stephen D. Wilson, and John W. Harter. Coherent phonon spectroscopy and interlayer modulation of charge density wave order in the kagome metal CsV_3Sb_5. *Physical Review Materials*, 5(11):L111801, November 2021.

[205] Wing-Ho Ko, Patrick A. Lee, and Xiao-Gang Wen. Doped kagome system as exotic superconductor. *Physical Review B*, 79(21):214502, June 2009.

[206] H.-M. Guo and M. Franz. Topological insulator on the kagome lattice. *Physical Review B*, 80(11):113102, September 2009.

[207] Jun Wen, Andreas Rüegg, C.-C. Joseph Wang, and Gregory A. Fiete. Interaction-driven topological insulators on the kagome and the decorated honeycomb lattices. *Phys. Rev. B*, 82:075125, Aug 2010.

[208] Wan-Sheng Wang, Zheng-Zhao Li, Yuan-Yuan Xiang, and Qiang-Hua Wang. Competing electronic orders on kagome lattices at van Hove filling. *Physical Review B*, 87(11):115135, March 2013.

[209] Maximilian L. Kiesel, Christian Platt, and Ronny Thomale. Unconventional Fermi Surface Instabilities in the Kagome Hubbard Model. *Physical Review Letters*, 110(12):126405, March 2013.

[210] I. I. Mazin, Harald O. Jeschke, Frank Lechermann, Hunpyo Lee, Mario Fink, Ronny Thomale, and Roser Valentí. Theoretical prediction of a strongly correlated Dirac metal. *Nature Communications*, 5(1):4261, July 2014.

[211] Linda Ye, Mingu Kang, Junwei Liu, Felix Von Cube, Christina R. Wicker, Takehito Suzuki, Chris Jozwiak, Aaron Bostwick, Eli Rotenberg, David C. Bell, Liang Fu, Riccardo Comin, and Joseph G. Checkelsky. Massive Dirac fermions in a ferromagnetic kagome metal. *Nature*, 555(7698):638–642, March 2018.

[212] Mingu Kang, Linda Ye, Shiang Fang, Jhih-Shih You, Abe Levitan, Minyong Han, Jorge I. Facio, Chris Jozwiak, Aaron Bostwick, Eli Rotenberg, Mun K. Chan, Ross D. McDonald, David Graf, Konstantine Kaznatcheev, Elio Vescovo, David C. Bell, Efthimios Kaxiras, Jeroen Van Den Brink, Manuel Richter, Madhav Prasad Ghimire, Joseph G. Checkelsky, and Riccardo Comin. Dirac fermions and flat bands in the ideal kagome metal FeSn. *Nature Materials*, 19(2):163–169, February 2020.

[213] Brenden R. Ortiz, Samuel M. L. Teicher, Yong Hu, Julia L. Zuo, Paul M. Sarte, Emily C. Schueller, A. M. Milinda Abeykoon, Matthew J. Krogstad, Stephan Rosenkranz, Raymond Osborn, Ram Seshadri, Leon Balents, Junfeng He, and Stephen D. Wilson. CsV_3Sb_5: A Z_2 Topological Kagome Metal with a Superconducting Ground State. *Physical Review Letters*, 125(24):247002, December 2020.

[214] Brenden R. Ortiz, Samuel M. L. Teicher, Linus Kautzsch, Paul M. Sarte, Noah Ratcliff, John Harter, Jacob P. C. Ruff, Ram Seshadri, and Stephen D. Wilson. Fermi Surface Mapping and the Nature of Charge-Density-Wave Order in the Kagome Superconductor CsV_3Sb_5. *Physical Review X*, 11(4):041030, November 2021.

[215] Qiangwei Yin, Zhijun Tu, Chunsheng Gong, Yang Fu, Shaohua Yan, and Hechang Lei. Superconductivity and normal-state properties of kagome metal RbV_3Sb_5 single crystals. *Chinese Physics Letters*, 38(3):037403, Mar 2021.

[216] Hengxin Tan, Yizhou Liu, Ziqiang Wang, and Binghai Yan. Charge Density Waves and Electronic Properties of Superconducting Kagome Metals. *Physical Review Letters*, 127(4):046401, July 2021.

[217] Shuo-Ying Yang, Yaojia Wang, Brenden R. Ortiz, Defa Liu, Jacob Gayles, Elena Derunova, Rafael Gonzalez-Hernandez, Libor Šmejkal, Yulin Chen, Stuart S. P. Parkin, Stephen D. Wilson, Eric S. Toberer, Tyrel McQueen, and Mazhar N. Ali. Giant, unconventional anomalous Hall effect in the metallic frustrated magnet candidate, KV_3Sb_5. *Science Advances*, 6(31):eabb6003, July 2020.

[218] F. H. Yu, T. Wu, Z. Y. Wang, B. Lei, W. Z. Zhuo, J. J. Ying, and X. H. Chen. Concurrence of anomalous Hall effect and charge density wave in a superconducting topological kagome metal. *Physical Review B*, 104(4):L041103, July 2021.

[219] Yu-Xiao Jiang, Jia-Xin Yin, M. Michael Denner, Nana Shumiya, Brenden R. Ortiz, Gang Xu, Zurab Guguchia, Junyi He, Md Shafayat Hossain, Xiaoxiong Liu, Jacob Ruff, Linus Kautzsch, Songtian S. Zhang, Guoqing Chang, Ilya Belopolski, Qi Zhang, Tyler A. Cochran, Daniel Multer, Maksim Litskevich, Zi-Jia Cheng, Xian P. Yang, Ziqiang Wang, Ronny Thomale, Titus Neupert, Stephen D. Wilson, and M. Zahid Hasan. Unconventional chiral charge order in kagome superconductor KV_3Sb_5. *Nature Materials*, 20(10):1353–1357, October 2021.

[220] Eric M Kenney, Brenden R Ortiz, Chennan Wang, Stephen D Wilson, and Michael J Graf. Absence of local moments in the kagome metal KV_3Sb_5 as determined by muon spin spectroscopy. *Journal of Physics: Condensed Matter*, 33(23):235801, June 2021.

[221] C C Zhao, L S Wang, W Xia, Q W Yin, J M Ni, Y Y Huang, C P Tu, Z C Tao, Z J Tu, C S Gong, H C Lei, Y F Guo, X F Yang, and S Y Li. Nodal superconductivity and superconducting domes in the topological Kagome metal CsV_3Sb_5.

[222] K. Y. Chen, N. N. Wang, Q. W. Yin, Y. H. Gu, K. Jiang, Z. J. Tu, C. S. Gong, Y. Uwatoko, J. P. Sun, H. C. Lei, J. P. Hu, and J.-G. Cheng. Double Superconducting Dome and Triple Enhancement of T_c in the Kagome Superconductor CsV_3Sb_5 under High Pressure. *Physical Review Letters*, 126(24):247001, June 2021.

[223] Jian-Feng Zhang, Kai Liu, and Zhong-Yi Lu. First-principles study of the double-dome superconductivity in the kagome material CsV_3Sb_5 under pressure. *Physical Review B*, 104(19):195130, November 2021.

[224] Xu Chen, Xinhui Zhan, Xiaojun Wang, Jun Deng, Xiao-Bing Liu, Xin Chen, Jian-Gang Guo, and Xiaolong Chen. Highly Robust Reentrant Superconductivity in CsV_3Sb_5 under Pressure. *Chinese Physics Letters*, 38(5):057402, June 2021.

[225] Zuowei Liang, Xingyuan Hou, Fan Zhang, Wanru Ma, Ping Wu, Zongyuan Zhang, Fanghang Yu, J.-J. Ying, Kun Jiang, Lei Shan, Zhenyu Wang, and X.-H. Chen. Three-Dimensional Charge Density Wave and Surface-Dependent Vortex-Core States in a Kagome Superconductor CsV_3Sb_5. *Physical Review X*, 11(3):031026, August 2021.

[226] Haoxiang Li, T. T. Zhang, T. Yilmaz, Y. Y. Pai, C. E. Marvinney, A. Said, Q. W. Yin, C. S. Gong, Z. J. Tu, E. Vescovo, C. S. Nelson, R. G. Moore, S. Murakami, H. C. Lei, H. N. Lee, B. J. Lawrie, and H. Miao. Observation of unconventional charge density wave without acoustic phonon anomaly in kagome superconductors AV_3Sb_5 (A = Rb, Cs). *Physical Review X*, 11(3):031050, September 2021.

[227] He Zhao, Hong Li, Brenden R. Ortiz, Samuel M. L. Teicher, Takamori Park, Mengxing Ye, Ziqiang Wang, Leon Balents, Stephen D. Wilson, and Ilija Zeljkovic. Cascade of correlated electron states in a kagome superconductor CsV_3Sb_5. *Nature*, 599(7884):216–221, November 2021.

[228] Shunli Ni, Sheng Ma, Yuhang Zhang, Jie Yuan, Haitao Yang, Zouyouwei Lu, Ningning Wang, Jianping Sun, Zhen Zhao, Dong Li, Shaobo Liu, Hua Zhang, Hui Chen, Kui Jin, Jinguang Cheng, Li Yu, Fang Zhou, Xiaoli Dong, Jiangping Hu, Hong-Jun Gao, and Zhongxian Zhao. Anisotropic superconducting properties of kagome metal CsV_3Sb_5. *Chinese Physics Letters*, 38(5):057403, jun 2021.

[229] E. Uykur, B. R. Ortiz, S. D. Wilson, M. Dressel, and A. A. Tsirlin. Optical detection of charge-density-wave instability in the non-magnetic kagome metal KV_3Sb_5. *npj Quantum Materials*, 7(1):16, January 2022.

[230] Nathan P. Wells, Paul M. Belden, Joseph R. Demers, and William T. Lotshaw. Transient reflectivity as a probe of ultrafast carrier dynamics in semiconductors: A revised model for low-temperature grown GaAs. *Journal of Applied Physics*, 116(7):073506, August 2014.

[231] Hui Chen, Haitao Yang, Bin Hu, Zhen Zhao, Jie Yuan, Yuqing Xing, Guojian Qian, Zihao Huang, Geng Li, Yuhan Ye, Sheng Ma, Shunli Ni, Hua Zhang, Qiangwei Yin, Chunsheng Gong, Zhijun Tu, Hechang Lei, Hengxin Tan, Sen Zhou, Chengmin Shen, Xiaoli Dong, Binghai Yan, Ziqiang Wang, and Hong-Jun Gao. Roton pair density wave in a strong-coupling kagome superconductor. *Nature*, 599(7884):222–228, November 2021.